Electronic Structure & Electrical properties of Ultra-Nanocrystalline Diamond (UNCD) for Multifunctional Devices.

by

Ramakgahlela Wendy Thoka

A dissertation submitted in accordance with the requirements of the degree of Master of Science in Physics at the University of South Africa.

Supervisor   : Prof. S. C. Ray (University of South Africa)

Co-supervisor   : Prof. S. J. Moloi (University of South Africa)

November 2020

i

Declaration

I,

Name: Ramakgahlela Wendy Thoka
Student number: 43123732

 declare that "**Electronic Structure & Electrical Properties of Ultra-Nanocrystalline Diamond (UNCD) for Multifunctional Devices** " is my own work and that all sources that I have used or quoted have been indicated and acknowledged by means of references.

I further declare that none of this material has been submitted for any other degree at University of South Africa (Unisa) for another qualification or at any other higher education institution.

....

Ramakgahlela Wendy Thoka   Date

Publication and Presentation

Peer-Reviewed publication

1. R**.W. Thoka**, S. J. Moloi, Sekhar C. Ray, W.F. Pong, I.-N. Lin, *Microstructure and electronic properties of ultra-nano-crystalline-diamond thin films,* Journal of Electron Spectroscopy and Related Phenomena **242**; 146968, (2020)

Poster Presentation

1. C-P-491: R.W. Thoka, S.J. Moloi, Sekhar C. Ray, W.F. Pong, I.-N. Lin, Microstructure and electronic properties of ultra-nano-crystalline-diamond thin films.

   -- Presented by Sekhar Chandra Ray in TACT 2019 International Thin Films conference, Nov 17-20, 2019. GIS NTUT Convention Center, National Taipei University of Technology, Taipei, Taiwan.

Acknowledgements

Abstract

In this work, we have synthesized ultra-nano-crystalline diamond (UNCD) thin films with average thickness ∼200 nm on n-type mirror polished silicon (100) substrates using microwave plasma enhanced chemical vapour deposition (MW-PECVD) system. The synthesis was carried out in different gas (H_2 - N_2 - Ar - CH_4) composition plasma atmospheres at 1200 W (2.45 GHz) and in the pressure of 120 Torr with plasma-temperature ∼475 °C. Surface morphology of all thin films were studied using high resolution scanning electron microscopy (HR -SEM) images. Raman spectroscopy was used for microstructural study and nanoindentation technique was used for the Hardness/Young's modulus study; whereas X-ray absorption near edge structure (XANES), X-ray photoelectron (XPS) and ultraviolet photoemission spectroscopies (UV-PES) techniques were used to study electronic structure of UNCD thin films. Electrical measurements, current -voltage (I-V), were used to study the conductivity of the films. The hardness of the films is found to be ∼30 GPa, Young's modulus to be ∼300 GPa and induced electron field emission, the turn on electric field, E_{TOE} = 11 V/µm. The results, in general, show that the UNCD could be useful for different industrial semiconductor/optoelectronic devices and as flexible materials for thin film coating technology.

Dedication

This work is dedicated to my late son Ntsako (Buti Nono). May your precious soul continue to rest in peace my darling boy. You are dearly missed.

&

His little brother Ofentse & little sister Vutivi.

Table of content

Chapter 1

Introduction

1.1 Background

Ultra-nanocrystalline diamond (UNCD) is one of the important triads of nanostructured carbons that compose of 3-5 nm crystallites. It is an exemplar par excellence of the profound changes in properties that can accompany the reduction in the size of material to low single digit nanometer dimensions. UNCD exhibits extreme hardness (97 GPa), low friction (0.1 in air) and outstanding chemical resistance. Consequently, the application of UNCD coatings to multipurpose mechanical pump seals can reduce frictional energy losses and eliminate downtime and hazardous emissions from seal failure and leakage. Researchers report that with specific pore size and ease of fabrication, diamond nano-feathers could be a great material of choice for supercapacitors, batteries, sensors, and solar cells to mention the few [1].

1.2 Problem statement and research motivation

Among many types of hard physical- and chemical-vapor deposition (PVD and CVD) coatings, diamond and diamond-like carbon coatings have attracted the most attention for sliding or rotating tribological surfaces, especially in micro-electro-mechanical systems (MEMS), biomedical and nano-scale applications [2–6].

In this study, UNCD films were prepared by microwave plasma chemical vapor deposition utilizing an argon/methane/nitrogen/hydrogen gas mixture. The films were examined using x-ray diffraction, Raman microanalysis, scanning electron microscopy, x-ray photoelectron spectroscopy, electrical and Young's modulus / hardness measurement techniques. The results, in general, indicate the feasibility of using UNCD in electronic devices and coating technology device applications.

1.3 Justification

The aim of the present research is to synthesize UNCD films and characterize the films using different characterization techniques to study their microstructure, electronic, electrical, and mechanical properties. The acquired data are then analyzed to provide the information regarding different applications in our daily life.

1.4 Aim and objectives

The objectives of this project are to investigate microstructure-mechanical-electronic transport property relationships of a new multifunctional material designated as ultra-nanocrystalline diamond (UNCD) for utilizing this material in novel microelectromechanical systems (MEMS) and nanoelectromechanical systems (NEMS).

1.5 Dissertation statement

In this work UNCD thin films will be synthesized on silicon substrate using microwave plasma enhanced chemical vapor deposition (MPCVD) technique and to study their practical applications. Large and clean UNCD films can be produced at very high growth rates, and their properties; mechanical, chemical, optical, electronic, and mechanical, can be tuned over a wide range. The goal is to produce large UNCD crystals in a thin film form that could be useful for practical application in our day-to-day life.

1.6 Dissertation outline

The dissertation is divided into five chapters, which entail

● **Chapter 1**: a brief background, the problem statement and research motivation,

● **Chapter 2:** a brief literature review of UNCD thin films,

● **Chapter 3:** experimental methodology,

● **Chapter 4:** preparation, characterization, results, discussion, conclusion, and prediction for future applications.

● **Chapter 5:** conclusion and recommendation for future work.

References

[1] Zeng, H., Moldovan, N., Catausan, G., 2019. *Diamond nanofeathers.* Diam. Relat. Mater., 91, pp. 165-172.

[2] Auciello, O., Krauss, A.R., Gruen, D.M., Ersoy, D., Tucek, J., Jayatissa, 2001. *Ultra-nanocrystalline diamond thin films for MEMS and moving mechanical assembly devices.* Diam. Relat. Mater., 10(11), pp.1952–1961.

[3] Sumant, A.V., Grierson, D.S., Gerbi, J.E., Carlisle, J.A., Auciello, O. and Carpick. R.W., 2007. *Surface chemistry and bonding configuration of ultra-nanocrystalline diamond surfaces and their effects on nanotribological properties.* Phys. Rev. B, 76 (23), p.235429.

[4] Bajaj, P., Akin, D., A. Gupta, A., Sherman, D., Shi, B., Auciello, O., Rashid, R., 2007. *Ultra-nanocrystalline diamond film as an optimal cell interface for biomedical applications.* Biomed. Microdevices, 9(6), pp.787–794.

[5] Grierson, D.S., Sumant A.V., Konicek, A.R., Abrecht, A., Birrell, J., Auciello, O., Carlisle, J.A., Scharf, T.W., Dugger, M.T., Gilbert, P.U.P.A., Carpick, R.W., 2007. *Tribochemistry and material transfer for the ultra-nanocrystalline diamond-silicon nitride interface revealed by X-ray photoelectron emission Spectro-microscopy.* J. Vac. Sci. Technol. B ,25(5), pp.1700–1705.

[6] Sumant, V., Grierson, D.S., Gerbi, J.E., Birrell, J., Lanke, U.D., Auciello, O., Carlisle, J.A., Carpick, R.W., 2005. *Toward the ultimate tribological interface: surface chemistry and nanotribology of ultra-nanocrystalline diamond.* Adv. Mater. ,17(8), pp.1039–1045.

Chapter 2

Literature review

Diamond is one of the most unique materials with excellent physical and chemical properties have ever been discovered. Whether it comes from nature or it is man-made, diamond has advantages over other materials due to these properties. The synthetic diamond materials usually suppress the defects that are commonly observed in the natural diamonds. Among the diamond synthesis methods, chemical vapor deposition method has received a great deal of attention in the material sciences since many new applications of the material are discovered using the method. These applications could not be discovered since other methods were relatively expensive with difficult procedure to follow, hence impossible to reproduce the material.

The manufacturing of UNCD films to exhibit unique and outstanding properties for various applications is possible with chemical vapor deposition method. These properties, among others, include high hardness, fracture strength, Young's modulus and wear resistance. The outstanding properties also involve extremely low friction coefficient, negligible stiction, low residual stress in as-deposited thin films, unique field electron-emission properties, a wide range of conductivity controlled by microstructure and doping, and highly conformal films. These properties are crucial for the development of novel MEMS/NEMS applications.

2.1 Ultra-nanocrystalline diamond (UNCD)

2.1.1 Structures

Ultra-nanocrystalline diamond (UNCD) film is a unique form of carbon, in which diamond grains of 3–5 nm sizes are surrounded by an amorphous carbon matrix. The film has applications where high conductivity is required, including electrochemical electrodes [1–3],

field emission [4] and heterostructures [5,6]. It has been reported that a nitrogen-doped UNCD film exhibits n-type conduction with an enhanced electrical conductivity attributed to the increased number of sp^2 bonds at grain boundaries (GBs) [7,8]. Amorphous carbon in GBs is a common component in UNCD films, whose electrical conductivities were reported to be not sufficiently high, thus limiting the applications of UNCD films [9]. It is believed that the conversion of amorphous carbon to a conducting graphitic phase along GBs enhances the efficiency for electron transport on the surface, thus improving the conductivity of the UNCD film [10,11]. Thus, the electrical properties can be effectively improved by modifying the structure and component of amorphous-carbon GBs. Carbon ions are not dopants for diamond grains, but they lead to more ordered amorphous-carbon GBs to enhance charge mobility. A high-dose C+-ion implantation (10^{15} cm^{-2}) and annealing lead to the crystallization of graphite phase not transformed from amorphous carbon in the UNCD film and degradation of the field-emission properties [12].

2.1.2 Properties

UNCD, a form of nanocrystalline diamond, captures many of the best properties of natural diamond in a scalable thin film technology. These properties enable diamond to be integrated into a wide range of products. UNCD is the term that encompasses a proprietary family of materials that are manufactured using patented chemical vapor deposition processes. UNCD can also have other unique properties adjustable and optimized for specific application. These properties are as follows:

Mechanical and Tribological properties [13-15]

- **Extreme hardness.**
- **Extremely wear resistant.**
- **Extremely strong.** Just as strong as single-crystal diamond.

6

- **Smooth.** Very low surface roughness.

- **Thin.** Ultrathin pinhole-free films can be produced.

- **Excellent adhesion.** UNCD is routinely deposited on silicon, SiO_2, W, Mo, TiAl4V6, and alpha "self-sintered" (binderless) SiC as well as Ta and Si3N4. Materials that readily form carbides tend to make the best substrates. Please contact us to inquire about additional materials.

- **Very low friction.** Coefficients of friction as low as 0.03 in air.

- **No stiction.** Hydrophobicity eliminates stiction in MEMS components, reducing manufacturing and packaging costs, while enhancing reliability.

- **Low film stress.** Critically important for materials integration in MEMS and other thin film applications.

Chemical properties [16]

- **Chemically stable and inert.** Same surface chemistry as natural diamond.

- **Hydrophobicity.** Can be rendered either hydrophobic or hydrophilic by adjusting surface chemistry.

- **Electrochemistry.** Very wide working potential window, low background currents.

- **Corrosion protection.** Diamond surface chemistry and ultrathin continuous films provide protective coatings.

Electrical properties [17-19]

- **Electrically conductive or insulating.** High room temperature N-type and P-type conductivities have been demonstrated.

- **Electron emitters.** Low threshold, stable field electron emission has been demonstrated.

- **Surface functionalization.** Probe molecules can be covalently attached with high stability for biosensors.

- **Bio-inert.** Can be used in biomedical applications such as bio-MEMS sensors and implants.

Microfabrication of Ultra-nanocrystalline diamond (UNCD) [20]

- **Low deposition temperatures.** Compatible with fragile electronics and low-melting point metals such as aluminium.

- **Conformal coatings.** Capable of coating high-aspect-ratio structures with conformal, smooth layers.

- **Etching.** UNCD can be etched using reactive ion etching.

UNCD enables devices to be fabricated that are:

- **Faster.** High acoustic velocity permits faster high frequency electronic filters andtime references (MHz-GHz).

- **More reliable.** Low stiction, friction, thermal stability and superior wear resistance.

- **Versatile.** Can be deposited on a range of substrates and integrated into complex thin film hetero structures that can be used in harsh environments.

2.1.3 Synthesis methods

Ultra-nanocrystalline diamond (UNCD) has been synthesized by means of hot filament CVD (HF-CVD), catalytic CVD, radio frequency (RF), direct-current (DC) and microwave plasma enhanced CVD (MPECVD) in hydrocarbon gas mixtures such as CH_4 or C_2H_6 diluted by H_2 [21-26].

2.1.4 Growth mechanism

The C_2 radical played an important role in the growth mechanism for UNCD [27]. However, some of the researchers [28-30] have shown that C_2 is only a minority species close to the substrate surface and plays no significant role in growth. May *et al.* [29] used a 2-dimensional model of the gas chemistry, including heat and mass transfer in HF reactors to understand the experimental observations. The conclusions led to a generalized mechanism [29] for the growth of diamond by CVD, which was consistent with all experimental observations, both from their group [29] and from others in the literature [28, 30]. The proposed mechanism involves competitive growth by all the C_1 radical species that are present in the gas mixture close to the growing diamond surface. Previous models only considered CH_3 since this is the dominant reactive hydrocarbon radical in standard H_2-rich CVD gas mixtures. However, May et al. [29] found that in HFCVD reactors at high filament temperatures (e.g. $T_{Filament}$ ~2700 K), the concentration of the other C_1 radical species, in particular C atoms, near the growing diamond surface can become a significant fraction (~5%) of that of CH_3, and so may contribute to the growth process.

In the model, abstraction of surface H atoms by gas phase atomic H are the reactions which drive the chemistry of growth. The various types of surface radical that result from abstraction are shown in Fig. 2.1. May et al. [29] proposed that CH_3 remains the major growth species, and if this adds to a surface bi-radical site, $C_d^* - C_d^*$, (defined as two surface radical sites adjacent to one another, see Fig. 2.1(d), the 'dangling bonds' on the surface are terminated and stabilized [32]. For typical diamond CVD conditions, the fraction of available biradical sites is ~10 times lower than that of radical sites (Fig.1(b)), but CH_3 cannot add to more abundant radical sites due to steric hindrance [31]. Further hydrogen abstraction converts the surface CH_3 groups into bridging CH_2 groups, and repetition of this process allows the CH_2 groups to migrate across the surface until they meet a step-edge, at which point they will extend the diamond lattice

leading to large regular crystals, and a microcrystalline diamond (MCD) film [29]. Thus, the prerequisites for MCD film formation are high H concentration (to generate enough surface biradical sites), high CH_3 concentration, and the rapid migration across the surface of CH_2 groups (catalyzed by H atom abstractions).
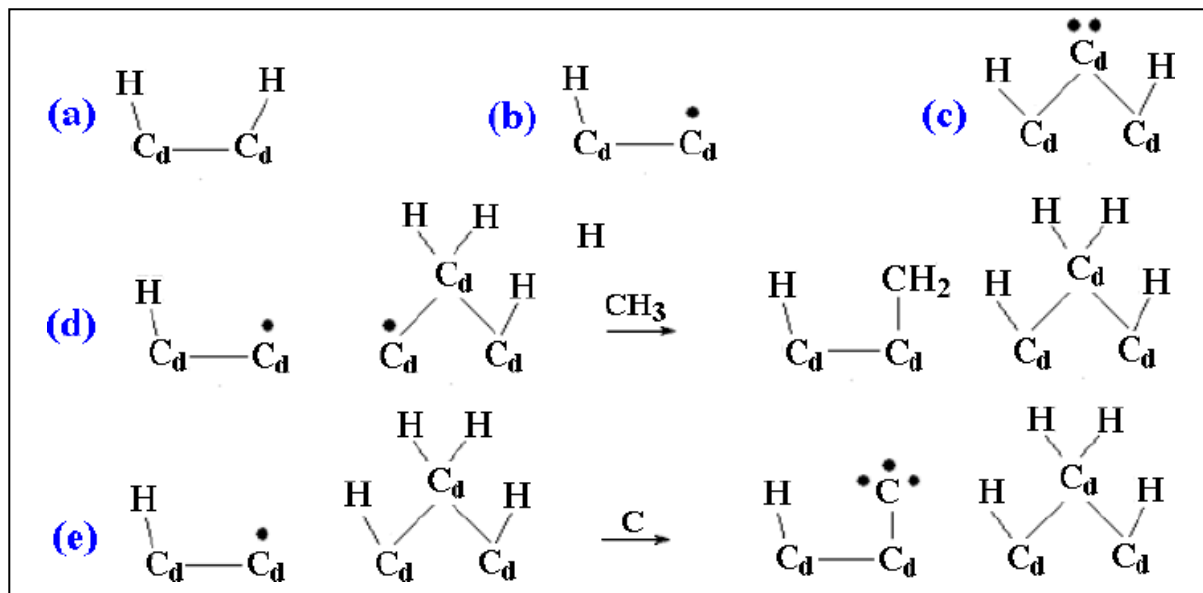
Figure 2.1. *Schematic diagram of the various (100) - (2×1) dimer surface and bridge sites important for diamond growth and re-nucleation. (a) A hydrogen terminated diamond surface. (b) A surface radical site C_d*. (c) A surface biradical site C_d**. (d) A different type of surface biradical site, C_d* - C_d*, followed by its reaction with methyl to give a CH_2 surface group [31]. (e) The radical site also reacts with a C atom (or CH radical, not shown) to give a reactive surface adduct C_d**.*

In CH_3 addition, however, May et al. [29] assumed that C atoms or CH radicals (also CH_2 but these have been neglected since their density close to the substrate surface is much lower) could also be adsorbed on the surface. Due to their smaller size, atomic C and CH have less steric hindrance and can add to both surface biradical sites and radical sites (see Fig. 2.1). Thus, even for low C atom concentrations, [C]/[CH_3] ~ 0.1, their contribution to the growth rate can be important since they can add to the more abundant radical sites. The resulting adducts structure C_d** (see Fig.1(e)) would remain reactive since it would still contain dangling bonds, making this a very high energy site. The most likely fate for such reactive surface sites, considering

that they are surrounded by a gas mixture containing a high concentration of H atoms and H_2 molecules, is that they are rapidly hydrogenated to CH_2. If so, the subsequent reactions will be indistinguishable from attachment and growth by methyl. However, other possible fates for the reactive surface adducts are reaction with other gas-phase hydrocarbon radicals CHx or restructuring of the surface. The role of such adducts as an initiator of re-nucleation processes requires additional theoretical study. For the typical conditions used to deposit MCD/NCD and UNCD in a variety of different diamond CVD reactors (including MW and HF CVD reactors), the reactions of the surface adducts with atomic hydrogen which lead to continuous normal diamond growth are much more frequent events than the reactions with CHx which ultimately could lead to re-nucleation. As long as the surface migration of CH_2 (induced by H abstractions) is much faster than adsorption of CH_3, the aggregation of CH_2 bridge sites into continuous chains (void filling) will provide normal layer-by-layer <100> diamond growth [31]. As the ratio of gaseous CHx/H increases, however, the initiation of next layer growth could proceed before all the voids in the current layer are filled. Thus, depending upon the gas mixture and reaction conditions used, the relative concentrations of each of these species close to the growing diamond surface (e.g. [H]/[CH_3], ([C]+[CH])/[CH_3]) determine the probability of a re-nucleation event occurring and average crystal sizes, <d>, and hence the morphology of the subsequent film, be it MCD, NCD or UNCD.

2.1.5 Applications

Ultra-nanocrystalline diamond (UNCD) films [33-35] with grains of 2–5 nm and a smooth surface of 10–20 nm root-mean-square (RMS) are candidates for fabrication of multifunctional devices, such as for microelectromechanical systems (MEMS) that require a high Young's modulus, low friction coefficient and high resistance to wear [36,37]. UNCD films are also used in biomedical devices requiring bio-inertness and non-cytotoxicity [38,39]. Combining these superior characteristics, UNCD is a potential material for use in biomedical devices such

as bio-MEMS. Diamond coatings have the chemical inertness and impermeability required to reduce the crevice corrosion that is commonly seen in conventional metallic implants. Recently, the suitability and non-cytotoxicity of ultra-nano-diamond films as a support surface for cell growth and proliferation has been proven [40-42]. Xiao et al. demonstrated the successful insertion of UNCD bioinert encapsulation coatings of silicon microchips into human eyes [43]. However, the responses of neural stem cells (NSCs) to the UNCD films through their nanoscale surface features and the different electron affinities that result from surface modification have not yet been studied. For the clinical applications it is require to precise the controlling of differentiation of NSCs *in vivo*, because most injuries to the central nervous system are caused by the loss or damage of a specific sub-population of the neural lineages [44,45]. Thus, focused on obtaining the N-doped UNCD films modified by hydrogen (H-) surface treatment. In this work, it is elucidated the nature of the top surfaces of modified UNCD films to H-terminated UNCD films. The results showed that H-terminated UNCD films support differentiation for various applications [44, 45].

References

[1]   Wang, J., Firestone, M.A., Auciello, O., Carlisle, J.A., 2004. *Surface functionalization of ultrananocrystalline diamond films by electrochemical reduction of Aryldiazonium salts.* Langmuir, 20(6), pp.11450-11456.

[2]   Garrett, D.J., Ganesan, K., Stacey, A., Fox, K., Meffin, H., Prawer, S. 2012. *Ultra-nanocrystalline diamond electrodes: optimization towards neural stimulation applications.* J. Neural. Eng., 91), p.016002.

[3]   Jiang, Y., Yu, H., Li, X., Lu, S.H., Hu, X.J., 2017. *Thermal oxidation induced high electrochemical activity of boron-doped nanocrystalline diamond electrodes.* Electrochim. Acta, 258, pp.61-70.

[4]   Sankaran, K., Srinivasu, K., Yeh, C., Thomas, J., Drijkoningen, S., Pobedinskas, P., Sundaravel, B., Leou, K. C., Leung, K.T., Van Bael, M.K., Schreck, M., Lin, I.N., Haenen, K.,2017. *Field electron emission enhancement in lithium implanted and annealed nitrogen-incorporated nanocrystalline diamond films.* Appl. Phys. Lett., 110(26), p.1602.

[5]   Zkria, A., Yoshitake, T., (2016). *Low-temperature carrier transport properties of n-type ultrananocrystalline diamond/p-type Si heterojunction diodes.* (2016) Compound Semiconductor Week (CSW), Includes 28th International Conference on Indium Phosphide & Related Materials (IPRM) & 43rd International Symposium on Compound Semiconductors (ISCS), pp. 1-2.

[6]   Zimmermann, T., Kubovic, M., Denisenko, A., Janischowsky, K., Williams, O.A., Gruen, D., Kohn, E., 2005. Ultra-nano-crystalline/single crystal diamond heterostructure diode. Diam. Relat. Mater., 14(4-7), pp.416-420.

[7]   Panda, K., Sundaravel, B., Panigrahi, B., Magudapathy, P., Nandagopala, K. D, Nair, K.,
        Chen, H. C., Lin, I. N., 2011. *Structural and electronic properties of nitrogen ion
        implanted ultrananocrystalline diamond surfaces.* J. Appl. Phys., 110(4), p.044304.

[8]   Zapol, P., Sternberg, M., Curtiss, L.A., Frauenheim, T. and Gruen, D. M., 2001. *Tight-
        binding molecular-dynamics simulation of impurities in ultrananocrystalline diamond
        grain boundaries.* Phys. Rev. B, 65(4), p. 045403.

[9]   Sankaran, K.J., Panda, K., Sundaravel, B., Chen, H. C., Lin, I.N., Lee, C.Y. Tai,
        N. H., 2012. *Engineering the Interface Characteristics of Ultrananocrystalline Diamond
        Films Grown on Au-Coated Si Substrates.* ACS Appl. Mater. Inter., 4(8), p.4169-4176.

[10]   Sankaran, K. J., Lin, Y. F., Jian, W. B., Chen, H. C., Panda, K., Sundaravel, B., Dong
        C.L., Tai, N. H., Lin, I. N., 2013. *Structural and electrical properties of conducting
        diamond nanowires.* ACS Appl. Mater. Inter., 5(4), pp.1294-1301.

[11]   Arenal, R., Bruno, P., Miller, D., Bleuel, M., Lal, J., Gruen, D., 2007. *Diamond nanowires
        and the insulator-metal transition in ultrananocrystalline diamond films.* Phys. Rev. B,
        75(19), p.195431.

[12]   Hu, X. J., Ye, J.S., Liu, H.J., Shen, Y.G., Chen, X. H., Hu, H., 2011. *n-type conductivity
        and phase transition in ultrananocrystalline diamond films by oxygen ion implantation
        and annealing.* J. Appl. Phys., 109(5), p.053524.

[13]   Rani, R., Panda, K., Kumar, N., Titovich, K.A., Kolesnikov, V.I, Vyacheslavovich,
        S.A., and Lin, I.N., 2018. *Tribological Properties of Ultra-nanocrystalline Diamond
        Films: Mechanochemical Transformation of Sliding Interfaces.* Sci. Reports.,
        8(1), pp.1-16.

[14]   Auciello, O., Sumant, A.V., 2018. *Status review of the science and technology of ultra-
        nanocrystalline diamond (UNCD) films and application to multifunctional devices.*
        Diam. Relat. Mater., 19(7-9), pp.699–718.

[15] Kumar, N., Sharma, N., Popov, C., Kulisch. W., Reithmaier, J.P, Favaro, G., A.K. Tyagi, A.K., Raj, B., 2011. *Tribological properties of ultrananocrystalline diamond films in various test atmosphere.* Tribology International, 44(12), pp.2042-2049.

[16] Palomino, J., Varshney, D., Resto, O., Weiner, B.R., Morell, G., 2014. *Ultra-nanocrystalline Diamond-Decorated Silicon Nanowire Field Emitters.* ACS Appl. Mater. Inter., 6(16), pp.13815−13822.

[17] Kulisch, W., Popov, C., Lefterova, E., Bliznakov, S., Reithmaier, J.P., Rossi, F., 2010. *Electrical properties of ultra-nanocrystalline diamond/amorphous carbon nanocomposite films.* Diam. Relat. Mater., 19 (5-6), pp.449–452

[18] Gan, L., Bolker, A., Saguy, C., Kalish, R., Tan, D.L., Tay, B.K., Gruen, D., Bruno, P., 2009. *The effect of grain boundaries and adsorbates on the electrical properties of hydrogenated ultra-nanocrystalline diamond.* Diam. Relat. Mater., 18(9), pp.1118–1122.

[19] Tzeng, Y., Yeh, S., Cheng, W., Fang, W. and Chu, Y., 2014. *Nitrogen-incorporated ultrananocrystalline diamond and multi-layer-graphene-like hybrid carbon films.* Sci Rep., 4, p. 4531.

[20] Williams, O.A., 2006. *Ultra-nanocrystalline diamond for electronic applications.* Semicond Sci Technol., 21(8), pp.49-56.

[21] Tzeng, Y., Chen, C.-L., Chen, Y.Y., Liu, C.Y., 2010. *Carbon nanowalls on graphite for cold cathode applications.* Diam. Relat. Mater., 19(2-3), pp.201–204.

[22] Dikonimos, T.H., 2007. *DC plasma enhanced growth of oriented carbon nanowall films by HFCVD.* Diam. Relat. Mater., 16 (4-7), pp.1240–1243.

[23] Itoh, T., Shimabukuro, S., Kawamura, S., Nonomura, S.,2006. *Preparation and electron field emission of carbon nanowall by Cat-CVD.* Thin Solid Films, 501(1-2), pp.314–317.

[24] Wu, Y., Qiao, P., Chong, T. & Shen, Z., 2002. *Carbon nanowalls grown by microwave plasma enhanced chemical vapor deposition.* Adv. Mater., 14(1), pp.64–67.

[25] Nishimura, K., Jiang, N., Hiraki, A., 2003. *Growth and characterization of carbon nanowalls.* IEICE Trans Electron E86–C, 5, pp.821–824.

[26] Tanaka, K., Yoshimura, M., Okamoto, A., Ueda, K., 2005. *Growth of carbon nanowalls on a SiO$_2$ substrate by microwave plasma enhanced chemical vapor deposition.* Jpn. J. Appl. Phys, 44(4R), pp.2074–2076.

[27]   Zhou, D., McCauley, T.G., Qin, L.C., Krauss, A.R. and Gruen, D.M., 1998. *Synthesis of nanocrystalline diamond thin films from an Ar–CH4 microwave plasma.* J. Appl. Phys., 83(1), pp.540-543.

[28]   May, P.W., Harvey, J.N., Smith, J.A., Mankelevich, Y.A., 2006. *Reevaluation of the mechanism for ultrananocrystalline diamond deposition from Ar/ CH 4/H2 gas mixtures.* J. Appl. Phys., 99(10), p.104907.

[29]   May, P.W., Mankelevich, Y.A., 2006. *Experiment and modeling of the deposition of ultrananocrystalline diamond films using hot filament chemical vapor deposition and Ar/ CH4/H2 gas mixtures: A generalized mechanism for ultrananocrystalline diamond growth.* J. Appl. Phys., 100(2), p.024301.

[30] Rabeau, J.R., John, P., Wilson, J.I.B., Fan, Y., 2004. *The role of C 2 in nanocrystalline diamond growth.* J. Appl. Phys., *96*(11), pp.6724-6732.

[31] Skokov, S., Weiner, B., Frenklach, M., 1994. *Elementary reaction mechanism for growth of diamond (100) surfaces from methyl radicals.* J. Phys. Chem., 98(28), pp.7073- 7082.

[32] Smith, J.A., Wills, J.B., Moores, H.S., Orr-Ewing, A.J., Ashfold, M.N., Mankelevich, Y.A., Suetin, N.V., 2002. *Effects of NH3 and N2 additions to hot filament activated CH4/H2 gas mixtures.* J. Appl. Phys., 92(2), pp.672-681.

[33] Gruen, D.M., 1999. *Nanocrystalline diamond films.* Annu. Rev. Mater. Sci, 29(1), pp.211-259.

[34] Chen, Y.C., Zhong, X.Y., Konicek, A.R., Grierson, D.S., Tai, N.H., Lin, I.N., Kabius, B., Hiller, J.M., Sumant, A.V., Carpick, R.W., Auciello, O., 2008. *Synthesis and characterization of smooth ultrananocrystalline diamond films via low pressure bias-enhanced nucleation and growth.* Appl. Phys. Lett., 92(13), p.133113.

[35] Lee, Y.C., Lin, S.J., Chia, C.T., Cheng, H.F., Lin, I.N., 2005. *Effect of processing parameters on the nucleation behavior of nano-crystalline diamond film*. Diam. Relat. Mater., 14(3-7), pp.296-301.

[36] Auciello, O., Birrell, J., Carlisle, J.A., Gerbi, J.E., Xiao, X., Peng, B., Espinosa, H.D., 2004. *Materials science and fabrication processes for a new MEMS technology based on ultrananocrystalline diamond thin films.* J. Phys: Condens. Mater., 16(16), p.R539.

[37] Lee, Y.C., Lin, S.J., Buck, V., Kunze, R., Schmidt, H., Lin, C.Y., Fang, W.L., Lin, I.N., 2008. *Surface acoustic wave properties of natural smooth ultra-nanocrystalline diamond characterized by laser-induced SAW pulse technique.* Diam. Relat. Mater., 17(4-5), pp.446-450.

[38] Yang, W., Auciello, O., Butler, J.E., Cai, W., Carlisle, J.A., Gerbi, J.E., Gruen, D.M., Knickerbocker, Lasseter T.L., Russell Jr, J.N., Smith, L.M., Hamers, R.J., 2002. *DNA-modified nanocrystalline diamond thin films as stable, biologically active substrates.* Nat. Mater., 1, pp.253-257

[39] Nebel, C.E., Rezek, B., Shin, D., Uetsuka, H., Yang, N., 2007. *Diamond for bio-sensor applications*. J. Phys D: Appl. Phys., 40(20), p.6443.

[40] Lechleitner, T., Klauser, F., Seppi, T., Lechner, J., Jennings, P., Perco, P., Mayer, B., Steinmuller-Nethl. D., Hermann, M., Bertel, E., Pfaller, K., Pfaller, W., 2008. *The*

surface properties of nanocrystalline diamond and nanoparticulate diamond powder and their suitability as cell growth support surfaces. Biomaterials, 29 (32), pp.4275-4284.

[41]   Amaral, M., Dias, A.G, Gomes, P.S., Lopes, M.A., Silva, R.F., Santos, J.D., Fernandes, M.H., 2008. *Nanocrystalline diamond: in vitro biocompatibility assessment by MG63 and human bone marrow cells cultures.* J. Biomed. Mater. Res A., 87(1), pp91-99.

[42]   Clem, W.C., Chowdhury, S., Weimer, J.J., Shaik, F.M., Hennessy, K.M., Konovalov, V.V., Waterfeld, A., Bellis, S., Vohra, Y.K., 2008. *Mesenchymal stem cell interaction with ultra-smooth nanostructured diamond for wear-resistant orthopaedic implants.* Biomaterials, 29(24-25), pp.3461-3468.

[43]   Xiao, X.C., Wang, J., Liu, C., Carlisle, J.A., Mech, B., Greenberg, R., Guven, D., Freada, R., Humayun, M.S., Wieland, J., Auciello, O., 2006. *In vitro and in vivo evaluation of ultrananocrystalline diamond for coating of implantable retinal microchips.* J. Biomed. Mater. Res B Appl. Biomater., 77(2), pp.273-281

[44]   Armstrong, R.J., Svendsen, C.N., 2000. *Neural stem cells: from cell biology to cell replacement.* Cell Transplant., 9(2), pp. 139-152

[45]   Bithell, A., Williams, B.P., 2005. *Neural stem cells and cell replacement therapy: making the right cells.* Clin Sci, 108(1), pp. 13-22.

Chapter 3

Experimental methodology

UNCD thin films were grown on *n*-type mirror polished silicon (100) substrates using microwave plasma enhanced chemical vapor deposition (MW-PECVD) system. Prior to ultra-sonification in diamond powder (30 nm) slurry of methanol solution, silicon substrates were cleaned using standard chemical procedure to remove surface oxide layer and other contaminants. The substrates were then cleaned and blown dried using nitrogen gas. The UNCD films were grown at different composition gas plasma atmospheres at 1200W (2.45 GHz) in a 120 Torr chamber pressure. The total gas flow rate was 100 sccm; which contained 85-90 sccm CH_4+Ar, 5–10 sccm H_2 with 5 sccm of N_2 gas. The estimated temperature of the substrates during growth was ~475 ^{0} C, which could have increased during the bombardment of species. The thickness of the deposited films was estimated using a cross sectional field emission SEM images to be ~200 nm. A very few amounts of nitrogen content (0.48- 1.32at %) was found in the UNCD film structure that was estimated from the elemental and compositional analysis XPS measurements. Material properties such as microstructural, electronic, and bonding were studied using XRD, FE-SEM, FTIR, Raman, XANES, XPS and UV-PES techniques.

3.1 Deposition/synthesize process of UNCD

Ultra-nanocrystalline diamond (UNCD) has been synthesized by means of hot filament CVD (HF-CVD), catalytic CVD, radio frequency (RF), direct-current (DC) and microwave plasma enhanced CVD (MPECVD) in hydrocarbon gas mixtures such as CH_4 or C_2H_6 diluted by H_2 [1-6].

3.1.1 Plasma enhanced chemical vapor deposition

For the synthesis of UNCD by the chemical deposition process, the influence of the nucleation density on the morphology of the films was varied between 1 x 10^8 cm^{-2} and 1 x 10^{10} cm^{-2}. This could be done by variation of the amount of ultra-disperse diamond powder (3-5 nm) added to the nanocrystalline diamond powder (250 nm) used for the ultrasonic pre-treatment of the silicon substrates.

Deposition set-up and conditions

Ultra-nanocrystalline diamond (UNCD) thin films are prepared by microwave plasma chemical vapor deposition (MWCVD) [7]. An MPECVD system (1.5 kW, 2.45 GHz, SEKI, Japan) is generally used for the synthesis of UNCD films in Ar$^+$ diluted CH4 (1–3%) with N2 (1–50%) additives. Prior to the deposition, oxidized *p- or n*-type (100) silicon substrates were immersed in a dimethyl sulfoxide (DMSO) solution containing detonation produced diamond nanoparticles which is under ultrasonic agitation for diamond nanoparticles to adhere on the substrate surface as diamond nuclei. Substrates were placed on a resistively heated molybdenum substrate holder. A thermocouple temperature sensor was inserted into the back side of the substrate holder for temperature measurements while a dual-colour optical pyrometer was aimed at the substrate surface for non-contact measurement of the substrate temperature when the process plasma was turned off.

The substrate holder was preheated to 800°C in vacuum by the resistive heater before MPECVD process begins. The surface temperature of the substrate measured by an optical pyrometer in vacuum is 50–100°C lower than that of the substrate holder. During the deposition process, additional plasma heating and gas cooling resulted in the substrate temperature become higher or lower than the 800°C preheated substrate holder temperature. The measured temperatures were 760, 860 and 890°C for substrates after MPECVD processes in Ar-diluted

1, 2 and 3% CH4 with 20% N2 additive, respectively. The substrate temperature increased with CH4 content in the gas mixture. It indicated that heat flux to the substrate was higher for process plasma in a gas mixture with a higher percentage of CH4. Substrate temperature at around 800°C was favourable for the growth of UNCD thin films.
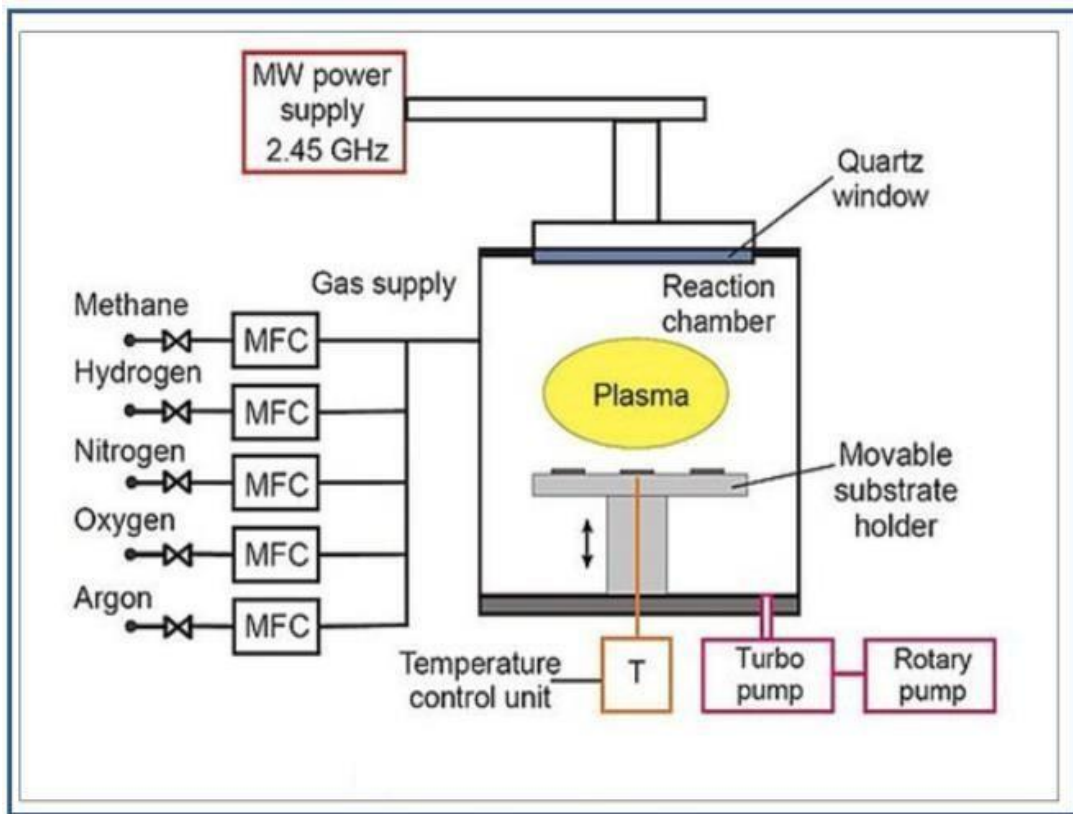
Figure 3.1: Schematic diagram of plasma enhanced chemical deposition

The reactor chamber is evacuated by a rotary vane pump to a base pressure of 8 mTorr. Process gases are fed through electronic mass flow controllers into the CVD chamber. The gas pressure is controlled by a throttle valve and a gas independent capacitive manometer. Unless otherwise stated, each MPECVD process is carried out in Ar-diluted 1, 2, or 3% CH4 with 20%–50% N2 additives at 90 Torr gas pressure under 1000 W applied microwave power for 1 hr. At the gas pressure of 90 Torr, frequent scattering by plasma species reduces the energy of ions bombarding the substrate.

The experiments were also performed at a substrate temperature of 600°C, a working pressure of 22 mbar, and a MW plasma input power of 800 W; the duration of the deposition process was 390 min. The films were grown onto monocrystalline (100) silicon wafers, etched in NH4F/HF and then pre-treated ultrasonically in a suspension of diamond powder in n-pentane to enhance the nucleation density. The pre-treatment suspension always contained 50 mg of NCD powder with a mean grain size of 250 nm, to which variable amounts (up to 80 mg) of ultra-disperse diamond (UDD) powder with a mean grain size 3–5 nm was added.

3.1.2 Hot-filament chemical vapor deposition (HF-CVD)

UNCD films could be deposited using a hot-filament chemical vapor deposition (HFCVD) system on single-crystal silicon (111) wafers [8]. In this process, the carbon source is acetone, the volume ratio between acetone and hydrogen is 1%–2% with a total gas flow rate of 200 ml/min, the working pressure in the reaction chamber was 0.5–1.4 kPa, and the temperature of the substrate was approximately 850 ^{0}C. The thickness of the as-deposited UNCD films was approximately ~5 μm could be obtained at a growth rate of ~1.5 μm/h. The C^+ implantation was performed on as-deposited UNCD films with an implantation energy of 90 keV and dose of 10^{12} cm^{-2}. For room temperature implantations, there is a universal critical damage density (10^{22} vacancies/cm^3), which, when exceeded, leads to complete graphitization of heavily damaged diamond crystals upon annealing [9]. It was reported that the C^+ implantation level of 10^{12} cm^{-2} at room temperature was significantly below the critical dose of (2–3) $\times 10^{15}$ cm^{-2} [10]. The C ions were implanted into diamond with an average ion range of 121 nm, creating 10^{19} vacancies/cm^3 in the meantime. The implanted samples were annealed at 500-1000 °C for 30 min at a pressure of 4000 Pa (80% N_2 and 20% O_2) to obtained different grain size UNCD.

May et al. [11] synthesized UNCD thin films using a standard HF-CVD reactor operating at a pressure of 100 Torr using high purity Ar, CH_4 and H_2 as source gases. Mass flow controllers

were used to control the ratios of the three gases. [Ar]/([Ar]+[H2]) was kept constant at 80%, and that of [CH4]/([H2]+[CH4]) at 1.5%, which puts it in the UNCD growth region of the Ar/CH4/H2 composition diagram [12]. The filament was made from 0.25 mm-diameter Ta metal, wound around a 3 mm-diameter core to produce a 2 cm-long coil that was positioned 5.5 mm from the substrate surface. The filament temperature was kept constant at 2400ºC and monitored using a 2-colour optical pyrometer. The substrate was single crystal Si (100) which had been manually abraded prior to deposition using 1-3 µm diamond grit, and then ultrasonically cleaned with propan-2-ol. The substrate was on a separate heater to give additional uniform heating and to maintain it at a temperature of ~850-900ºC (also measured using the optical pyrometer). Typical deposition times were 8 h. The schematic representation of the of a process in the HFCVD system used for the UNCD film deposition is given in the figure 3.2.
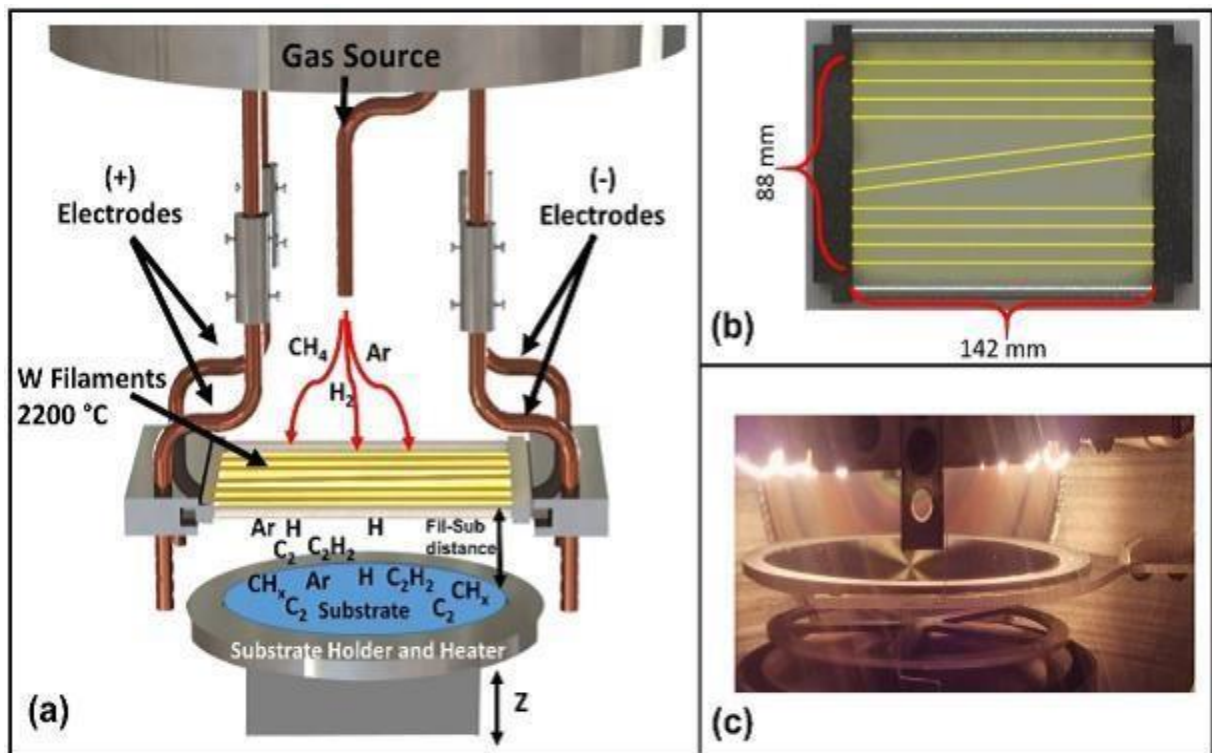

Figure 3.2: *Schematic representation of the HFCVD-substrate geometrical arrangement and gas flow and species involved in the UNCD film growth process via the HFCVD system [16].*

3.2 X-Ray diffraction (XRD) measurement

X-ray diffraction is based on constructive interference of monochromatic X-rays and a crystalline sample. These X-rays are generated by a cathode ray tube, filtered to produce monochromatic radiation, collimated to concentrate, and directed toward the sample. The interaction of the incident rays with the sample produces constructive interference (and a diffracted ray) when conditions satisfy Bragg's Law ($n\lambda = 2d \sin \theta$). This law relates the wavelength of electromagnetic radiation to the diffraction angle and the lattice spacing in a crystalline sample. These diffracted X-rays are then detected, processed, and counted. By scanning the sample through a range of 2θ angles, all possible diffraction directions of the lattice should be attained due to the random orientation of the powdered material. Conversion of the diffraction peaks to d-spacings allows identification of the mineral because each mineral has a set of unique d-spacings. Typically, this is achieved by comparison of d-spacings with standard reference patterns.

X-ray diffractometers consist of three basic elements: An X-ray tube, a sample holder, and an X-ray detector. X-rays are generated in a cathode ray tube by heating a filament to produce electrons, accelerating the electrons toward a target by applying a voltage, and bombarding the target material with electrons. When electrons have enough energy to dislodge inner shell electrons of the target material, characteristic X-ray spectra are produced. These spectra consist of several components, the most common being K_α and K_β. K_α consists, in part, of $K_{\alpha 1}$ and $K_{\alpha 2}$. $K_{\alpha 1}$ has a slightly shorter wavelength and twice the intensity as $K_{\alpha 2}$. The specific wavelengths are characteristic of the target material (Cu, Fe, Mo, Cr). Filtering, by foils or crystal monochromators, is required to produce monochromatic X-rays needed for diffraction. $K_{\alpha 1}$and $K_{\alpha 2}$ are sufficiently close in wavelength such that a weighted average of the two is used. Copper is the most common target material for single-crystal diffraction, with CuK_α radiation $=$

1.5418Å. These X-rays are collimated and directed onto the sample. As the sample and detector are rotated, the intensity of the reflected X-rays is recorded. When the geometry of the incident X-rays impinging the sample satisfies the Bragg Equation, constructive interference occurs and a peak in intensity occurs. A detector records and processes this X-ray signal and converts the signal to a count rate which is then output to a device such as a printer or computer monitor. The geometry of an X-ray diffractometer is such that the sample rotates in the path of the collimated X-ray beam at an angle θ while the X-ray detector is mounted on an arm to collect the diffracted X-rays and rotates at an angle of 2θ. The instrument used to maintain the angle and rotate the sample is termed a *goniometer*. For typical powder patterns, data is collected at 2θ from ~5° to 90°, angles that are pre-set in the X-ray scan.

X-ray powder diffraction is most widely used for the identification of unknown crystalline materials (e.g. minerals, inorganic compounds). Determination of unknown solids is critical to studies in geology, environmental science, material science, engineering, and biology. Other applications include:

- characterization of crystalline materials
- identification of fine-grained minerals such as clays and mixed layer clays that are difficult to determine optically
- determination of unit cell dimensions
- measurement of sample purity

With specialized techniques, XRD can be used to:

- determine crystal structures using Rietveld refinement
- determine of modal amounts of minerals (quantitative analysis)
- characterize thin films samples by:

- determining lattice mismatch between film and substrate and to inferring stress and strain

- determining dislocation density and quality of the film by rocking curve measurements

- measuring superlattices in multi layered epitaxial structures

- determining the thickness, roughness and density of the film using glancing incidence X-ray reflectivity measurements

- make textural measurements, such as the orientation of grains, in a polycrystalline sample.

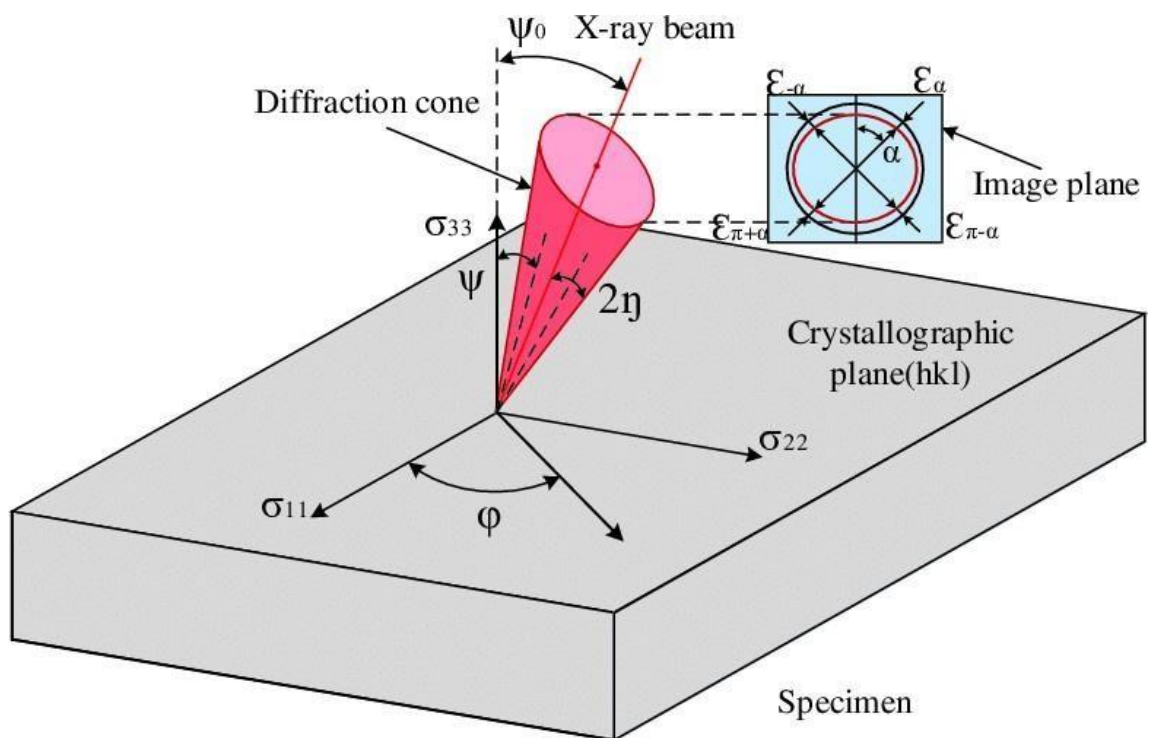XRD schematic representation is given figure 3.3.

Figure 3.3: *X-ray diffraction (XRD) schematic diagram. X-ray diffraction (XRD) schematic diagram (Shen, Qi & Zhanqiang, Liu & Hua, Yang & Zhao, Jinfu & Lv, Woyun & Mohsan, Aziz Ul Hassan. (2018). Effects of Cutting-Edge Microgeometry on Residual Stress in Orthogonal Cutting of Inconel 718 by FEM. Materials. 11. 1015. 10.3390/ma11061015.).*

3.3 Scanning Electron Microscopy (SEM) Measurement

A scanning electron microscope (SEM) is a type of electron microscope that produces images of a sample by scanning the surface with a focused beam of electrons. The electrons interact with atoms in the sample, producing various signals that contain information about the surface topography and composition of the sample. The electron beam is scanned in a raster scan pattern, and the position of the beam is combined with the intensity of the detected signal to produce an image. In the most common SEM mode, secondary electrons emitted by atoms excited by the electron beam are detected using a secondary electron detector (Everhart-Thornley detector). The number of secondary electrons that can be detected, and thus the signal intensity, depends, among other things, on specimen topography. SEM can achieve resolution better than 1 nm.

Specimens are observed in high vacuum in conventional SEM, or in low vacuum or wet conditions in variable pressure or environmental SEM, and at a wide range of cryogenic or elevated temperatures with specialized instruments [13].

The signals used by a scanning electron microscope to produce an image result from interactions of the electron beam with atoms at various depths within the sample.

Various types of signals are produced including secondary electrons (SE), reflected or back-scattered electrons (BSE), characteristic X-rays and light (cathodoluminescence) (CL), absorbed current (specimen current) and transmitted electrons. Secondary electron detectors are standard equipment in all SEMs, but it is rare for a single machine to have detectors for all other possible signals.

Secondary electrons have very low energies on the order of 50 eV, which limits their mean free path in solid matter. Consequently, SEs can only escape from the top few nanometers of the surface of a sample. The signal from secondary electrons tends to be highly localized at the point of impact of the primary electron beam, making it possible to collect images of the sample surface with a resolution of below 1 nm. Back-scattered electrons (BSE) are beam electrons that are reflected from the sample by elastic scattering. They emerge from deeper locations within the specimen and, consequently, the resolution of BSE images is less than SE images. However, BSE are often used in analytical SEM, along with the spectra made from the characteristic X-rays, because the intensity of the BSE signal is strongly related to the atomic number (Z) of the specimen. BSE images can provide information about the distribution, but not the identity, of different elements in the sample. In samples predominantly composed of light elements, such as biological specimens, BSE imaging can image colloidal gold immuno-labels of 5 or 10 nm diameter, which would otherwise be difficult or impossible to detect in secondary electron images.[13] Characteristic X-rays are emitted when the electron beam removes an inner shell electron from the sample, causing a higher-energy electron to fill the shell and release energy. The energy or wavelength of these characteristic X-rays can be measured by Energy-dispersive X-ray spectroscopy or Wavelength-dispersive X-ray spectroscopy and used to identify and measure the abundance of elements in the sample and map their distribution.

Due to the very narrow electron beam, SEM micrographs have a large depth of field yielding a characteristic three-dimensional appearance useful for understanding the surface structure of a sample.[14] This is exemplified by the micrograph of pollen shown above. A wide range of magnifications is possible, from about 10 times (about equivalent to that of a powerful hand-

lens) to more than 500,000 times, about 250 times the magnification limit of the best light microscopes, Schematic representation of the SEM is given in figure 3.4.
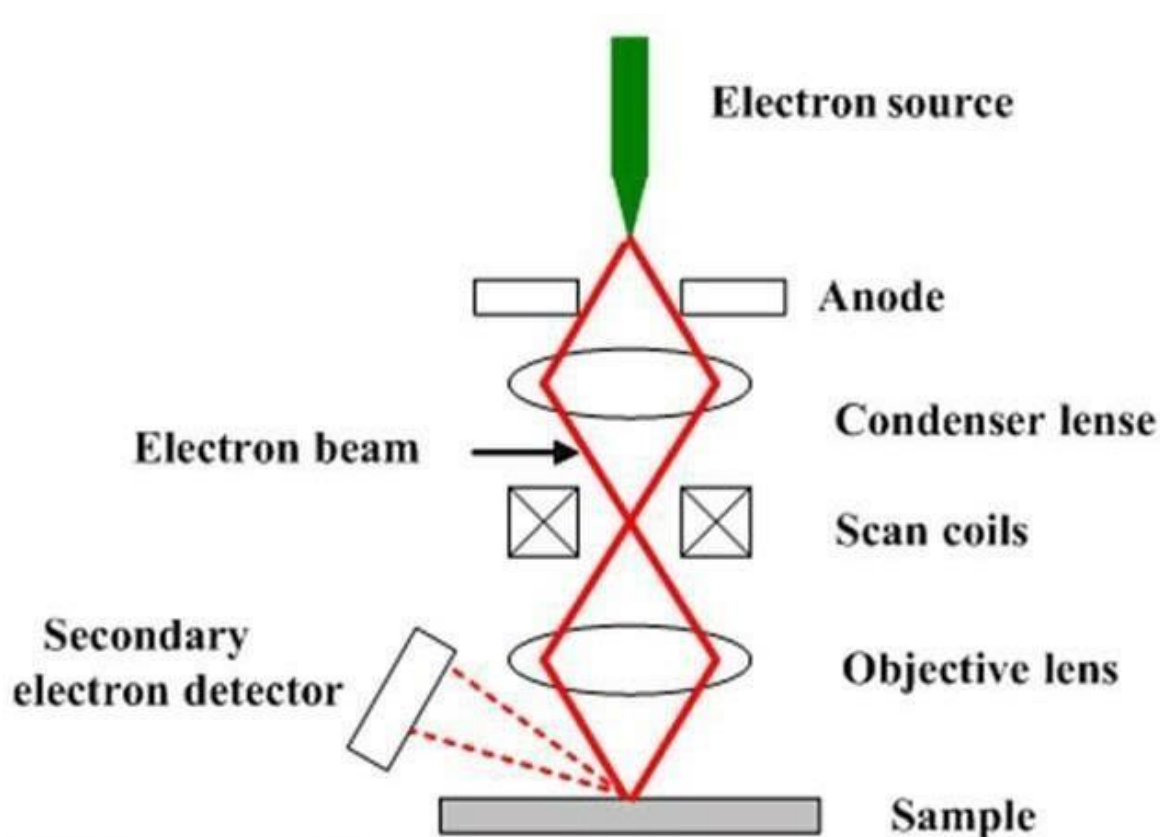
Figure 3.4: *A schematic diagram of scanning electron microscope (Peiris, T. A. Nirmal. (2014). Microwave-assisted processing of solid materials for sustainable energy related electronic and optoelectronic applications.).*

3.4 Raman Spectroscopy Measurement

Raman spectroscopy named after its founder C.V Raman, is a very powerful tool to determine the chemical and structural properties of liquid or solid materials using a simple non-destructive and non-contact method of measurement both qualitatively and quantitively. It has several advantages over other conventional techniques including the ability to rapidly cover wide measurement range (50 cm^{-1} to 4000 cm^{-1}) and distinguish between sp^3 and sp^2 bonds in carbon materials and no sample preparation. Qualitative analysis can be performed by measuring the

frequency of scattered radiations while quantitative analysis can be measured by measuring the intensity of scattered radiations [17]. The spectrum profile gives an extensive chemical fingerprint that can be used for identifying a material and differentiating it from others. The intensity of a spectrum is directly proportional to concentration [20]. Typically, a calibration procedure will be used to determine the relationship between peak intensity and concentration, and then routine measurements can be made to analyze for concentration [20].

Raman spectroscopy is based on the interaction of light with the chemical bonds within a material. When monochromatic light interacts with the molecules within a material, light is scattered. Most of the scattered light is at the same wavelength (or color) as the laser source and does not provide useful information – this is called Rayleigh Scatter [23]. A small amount of light (1 in a million) is scattered at different wavelengths which depend on the chemical structure of the analyte – this is called Raman Scatter [23]. Rayleigh scattering leads to no change in energy whereas Raman scattering leads to change in energy resulting in anti-stokes-$h(v_0+v_n)$ and stokes-$h(v_0-v)$. The change in energy from molecular vibration is collected by the Raman spectrum. Several peaks displaying intensity and wavelength position of the Raman scattered light are presented by the Raman spectrum. Each peak corresponds to a specific molecular bond vibration, including individual bonds such as C-C, C=C, N-O, C-H etc. [23]. Schematic representation of the theory of Raman Spectroscopy is given in figure 3.5.
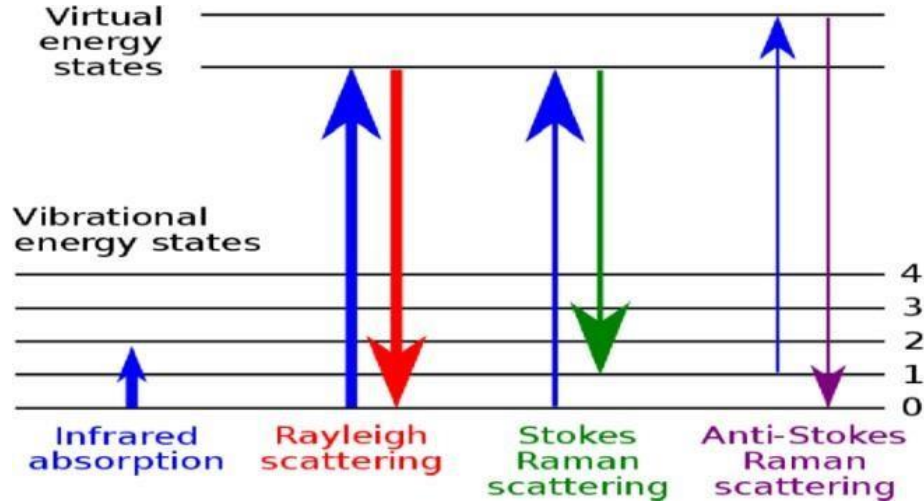
Figure 3.5: *Schematic representation of the Raman Spectroscopy theory [56].*

Raman spectroscopy is also used for establishing the crystalline quality of diamond thin films. This is done by estimation of sp^2 -bonded carbon in films. Difficulty arises when Raman spectroscopy is used to examination the structure of carbon films with a mixture of sp^2- and sp^3-bonded carbon in several different bonding configurations that possess different short- and large range order as is found in nanocrystalline diamond and amorphous carbon films [21]. Using the laser with wavelength in the visible region makes the energy of incident photons to be lower than that of the band gap for sp^3 bonded carbon resulting in a larger Raman scattering cross section for sp^2 carbon than sp^3 carbon attributed to the resonant Raman effect. The spectra observed are thus completely by Raman scattering from sp^2-bonded carbon, even when a significant amount of carbon in the sample is sp^3 bonded [21], the problem resulting from the use of ultraviolet excitation measurements with photon energy being shifted to a higher sp^3 carbon local gap at approximately 5.5 eV.

It is well known that the Raman spectrum of a single crystal diamond is characterized with a sharp single band at 1332 cm^{-1} corresponding to the sp^3 hybridization of diamond [24]. The graphite spectrum has two bands at 1350 cm^{-1} and 1580 cm^{-1} representing the disordered carbon and the graphitic bands. Both bands are the sp^2 carbon signatures. For a microcrystalline

31

diamond, a sharp peak at 1332 c m^{-1} (*sp^3* diamond) is predominant while the nanocrystalline diamond films mostly exhibit the scattering due to sp^2 carbon, even though most of the film is *sp^3* bonded as the visible Raman spectrum is more sensitive.

3.5 Fourier Transform Infra-Red (FTIR) Measurement

Fourier Transform-Infrared Spectroscopy (FTIR) is an analytical technique used to identify organic (and in some cases inorganic) materials [26]. It is a non-destructive, real time measurement and relatively easy to use technique, and offers quantitative and qualitative material analysis. Absorption of infrared radiation by the sample material versus wavelength is measured, and molecular components and structures are identified by the infrared absorption bands. The spectrum is obtained by measuring the interferogram of the sample using the interferometer, the Michaelson interferometer. A Fourier transform is then performed on the interferogram to obtain the spectrum. When the infrared light at wavelength λ enters the Michelson interferometer, if the optical path difference is an integer multiple, the peaks and valleys superimpose, increasing the light intensity [31]. The light intensity weakens when the optical path difference is a half-integer multiple (integer + 1/2). The intensity I(x) at the optical path difference x is expressed as:

$$I(x) = \frac{1}{2}P(\lambda)[1 + 2\pi x] \qquad (3.1)$$

where P(λ) is the original light intensity. The interferogram with respect to infrared light at wavelength λ is formed by the AC component (cos). As the light emitted by the light source combines at various wavelengths, the interferogram obtained is the sum of the expression above at various wavelengths λ. For a zero optical path difference (OPD), light is reinforced at all wavelengths in such a way that the interferogram exhibits high intensity. This is called "center burst" [31].

Applying Fourier transform to an interferogram, light intensity is obtained at each wavelength. For an interferogram created at continuous wavenumbers where wav, the light intensity is expressed as:

$$I(x) = \int_0^\infty S(v)\cos(2\pi vx)dv \qquad (3.2)$$

where

$$S(v) = \int_0^\infty I(x)\cos(2\pi x)dx \qquad (3.3)$$

where $S(v)$ is the infrared light intensity at wavenumber v. A schematic diagram of FTIR measurements is shown in figure process is shown in the figure below.
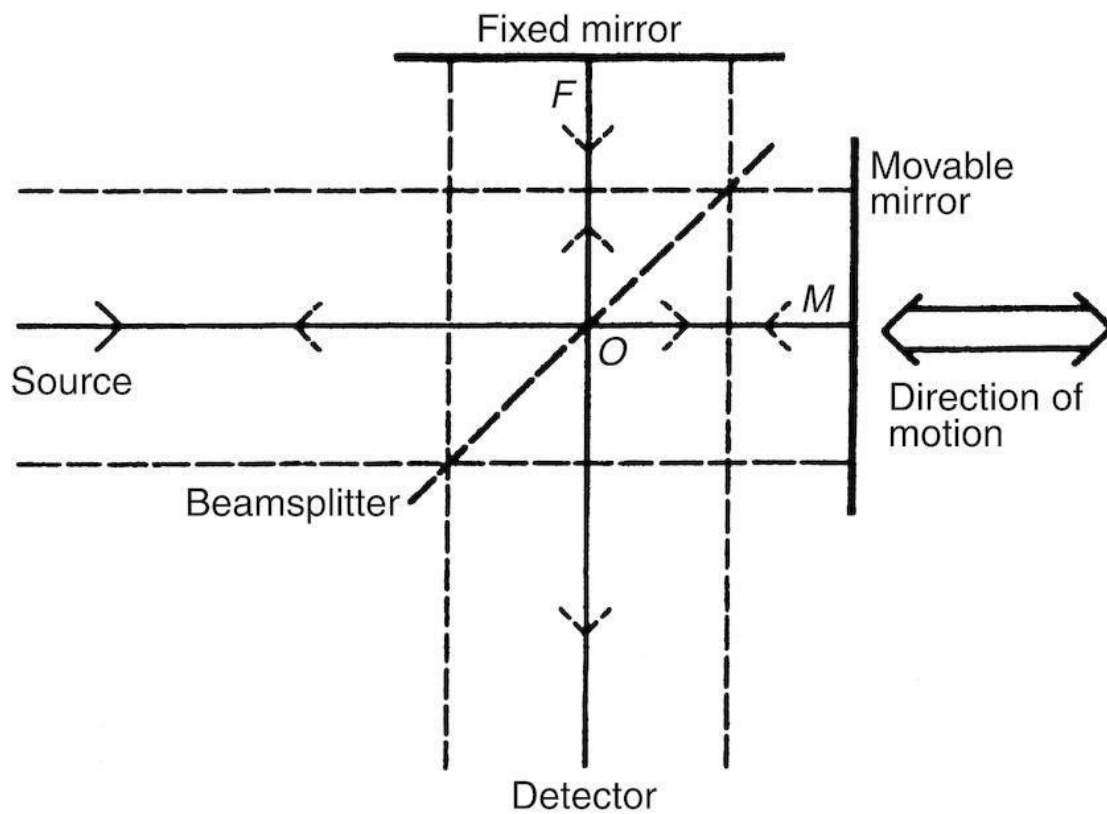
Figure 3.6: *Schematic diagram of a FTIR spectrometer based on the Michelson interferometer. The median ray is shown as a solid line, and the extremes of the collimated beam are shown as broken lines [29].*

FTIR spectroscopy is well known for the analysis of the impurities in diamond and investigating the chemical bonding structures comprised of carbon and hydrogen atoms in a-C:H [27]. Hydrogen content in the a-C:H can be quantitatively estimated using this technique.

The absorption features found in diamond films are the intrinsic two phonon absorption from 1500-2700 cm^{-1}, one phonon absorption at 1000-1350 cm^{-1} and the hydrogen related C-H stretch absorption from 2800-3000 cm^{-1} [28,30]. For complicated structures such as UNCD/ a-C:H with large numbers of UNCD grains embedded in the a-C:H matrix, the FTIR technique enables us to detect the chemical bonds at the a-C:H matrix as well as at the grain boundaries.

3.6 Nano-Indentation Measurement System (Young's modulus & Hardness)

Nano-indentation, also known as the instrumented indentation testing, is the widely used technique for determining mechanical properties (e.g. hardness & modulus) of materials. Most notably, this technique does not need any sample preparation and can measure properties for various materials ranging from hard superalloys to soft biomaterials within seconds making it the fastest technique for such measurements [37]. Load and depth are the basic measurements required for performing nano-indentation experiments. The indenters of different geometries such as Berkovich for E and H, spherical for stress-strain, flat punch for complex modulus, cube corner for fracture toughness, spherical cone for scratch measurements, wedge for 3-point bending can be used to measure the properties a user is interested in [37]. The schematic representation of the nano-indentation process is given in figure 3.7

Industry and universities mostly use this technique for characterizing thin films. This technique is very sensitive to the substrate properties. Therefore, the contact depth should be kept to less than (10-20) % of the film thickness to circumvent the substrate effect. Additionally, the hardness and Young's modulus values obtained from the measurements can depend significantly on whether the shape of the blunt tip as well as the substrate effects were considered. In 1992, Oliver & Pharr developed a method for calculating hardness and modulus from the load curves. The method is based on the material's contact with a known material,

commonly diamond. Schematic representation of the nano-indentation process is given in figure 3.7.

$$h_c = h - \varepsilon \frac{P}{S}$$

$$A = f(h_c)$$

$$H = \frac{P}{A}$$

$$E = \frac{\sqrt{\pi}}{2} \frac{S}{\sqrt{A}}$$
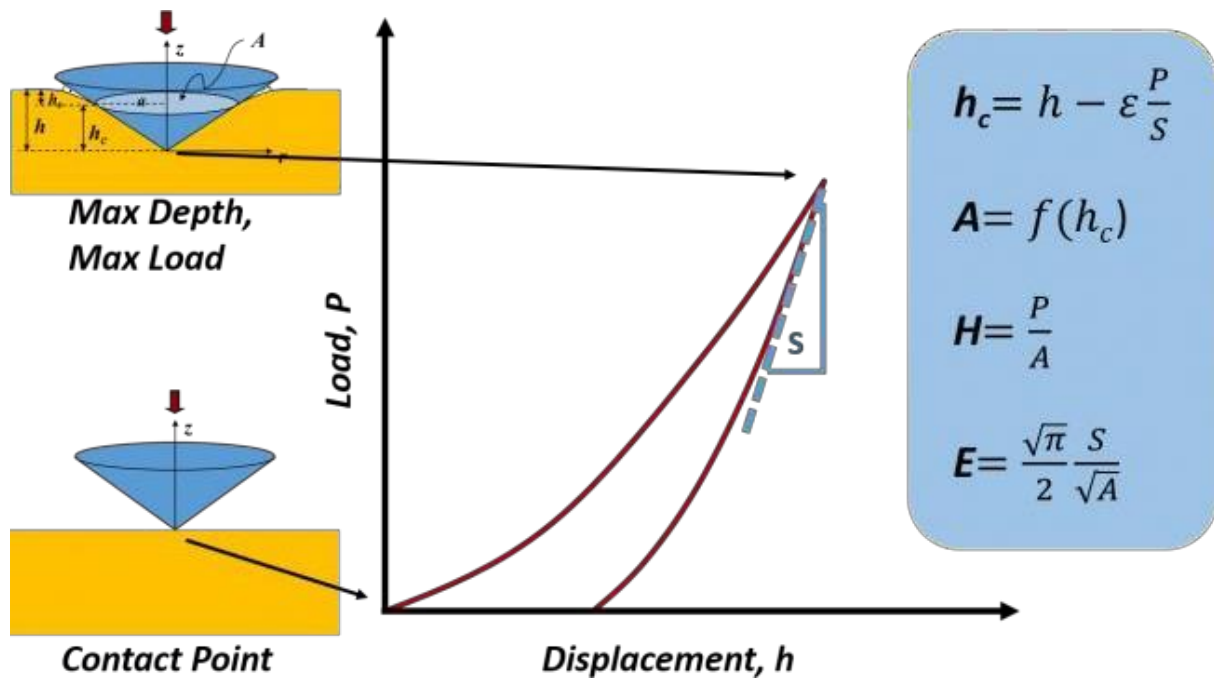
Figure 3.7: *Schematic of the nano-indentation process [37]*

3.7 X-rays Photoelectron Spectroscopy (XPS) Measurement System

X-ray Photoelectron Spectroscopy (XPS), also referred to as the Electron Spectroscopy for Chemical Analysis (ESCA) is an analytical method for characterizing material surfaces. It uses the photoelectrons excited by X-ray radiation and released from the material into vacuum. The technique is widely used due to its simplicity in use and data interpretation, application in a wide range of materials as well as the provision of vital quantitative and chemical state information of the material under study. The analysis depth is approximated to be 5 nm, making it a very suitable tool for the compositional analysis of ultra-thin layers and thin micro-scale features. The electrons in the (solid) sample are characterized by their binding energies (BE), which depend on the element of its origin [41]. Using only the elastically scattered electrons

(electrons without energy losses) emitted from the sample, information about the composition of the sample can be derived from their energy spectrum [41]. All elements on the periodic table except helium and hydrogen, due to their low sensitivity in the valence band are detected by different characteristic BE peak. The detection limits depend on the element and are typically in the range 0.1–0.5 at% [41]. Low energy X-rays from an aluminium or magnesium source (typically Mg-Kα or Al-Kα at 1253.6 and 1486.6 eV respectively) are commonly used [43]. The kinetic energy of ejected photoelectrons is measured by the analyzer and is transformed into binding energy as follows:

$$E_B = h\upsilon - \phi - E_K$$

(3.4)

where: E_B = Electron binding energy /eV

h = Plancks constant /eV.s

υ = Frequency of incident radiation /s^{-1}

ϕ = Surface work function /eV

:E_K = Kinetic energy of emergent electron /eV [43].

XPS is used for measuring the following

- elemental composition of the surface (top 1–10 nm usually)

- empirical formula of pure materials

- elements that contaminate a surface

- chemical or electronic state of each element in the surface

- uniformity of elemental composition across the top surface (or line

- profiling or mapping)

- uniformity of elemental composition as a function of ion beam

- etching (or depth profiling) [42].

The XPS process is schematically represented in figure 3.8.
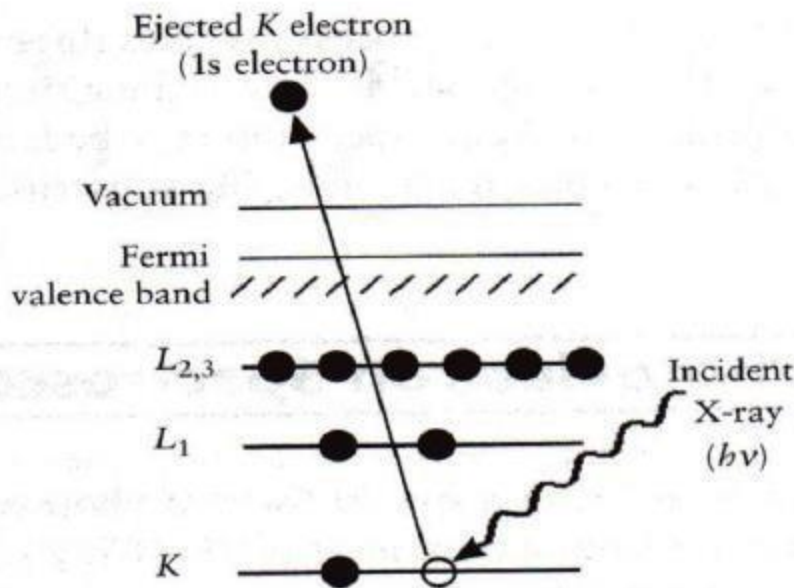
Figure 3.8: *Schematic representation of the XPS process [43].*

3.8 Ultra-Violet Photoelectron Spectroscopy (UPS) Measurement

Ultraviolet Photoelectron Spectroscopy is a robust tool for probing the valence energy levels and chemical bonding of the material's surface. In this technique, the sample under investigation is irradiated using vacuum UV photons of energy hv, created in a continuous discharge source by applying high voltage to a gas to cause breakdown [55]. The energies range from 10- 50 eV which is greater than the typical work-function values (2-5 eV) [46]. Noble gas discharge lamps are used as radiation sources. Helium I (21.2 eV) or He II (40.8 eV) is mostly used. Such photons exciting energy is of the same order of magnitude as the binding energies of outermost levels of atoms and that's why only the photoelectrons emitted from the valence band or the shallow core levels can be detected while the deep core electron levels cannot be excited [55]. UPS is very surface (to a depth of around 10nm) sensitive and hence more susceptible to surface contamination. UPS is mostly used in studying the adsorption as well as valence band structures of metals, alloys and semiconductors due to high photo-ionization

cross-section of valence electrons when using ultraviolet light. Angle-resolved UPS can be obtained by polarized incident light coupled with variable angle of detection, for the provision of vital information about the orientation of molecular orbitals and structural modifications of adsorbed species on surfaces. UPS can also be used wide band gap semiconductor (diamond) surface electron affinity measurements. The material's work-function can also be extracted from the spectrum's secondary electron cut-offs. The advantage of using UPS over conventional photoelectron spectroscopies is that UPS has a very narrow line width and a high flux of photons available from simple discharge sources. Fine structures due to vibrational levels of the molecular ion which allowing molecular orbital assignment of specific peaks can be observed using high resolution UPS scans. The schematic diagram of the UPS instrument is depicted in figure 3.9.
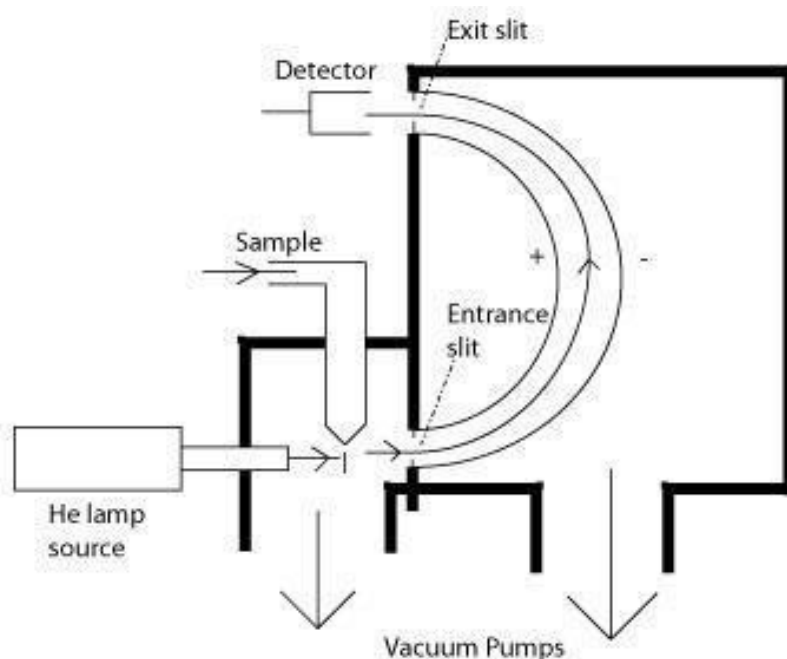
Figure 3.9: *Schematic of a basic UPS instrument [55].*

3.9 X-Ray Absorption Near Edge Structure (XANES) Spectroscopy Measurement

X-ray absorption near-edge structure also called NEXAFS (near-edge X-ray absorption fine structure) exists in the energy level of 50 eV above the absorption edge [50]. It is used largely to study the local structure and electronic states of gas-phase, molecular and condensed matter using the synchrotron radiation. In XANES, a photon is absorbed, and an electron is excited from a core state to an empty state [48]. The electron of a specific core level is excited only if the photon energy is equal or higher than the binding energy of that core level. The energy of an absorption edge therefore corresponds to the core-level energy, which is characteristic for each element, making XANES an element-selective technique [48]. In addition to element selectivity, the other advantages of the XANES is the possibility to obtain detailed information in the absence of long-range order. It can provide a detailed picture of the local electronic structure of the element studied. In XANES, the changes in the absorption of X-rays due to the photoelectric effect is measured. The XANES spectrum is given by the absorption cross section µ [48]. When the X-ray passes an electron, its electric field oscillates in both direction and strength, allowing the electron to capture the energy. Features studied by the XANES include:

- The edge position (a primary indicator of oxidation state)

- "pre-edge" features

- intensity, number, position, and shape of peaks at the top of the main edge.

Schematic diagram of the XANES process is shown in figure 3.10.
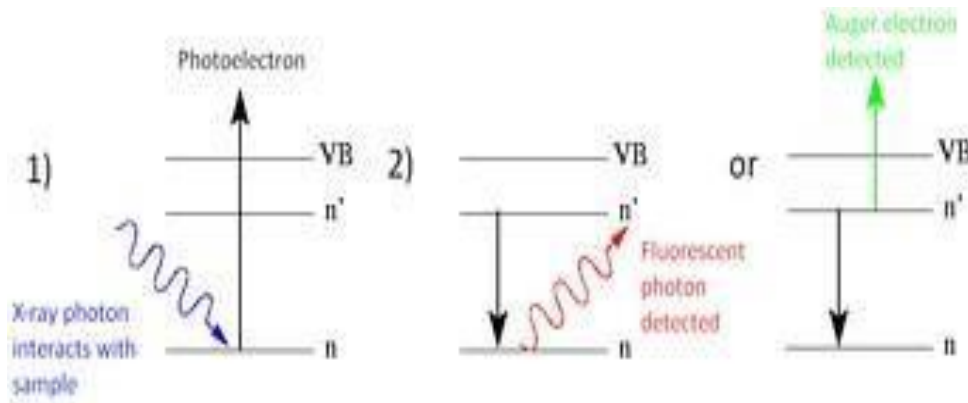
Figure 3.10: *The fundamental processes which contribute to XANES spectra: 1) photo absorption of an x-ray into a core level followed by photoelectron emission, followed by either 2) (left) filling of the core hole by an electron in another level, accompanied by fluorescence; or (right) filling of the core hole by an electron in another level followed by emission of an Auger electron (https://wiki2.org/en/X-ray_absorption_near_edge_structure).*

3.10 Current (I) - Voltage (V) Measurement

Current-Voltage(I-V) measurements are used for probing the electrical characteristics of a material. More information about the material's electrical properties are extracted from the current-voltage curves. These characteristic curves are graphical representation of the relationship between the voltage applied across the device and the current flowing through the device. Fundamental properties of electronic devices can also be extracted from these curves. A basic aspect of the operation of an electronic device can be deduced from the position of the curve on the I-V graph [54] which is divided into four quadrants. The graph's quadrants provide information on whether the device is passive or active. The device with a curve in the first and third quadrants is passive (resistor, diode), while the device with the curve in the second and fourth and quadrants is active (solar cell).

Electronic devices have different IV-curves. A resistor has the simplest form of the I-V curve depicting a linear relationship between the applied voltage and the resulting current, obeying the Ohm's law: $I = V/R$ with the slope being $1/R$. Diodes and solar cells on the other hand

depict a non-linear relationship between the applied voltage and the current passing through them and thin films portray the hysteresis loop characteristic. The hysteresis loop characteristics may be due to various factors such as:

- Channel film thickness

- Hydrogenation treatment

- Sweeping gate voltage range

- Temperature.

I-V curves of different devices (resistor, diode, solar cell) are shown in figure 3.11.
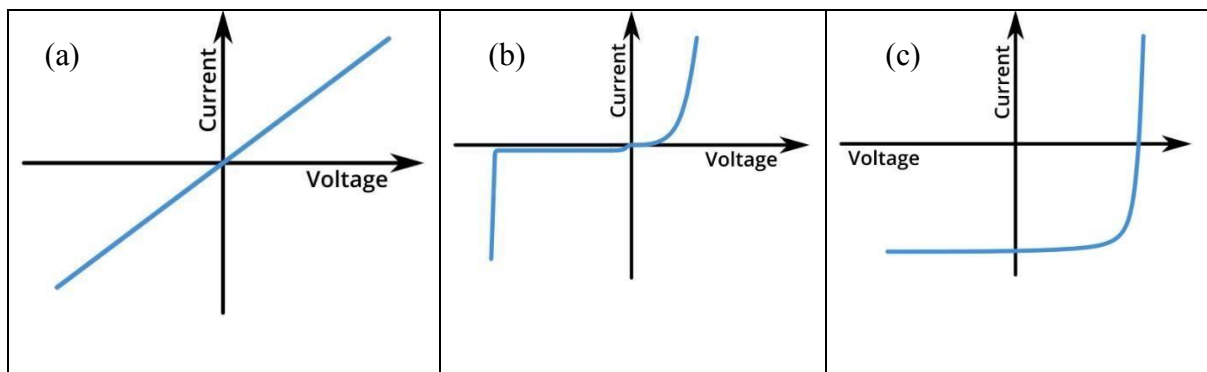
Figure 3.1: *Current-voltage characteristics of (a) resistor, (b) diode and (c) solar cell [54].*

References

[1]   Tzeng, Y., Chen, C.-L., Chen, Y.-Y., Liu, C.-Y., 2010. *Carbon nanowalls on graphite for cold cathode applications*. Diam. Relat. Mater., 19(2-3), pp. 201–204.

[2]   Dikonimos, T.H, 2007. *DC plasma enhanced growth of oriented carbon nanowall films by HFCVD*. Diam. Relat. Mater., 16(4-7), pp. 1240–1243.

[3]   Itoh, T., Shimabukuro, S., Kawamura, S., Nonomura, S., (2006). *Preparation and electron field emission of carbon nanowall by Cat-CVD*. Thin Solid Films, 501(1-2), pp. 314– 317.

[4]   Wu, Y., Qiao, Chong, P., T., Shen, Z., 2002. *Carbon nanowalls grown by microwave plasma enhanced chemical vapor deposition*. Adv. Mater., 14(1), pp.64–67.

[5]   Nishimura, K., Jiang, N. & Hiraki, A., 2003. *Growth and characterization of carbon nanowalls*. IEICE Trans Electron E86–C, 86(5), pp. 821–824.

[6]   Tanaka, K., Yoshimura, M., Okamoto, A. & Ueda, K., 2005. *Growth of carbon nanowalls on a SiO$_2$ substrate by microwave plasma enhanced chemical vapor deposition*. Jpn. J. Appl. Phys., 44(4R), pp. 2074–2076.

[7]   Tzeng, Y., Yeh, S., Fang, W., Chu Y., 2015. *Nitrogen-incorporated ultrananocrystalline diamond and multi-layer-graphene-like hybrid carbon films*. Sci. Rep, 4, p. 4531.

[8]   Xu, H., Liu, J.J., Ye, H.T., Coathup, D.J., Khomich, A.V., Hu, X.J., 2018. *Structural and electrical properties of carbon-ion-implanted ultra-nanocrystalline diamond films*. Chin. Phys. B, 27(9), p.096104

[9]   Uzan-Saguy, C., Cytermann, C., Brener, R., Richter, V., Shaanan, M., Kalish, R., 1995. *Damage threshold for ionbeam induced graphitization of diamond*. Appl. Phys. Lett., 67(9), pp.1194-1196.

[10]   Prawer, S., Kalish, R., 1995. *Ion-beam-induced transformation of diamond*. Phys. Rev. B, 51(22), p. 15711.

[11] May, P.W., Y. A. Mankelevich, Y.A., 2007. *The Mechanism for Ultrananocrystalline Diamond Growth: Experimental and Theoretical Studies.* Mater. Res. Soc. Symp. Proc. 956, MRS, p.0956-J07-04.

[12] May, P.W., Smith, J.S., Mankelevich, Y.A., 2006. *Deposition of NCD films using hot filament CVD and Ar/CH$_4$/H$_2$ gas mixtures.* Diamond Relat. Mater., 15(2-3), pp. 345-352.

[13] Stokes, D. J., 2008. *Principles and Practice of Variable Pressure Environmental Scanning Electron Microscopy (VP-ESEM).* John Wiley & Sons.

[14] Suzuki, E., 2002. *High-resolution scanning electron microscopy of immunogold-labelled cells by the use of thin plasma coating of osmium.* J. Microsc**.,** 208 (3), pp. 153–157.

[15] Goldstein, G. I.; Newbury, D. E.; Echlin, P.; Joy, D. C.; Fiori, C.; Lifshin, E. 1981. *Scanning electron microscopy and x-ray microanalysis.* New York: Plenum Press.

[16] Alcantar-Pena, J.J. Montes J., Arellano-Jimenez, M.J., Ortega Aguilar, J.E, Berman-Mendoza, D., Garcia, R., 2016. *Low temperature hot filament chemical vapor deposition of ultra-nanocrystalline diamond films with tunable sheet resistance for electronic power devices.* Diam. Relat. Mater., 69, pp. 207–213.

[17]   Bumbrah, G.S., Sharma, R.M., 2016. *Raman spectroscopy- Basic principles, instrumentation and selected applications for characterization of drugs of abuse.* Egypt. J. Forensic Sci., 6(3), pp. 209-215.

[18] Jones, R.R., Hooper, D.C., Zhang, L., Wolverson, D., Valev, V.K., 2019. *Raman techniques: fundamentals and frontiers.* Nanoscale Res. Lett., 14(1), pp.1-34.

[19]   Horiba (https://www.horiba.com/en_en/raman-imaging-and-spectroscopy/).

[20]   Birrell, J., Gerbi, J.E., Auciello, O., G,ibson, J.M., Johnson, J., Carlisle, J.A., 2005. *Interpretation of the Raman spectra of ultrananocrystalline diamond.* Diam. Relat. Mater., 14(1), pp.86-92.

[21]   Grasselli, J.G., Snavely, M.K., Bulkin, B.J., 1980. *Applications of Raman Spectroscopy.* Phys. Rep., 65 (4), pp. 231—344.

[22]   Horiba (https://www.horiba.com/en_en/raman-imaging-and-spectroscopy/)

[23]   Jeedigunta, S., 2008. *Growth and characterization of nanocrystalline diamond films for microelectronics and microelectromechanical systems. USF Schloar Comms, 316.*

[24]   Ţucureanu, V., Matei, A., Avram, A.M., 2016. *FTIR Spectroscopy for Carbon Family Study.* Crit. Rev. Anal. Chem., 46(5), pp.502-520.

[25]   Materials Evaluation and Engineering Inc. (MEE) (https://www.mee-inc.com/hamm/fourier-transform-infrared-spectroscopy-ftir/).

[26]   Al-Riyami, S., Ohmagari, S., Yoshitake, T., 2011. *Fourier transform infrared spectroscopic study of nitrogen-doped ultrananocrystalline diamond/hydrogenated amorphous carbon composite films prepared by pulsed laser deposition.* Diam. Relat. Mater., 20(7), pp.1072-1075.

[27]   Erz, R., Diitter, W., Jung, K., Ehrhardt, K.H., 1995. *Investigation of boron and hydrogen concentrations in p-type diamond films by infrared spectroscopy.* Diam. Relat. Mater.4(4), pp. 469-472

[28]   Leclerc, D., 2000. *Fourier Transform Infrared Spectroscopy in the Pulp and Paper Industry.* Encyclopedia of Analytical Chemistry, Wiley & Sons.

[29]   Arantes, T.M., Santos, N.M., Azevedo, A.F., Baldan, M.R. and Ferreira, N.G., 2014. *Fourier transform infrared spectroscopic study of boron-doped micro/nano/ultrananocrystalline diamond prepared by chemical vapor deposition.* Mater. Sci. Forum, 802, pp. 140-145.

[30] Shimazu (https://www.shimadzu.com/an/ftir/support/tips/letter15/apodization.html).

[31] Chudoba T., 2006. *Measurement of Hardness and Young's Modulus by Nanoindentation.*

In: Nanostructured Coatings. (eds) Cavaleiro A., De Hosson J.T.M. Nanostructure Science and Technology. Springer, New York, NY.

[32] Guillonneau, G., Kermouche, G., Bec, S., Jean-Luc Loubet, J.L.,2021. *Determination of mechanical properties by nanoindentation independently of indentation depth measurement.* J. Mater. Res., 27(19), pp.2551-2560.

[33] Suk, J.W., Murali, S., An, J., Rodney S. Ruoff, R.S., 2012. *Mechanical measurements of ultra-thin amorphous carbon membranes using atomic force microscopy.* Carbon, 50(6), pp.2220-2225

[34] Yeon-Gil Jung, Y.G., Brian R. Lawn, B.R., Martynuik, M., Huang, H., Hu, X.Z., 2004. *Evaluation of elastic modulus and hardness of thin films by nanoindentation.* J. Mater. Res., 19 (10), pp.3076-3080.

[35] Chicot, D., N'Jock, M.Y., Puchi-Cabrera, E.S., Iost, A., Staia, M.H., Louis, G., Bouscarrat, G., Aumaitre, R., 2014. *A contact area function for Berkovich nanoindentation: Application to hardness determination of a TiHfCN thin film.* Thin Solid Films, pp.259-266.

[36] Nanoscience (https://www.nanoscience.com/techniques/nanoindentation/#how.)

[37] Springer (https://link.springer.com/referenceworkentry/10.1007%2F978-3-642-35950-716730-1.)

[38] Han, L., Joost J. V., 2009. *Determining the elastic modulus and hardness of an ultrathin film on a substrate using nanoindentation.* J. Mater. Res., 24(3), pp.1114-1126.

[39] Greczynski, G., Hultma, L., 2020. *X-ray photoelectron spectroscopy: Towards reliable binding energy referencing.* Prog. Mater. Sci., 107, p.100591.

[40]   Oswald, S., 2013. *XRay Photoelectron Spectroscopy in Analysis of Surfaces.* Encyclopedia of Analytical Chemistry, Wiley & Sons.

[41]   Nanohub (https://nanohub.org/resources/28936/download/MACK_U6_Simchi_XPS.pdf.)

[42]   Embong, Z., 2011. *XPS, AES and laser Raman spectroscopy: A fingerprint for a materials surface characterisation.* Jurnal Sains Nuklear Malaysia, 23(2), pp.26-45

[43]   Bubert, H., Jenett. H., 2002. *Surface and Thin flim Analysis: Principles, Instrumentation, Applications.* Wiley.

[44]   Himpsel, F.J., 2012. *Ultraviolet Photoelectron Spectroscopy.* Characterization of Materials, pp.1-13. Wiley & Sons.

[45]   Washington State University (http://www.wsu.edu/~pchemlab; 5-2669)

[46]   Ozawa K., 2018. *Ultraviolet Photoelectron Spectroscopy.* In: The Surface Science Society of Japan (eds) Compendium of Surface and Interface Analysis. Springer, Singapore.

[47]   Henderson, G.S., De Groot, F.M., Moulton, B.J., 2014. *X-ray Absorption Near-Edge Structure (XANES) Spectroscopy.* Rev Mineral Geochem,78(1), pp. 75-138.

[48]   Stohr, J. NEXAFS spectroscopy.1992. Springer-Verlag, Berlin and New York.

[49]   Medjo, R.E., 2013. *Characterization of carbon nanotubes. Physical and Chemical Properties of Carbon Nanotubes*, p.171.

[50]   Bobrov, K., Comtet, G., Dujardin, G., Hellner, L., Bergonzo, P., Mer, C., 2001. *Surface electronic states of the partially hydrogenated diamond C (100−(2×1): H surface.* Physical Review B, 63(16), p.165421.

[51] Lin, H.C., Hung, C.H., Chen, W.C., Lin, Z.M., Hsu, H.H., Hunag, T.Y., 2009. *Origin of hysteresis in current-voltage characteristics of polycrystalline silicon thin-film transistors*. J. Appl. Phys., 105(5), p.054502.

[52] Guo, W.H., Huang, J.T., Hwang, J.,1997. *Voltage characteristic of Al/boron-doped polycrystalline diamond Schottky contact*. Diamond Relat. Mater., 6(1), pp12-16.

[53] Ossila (https://www.ossila.com/pages/iv-curves-measurement)

[54] Functional Materials & Photonics Structures (https://fmps.fbk.eu/electron-spectroscopies-lab-aes-ups-xps)

[55] Chemistry Libretexts
(https://chem.libretexts.org/Bookshelves/Physical_and_Theoretical_Chemistry_Textbook_Maps/Supplemental_Modules_(Physical_and_Theoretical_Chemistry)/Spectroscopy/Photoelectron_Spectroscopy/Photoelectron_Spectroscopy%3A_Application)

[56] Mastelaro, V.R., Zanotto, E.D., 2018. *X-ray Absorption Fine Structure (XAFS) Studies of Oxide Glasses—A 45-Year Overview*. Materials, 11(2), p.204.

[57] https://en.wikipedia.org/wiki/Raman_spectroscopy.

Chapter 4

Ultra-Nano-Crystalline-Diamond (UNCD) Thin Films:

The deposition, characterization, and application of ultra-nanocrystalline diamond (UNCD) films have been extensively studied in the past few decades [1, 2] because UNCD is a promising material due to its excellent combination of chemical and physical properties such as, the excellent corrosion resistance, good chemical inertness, very smooth surface with excellent mechanical properties [3,4] *viz*. as high Young's modulus, high fracture toughness and low friction coefficient [5,6]. As a super-sealing material, UNCD films have been investigated in petroleum, chemical engineering, metallurgy, military, and other areas involving high temperature, high speed, heavy loading, and extremely corrosive and abrasive sealing conditions.

The UNCD film is a special form of diamond film that has attracted increasing attention from researchers because of its exclusive granular structure [7]. The UNCD film has ultra-small diamond grains (5–10 nm) and smooth surface characteristics. When the grain size of UNCD film is less than 10 nm, the surface smoothness is improved significantly, making it a promising material for tribological and mechanical sealing applications [5-10]. UNCD is a composite material in which nanometer sized (1–10 nm) diamond grains (sp^3 hybridized carbon atoms) are surrounded by an amorphous carbon matrix (sp^2 hybridized carbon atoms along with hydrogen). The grains of UNCD films have sp^3 character and the grain boundaries have a mixture of sp^2, sp^3, hydrocarbon, and amorphous carbon (a-C), in which the sp^2 character is predominant [11]. The grain boundaries are formed by the interfacial region of these phases. The diamond grains (crystallites) determine the mechanical properties of UNCD films and the optical and electrical characteristics, and surface chemistry are controlled by the grain boundaries [11]. Due to the π bonds, the amorphous carbon matrix is coupled, forming sp^2

clusters surrounded by the matrix of sp^3 C atoms. These clusters have π states close to the Fermi level, so these will determine the optical and electronic properties of nano-crystalline diamond films. It has been reported that n-type conduction with a high electrical conductivity was realized in a nitrogen-doped UNCD thin film [12].

In N-doped UNCD films, nitrogen atoms allow to form different type of bonds and many defect states that are generated within the band gap. So far it has been believed that the enhancement in the electrical conductivity is due to an increase of sp²-content in the film, which probably leads to an increase in grain boundary width. The nitrogen atoms preferentially incorporated into the (GBs) between UNCD grains and boundaries between UNCD grains and an a-C:H matrix. This causes a shift in the Fermi energy level toward the conduction band [13]. These are specific to UNCD films and quite different from the realization of n-type conduction in diamond and hydrogenated amorphous carbon (a-C:H) thin films. Therefore, it is extremely important to characterize the grain boundaries and particularly the bonding configuration of sp^2 carbon atoms.

In UNCD, the diamond grains and the grain boundaries are built of the same element and the grain boundaries are small and in addition are sandwiched between the crystallites, thus the realization of this task is rather difficult. It is reported that the preferential incorporation of nitrogen into the grain boundaries of N-doped UNCD films would form the larger clustering and disordering of graphite-like sp^2- bonded carbons [14, 15, 16]. However, the influence of other factors such as the formation of other phase and the kind of bonding still requires clarification. The undoped UNCD/a-C:H films have a structure wherein many UNCD grains with diameters of approximately 5 nm are embedded in an a-C:H matrix [17] and the films also have electrically insulating properties. Again, the hydrogen in diamond films is incorporated mainly at the grain boundaries and imperfections of the crystallites and bonded mostly to sp^3

carbon atoms. So, inclusion of hydrogen content is also the main key point to control the grain boundaries in the UNCD structure that changes the UNCD structure to microcrystalline diamond. These grain boundaries could be decreased by increasing the diamond-crystallites size by varying the hydrogen content. The future applications of UNCD films, however, especially in advanced fields where surface functionalization or doping is performed, require the detailed characterization of bonding states on the film surface and on the grain boundaries preferably with easy to use, non-destructive methods.

In this work, the change of crystalline structure, electronic and electrical properties on N-doped UNCD is studied by forming the grain boundaries in the interfacial region through inserting different hydrogen gas flow (sccm) during the deposition of UNCD thin films. The different methods are used for these studies are Raman spectroscopy, X-ray photoelectron spectroscopy (XPS), ultraviolet photoemission spectroscopy (UPS) and more advanced techniques such as X-ray absorption near edge structure (XANES) spectroscopy. In addition, X-ray diffraction spectroscopy (XRD), scanning electron microscopy (SEM), Fourier transform infrared spectroscopy (FTIR) etc. methods are also used for the study of UNCD thin films.

4.1 Thin film preparation

The UNCD films were deposited on n-type mirror polished Silicon (100) substrates using microwave plasma enhanced chemical vapor deposition (PECVD) apparatus [18]. The plasma was excited by 1200W microwave (2.45 GHz) in 100 Torr chamber pressure. Total flow rate of the gas was $N_2/Ar = 5\%$ (constant) and H_2 incorporations were varied within the range 0–20 sccm (see table 1). One side polished single crystal (100) Si wafers were used as substrates for UNCD film deposition. Smooth UNCD films were deposited on the substrate in a commercial 5 kW microwave plasma chemical vapor deposition (MPCVD) apparatus using $(N_2/Ar)/H_2/CH_4$ gas mixture.

Table 4.1: Elemental composition and quantification of UNCD synthesized at different hydrogen flow rate (sccm) with constant N_2/Ar flow = 5 sccm.

Samples identification	N_2/Ar (sccm)	H_2 (sccm)	E_0 (V/mm)	C at. %	C mass%	O at. %	O mass%	N at %	N Mass%
5(a)	5.0	0.0	09.3	90.02	87.19	09.61	12.40	0.37	0.41
5(b)	5.0	3.5	11.4	95.67	94.39	3.83	5.04	0.50	0.57
5(c)	5.0	5.0	13.6	96.35	95.41	2.32	3.06	1.32	1.53
5(d)	5.0	8.0	11.2	95.34	94.03	3.73	4.90	0.92	1.06
5(e)	5.0	10.0	15.0	96.40	95.33	3.12	4.11	0.48	0.55
5(f)	5.0	20.0	21.3	95.35	93.99	4.08	5.36	0.57	0.65

Prior to UNCD deposition, Si substrates were thoroughly degreased by sonicating in acetone and methanol, each for 10 min. Afterwards they were subjected to 2 min surface etch in a 40% HF solution to remove the native oxide layer. Then the substrates were ultrasonically abraded for 30 min in a suspension of nanocrystalline diamond powders with a grain size of 5 nm in ethanol to achieve a high nucleation density. Subsequently the substrates were again ultrasonically cleaned in de-ionized water to remove the nanocrystalline diamond particles sticking to the surface and were dried in nitrogen blow before inserted into the reactor chamber. The plasma was induced with a microwave power of 1 kW at a total pressure of 88 torr and total gas flow rate of 100 ml/min.

The substrate temperature was measured by an optical pyrometer through a quartz bell jar and maintained at 700ºC. The growth durations for all UNCD films were 5 h. To investigate the effect of H_2 concentration on the microstructure, grain size and surface smoothness of UNCD

films, the H_2 concentration in the plasma was varied from 0 – 20 sccm, %, N_2/Ar remains constant *i.e.* 5% and rest is methane. The deposition parameters used in the present investigation are listed in Table 1.

4. 2 Thin film characterizations

Systematic study of the electronic and bonding structure of N-doped UNCD thin films functionalized with H_2 and how the mechanical, electrical, electronic and micro-structural properties are varied when different form of grain boundaries are formed in the interfacial region of the sp^2, sp^3, hydrocarbon, and amorphous carbon (a-C) phases. The XRD, SEM, FTIR, Raman, UPS, XANES, I-V characteristic curve are used for these studies. C *K*-edge XANES spectra were measured using the HSGM beam line at the Taiwan Light Source (TLS), Hsinchu, Taiwan. Raman measurements were carried out using 532 nm LASER excitation wavelengths, with the laser beam spot size ~1 μm and the incident power was ~1mW for blue excitation and ~5mW for NIR excitation. The chemical compositional and quantificational analysis was investigated by the XPS measurements and the nano-mechanical characterizations of UNCD films were measured using a Nano indenter. Zeiss Cross Beam 540 Focussed Ion Beam Scanning Electron Microscopy Imaging (FIBSEM) set at 2 kV and 4 mm working distance in high resolution mode was used for the SEM measurements and Shimadzu IR Tracer-100 spectrometer for FTIR measurements.

4.3 Results and discussion

4.3.1 X-ray diffraction

X-ray diffraction (XRD) measurements were performed, proofing that the film consists of crystalline diamond grains. Figure 4.1 shows, the XRD of spectra of N-doped UNCD thin film

synthesized at different conditions. Different hydrogen flow rate (sccm) present in UNCD films were estimated from XPS spectra and are discussed later with the elemental composition and their quantificational analysis tabulated in Table 1. The XRD measurement was done using a standard Bragg-Brentano geometry and a Cu Kα X-ray source.

Different diamond peaks at 2θ = 43.9∘ <111>, 75.2∘ <220>, are clearly detectable. The ⟨100⟩ orientated silicon substrate leads to a peak at 69° and additionally some small peaks on the left side of the silicon <400> peak are detected, caused by the not perfectly monochromatic X-ray source. Each XRD spectrum of UNCD shows relatively sharp and narrow diffraction peaks at 2θ of ~43.9° and ~75.2° that are ascribed to the diffraction of <111> and <220> crystallographic planes of the cubic diamond respectively [19, 20]. Apart from these two diamond peaks, two shoulders observed at ~24.4° and ~37.7° respectively are assigned to (002) and (004) sp^2-diamond peaks. The (111) and (220) peaks at ~43.9° and ~75.2° are diamond peaks. The (111) diamond peak is slightly broader indicating non-crystalline structure of these films. The average crystallite size of the UNCD was estimated to be ranging from ~5 to ~7 nm from the line widths using the well-known Scherrer formula, $d = 0.9\lambda / (B \times cos\theta)$; with the x-ray wavelength (λ) of 0.154 nm. The average grain size is in the range of 4 to 6 nm, as measured by XRD. The full width at half maximum of the <111> peak was fitted, and the grain size was determined by applying Scherrer's equation.
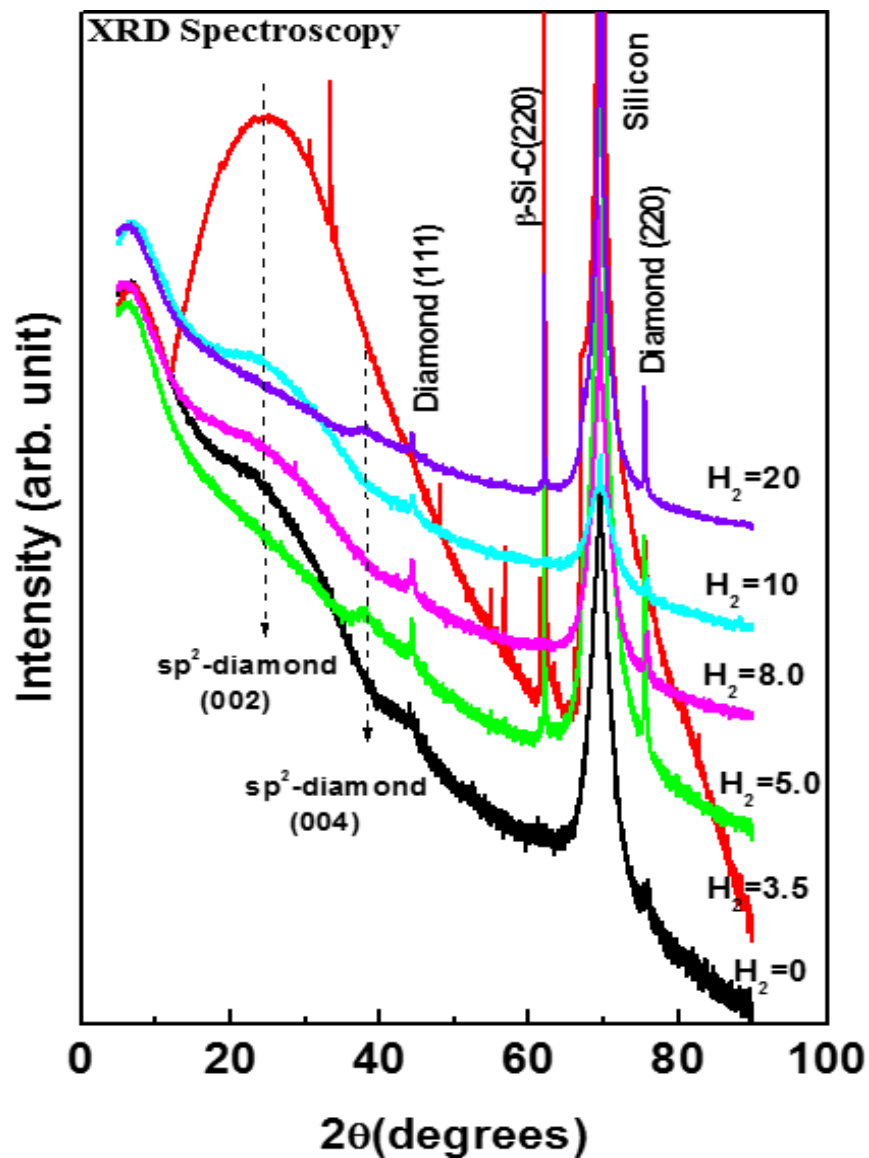
Figure 4.1: *X-ray diffraction pattern of UNCD thin films synthesized at different hydrogen flow rate (sccm) with constant N_2/Ar flow rate = 5 sccm.*

4.3.2 Scanning electron microscopy

The surface morphology of the deposited N-doped UNCD films is shown in figure 4.2 (i-vi) the films were deposited in different hydrogen flow rate starting from 0-20 sccm. A Surface morphology of the films shows densely packed homogeneously needle-like clusters distributed UNCD grains looking like diamond nanowires [19]. The grain size increases with H_2 concentration, and the grain size is around 6 nm when H_2 concentration is below 10%. Even

around 20%, the grain size is still under 10 nm. A slight variation of the grain size with hydrogen flow is 3.5 sccm, is observed with the size being 6 nm. It is also observed that the UNCD needle-like clusters are similar for the films having lower hydrogen flow concentration (5 sccm and 8 sccm) but become more agglomerated at higher H_2-flow rate.

It could be seen that for the UNCD surface smoothness improves and the grain size becomes fine when hydrogen flow rates are 5 sccm and 8 sccm. It is well known that UNCD films can be deposited without hydrogen or with a low concentration of hydrogen [20-22] and that the introduction of hydrogen is beneficial for stabilizing the sp^3 hybrid structure to form the micro-meter/nano-meter polycrystalline diamond films. Some researchers have recently reported the effect of hydrogen on quality of UNCD films with a hydrogen concentration below 3.5 sccm [21,22]. It is interesting to know the effect of hydrogen content on the diamond grain size and nucleation density, and particularly if UNCD can be deposited with hydrogen concentration well above 3.5 sccm as we studied in the present work.
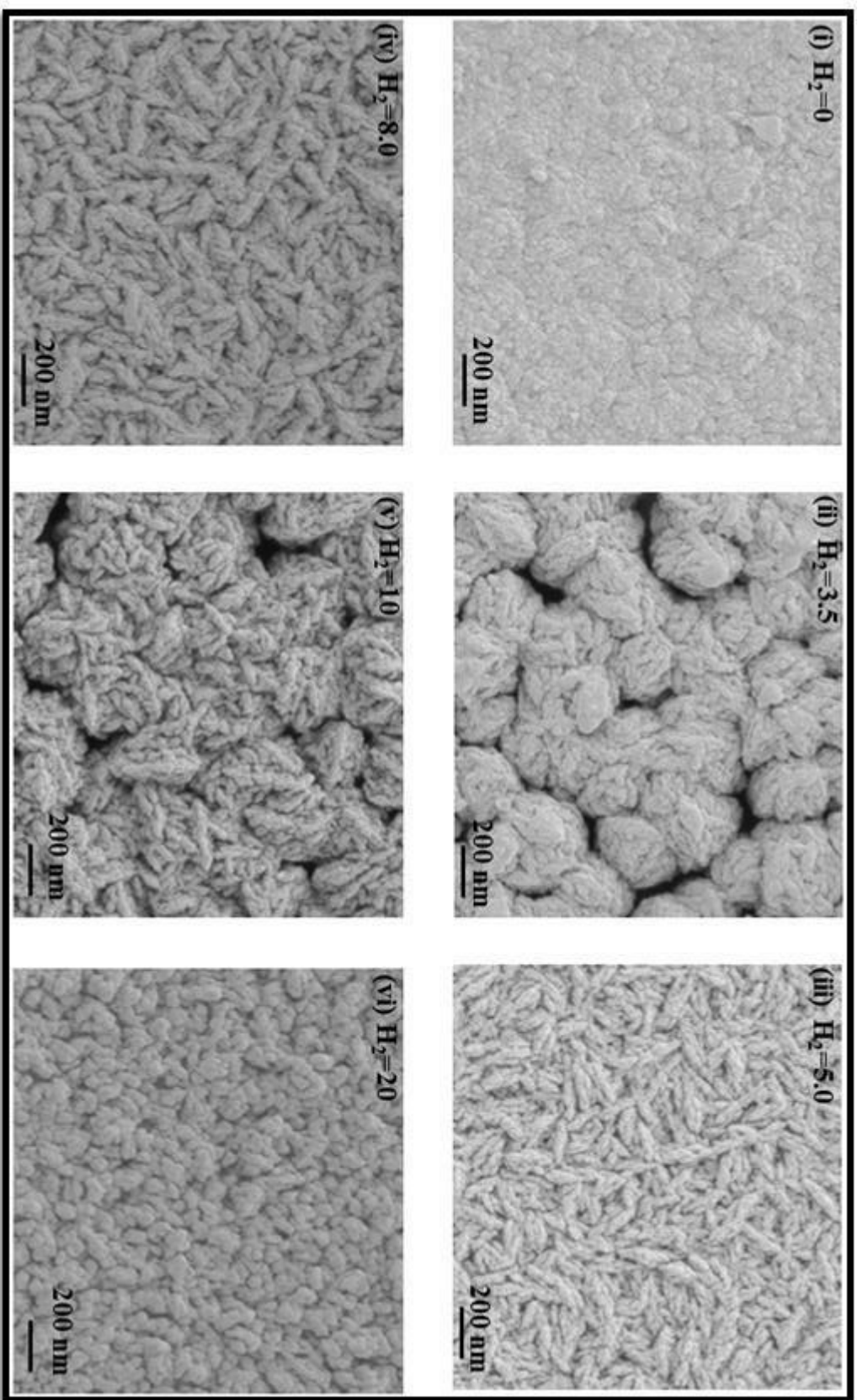
Figure 4.2: *Scanning Electron Microscopy Images of UNCD thin films synthesized at different hydrogen flow rate (sccm) with constant N_2/Ar flow = 5 sccm.*

4.3.3 Fourier transform infrared (FTIR) spectroscopy

Fourier transform infrared (FTIR) spectroscopy is an analytical tool for the study of chemical species, such as oxygen and hydrogen atoms, which are chemisorbed on the diamond surface, basically during the growth process. Fig. 4.3 show different FTIR spectra of N-doped UNCD films deposited at different hydrogen flow rate (sccm). The as-deposited N-doped UNCD film shows a band at 1779 cm^{-1}, which corresponds to species containing C=O groups as well as several bands in the region 1363–1017 cm^{-1}, usually assigned to the C–O–C stretching vibration, suggesting that the as-deposited diamond film was oxidized during the growth process. The broad band at 2900–3600 cm^{-1} and the weak peak at 1640 cm^{-1} is due to physically absorbed molecular water, indicating that a portion of the O_2 atoms react with H_2 to form H_2O. The existence of oxygen came from the reaction of the diamond surface with the air and with the chemicals, during the growth process. Therefore, the appearance of oxygen signals did come from two contributors, the N-doped UNCD crystallite surfaces and the UNCDs grain boundaries. However, due to the UNCD crystallites contain all of the sp^3-hybridized carbon atoms and both of the sp^3-hybridized and sp^2-hybridized carbon atoms are in the spectral range 2800–3100 cm^{-1}, which arise from C–H stretch vibrations, suggesting an hydrogenation process on diamond film surfaces, which was achieved during the synthesis. The C–H vibrational frequencies could be assigned according to the type of carbon hybridization (sp^3, sp^2 or sp^1) and to the type of group (C–H_3, C–H_2 or C–H). The C–H stretch frequency depends only weakly on the arrangement of the more distant neighbours, suggesting that hydrogen was incorporated basically on non-crystalline or defective and/or grain boundaries regions of the films. The broad band detected in the region 3000–3700 cm^{-1} which is due to O–H stretching vibrations of water, suggesting that the UNCD surface adsorb atmospheric water during the treatment [23].

Figure 4.3 *Fourier Transform Infra-Red spectra of UNCD thin films synthesized at different hydrogen flow rate (sccm) with constant N_2/Ar flow = 5 sccm.*

Figure 4.3 shows FTIR spectra in the region of the C–H stretching vibrations two peaks at 2920 cm^{-1} and 2850 cm^{-1} is clearly discernible which can be assigned to CH_2 groups in which the carbon is sp^3 hybridized [24]. Such band has been observed not only in UNCD films [25, 26] but also for in case of amorphous carbon films. Figure of infrared absorption spectra in the region of the C–H stretching vibrations from 3050 cm^{-1} to 2750 cm^{-1}. A network of CH_3, CH_2 and CH groups with varying bond lengths and angles [24]. The peaks above 3000 cm^{-1} further be concluded that the hydrogen is almost exclusively bonded to sp^3 hybridized carbon. The Fig. 4.3 shows the C–H band between 3050 cm^{-1} and 2750 cm^{-1}. The increase of H incorporation in the initial growth phase, the hydrogen is bonded especially in the form of sp^3 CH_2 groups. The distinctive differences between N-doped UNCD films at the centre are in the

spectral range of 2800‑3100 cm^{-1}. The sp^2-CH_2 asymmetric and sp^2-CH stretching vibrations at 3078 cm^{-1} and 3039 cm^{-1} are observed in N-doped UNCD films [24-30]. The sp^3-CH and sp^3-CH^2 asymmetric stretching vibrations at 2895 cm^{-1} and 2923 cm^{-1} are shown for undoped UNCD films [27-30].

4.3.4 Raman Spectroscopy

Raman spectra were measured for all films that were grown with different hydrogen flow rate (sccm) at the excitation wavelength was ~515 nm. The spectra and the deconvoluted spectra are shown in Figure 4.4 and 4.5. A linear background was subtracted from all spectra. The diamond peak at 1332 cm^{-1} is observed in all UNCD films [31, 32]. The D- and G-band peaks were fitted using Gaussian line functions, revealing the intensities and full width at half maximum (FWHM) of each. Following argumentation in [32–34], the increasing FWHM of the G-band and the decreasing ratio of D-band intensity to G-band intensity I_D/I_G indicates an increase of structural disorder of the sp^2 bonded carbon. The chemical constitution and structure of the grain boundaries are reflected by measurements. Peaks assigned as ~1190 cm^{-1} originate from C–H bending and C–C stretching Raman modes of trans-polyacetylene (t-PA or poly-CHx) chains [35, 36]. The t-PA is an alternate chain of sp^2 C–C carbon atoms with a single hydrogen atom bonded to each carbon atom and this lies in the grain boundaries of UNCD crystallites [37]. Furthermore, the peaks assigned as 1550 cm^{-1} bands correspond to sp^2 C–C bonded carbon.

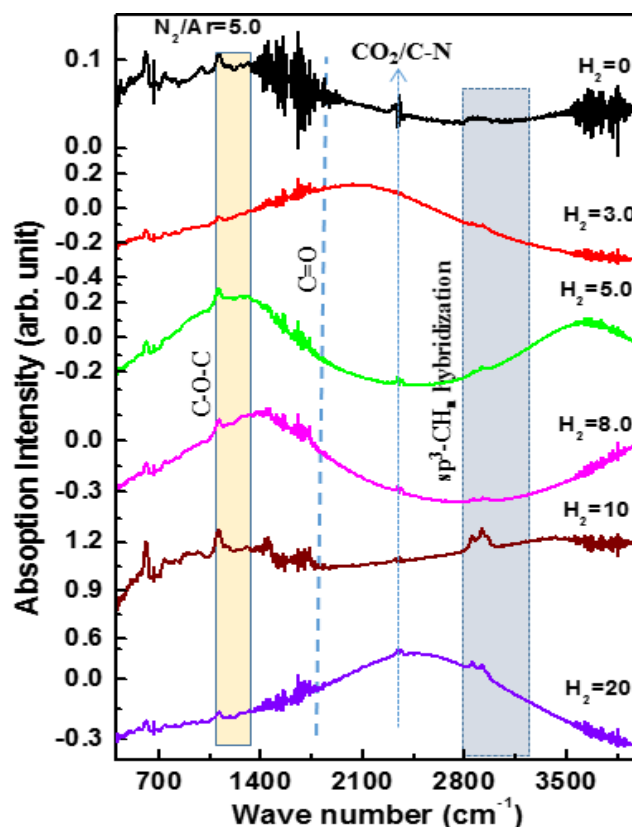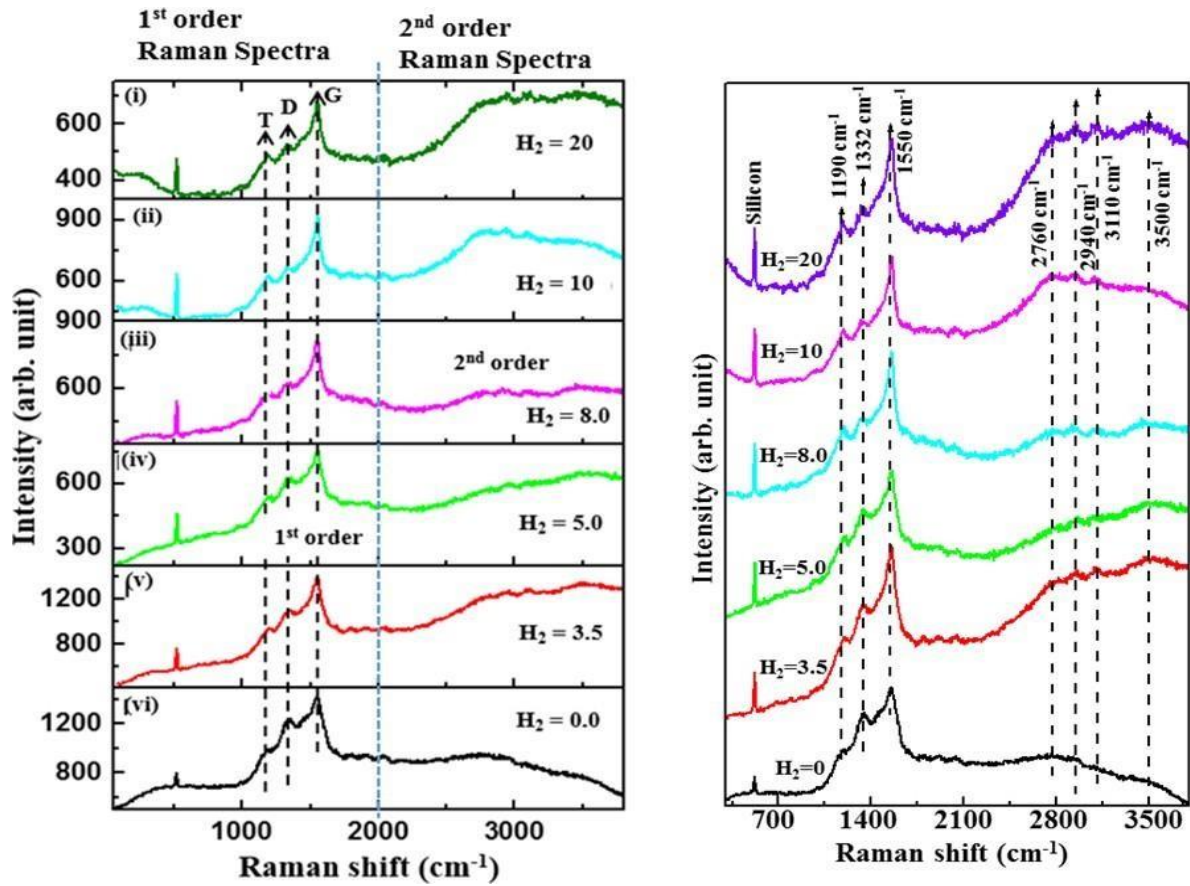***Figure 4.4****: Raman spectra of UNCD thin films synthesized at different hydrogen flow rate (sccm) with constant N_2/Ar flow = 5 sccm*

We conclude that, for higher amount of H_2 addition to the feed gas, the disorder of the grain boundaries increases. This relation between disorder of grain boundary and conductivity agrees with investigations on plasma CVD grown nitrogen doped UNCD films [37] and will be discussed later in the electrical measurement section. The G band is of E_{2g} symmetry and appears due to bond-stretching vibration of a pair of sp^2C–C sites in the form of olefinic chains or aromatic rings [35, 36, 38]. In microcrystalline and single crystal diamonds, the full-width at half-maximum (FWHM) of this peak is normally narrow and centred at ∼1333 cm−1. The shift of this peak to the lower wavenumber (1332 cm⁻) and the subsequent broadening in the case of the UNCD film correspond to the strained lattice due to nanocrystalline grains. We

have deconvoluted all spectra that are shown in Fig. 4.5, where 1st column shows the first order and 2nd column shows second-order Raman spectra. Different parameters obtained after gaussian fitting fist order and second order are tabulated in table 2 (a) and table 2(b).
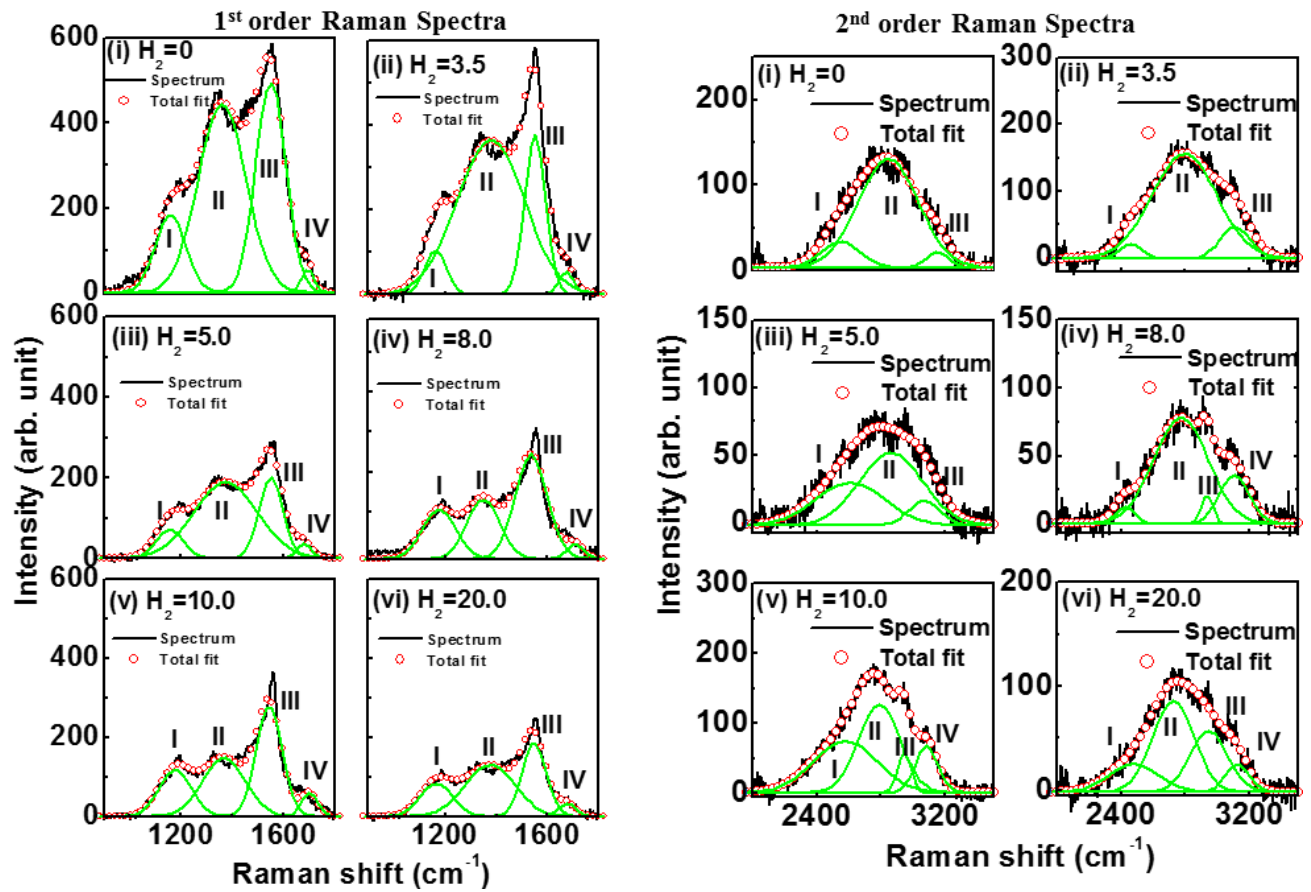
Figure 4.5: *Convoluted different 1st order (2nd order) Raman spectra of UNCD thin films synthesized at different N_2/Ar-flow rate =5 sccm.*

Table 2 (a): Different Raman parameters obtained from convoluted Raman spectra of UNCD synthesized at different hydrogen flow rate (sccm) with constant N_2/Ar flow = 5 sccm.

H_2	Peak I (T-Peak)				Peak II (D-peak)				Peak III (G-Peak)				Peak IV		
	Position x1 (cm⁻¹)	Width Δw1 (cm⁻¹)	Area a1(a.u.) Intensity	Height h1(a.u.) Intensity	Position x2 (cm⁻¹)	Width Δw2 (cm⁻¹)	Area a2(a.u.) Intensity	Height h2(a.u.) Intensity	Position x3 (cm⁻¹)	Width Δw3 (cm⁻¹)	Area a3(a.u.) Intensity	Height h3(a.u.) Intensity	Position x4 (cm⁻¹)	Width Δw4 (cm⁻¹)	Area a4(a.u.) Intensity	Height h4(a.u.) Intensity
0.0	1157.3	119.95	27332	181.8	1358.6	186.03	103830	445.3	1548.7	117.46	72875	495.0	1692.6	48.73	3403	55.7
3.5	1163.1	83.96	11146	105.9	1377.5	264.08	121070	365.8	1550.8	83.69	39983	381.2	1672.6	57.54	3946	54.7
5.0	1153.6	105.18	9357	71.0	1373.2	249.24	59473	190.4	1551.4	92.40	23187	200.2	1678.8	57.06	2567	35.9
8.0	1177.1	130.07	19978	122.6	1348.5	127.59	23810	148.9	1535.7	128.75	42127	261.1	1708.8	66.81	3156	37.7
10.0	1175.1	125.99	18644	118.1	1366.1	168.56	31551	149.3	1544.0	100.14	35150	280.1	1700.5	62.75	4679	59.5
20.0	1165.9	126.49	13254	83.6	1373.8	194.72	31767	130.2	1546.9	95.74	22731	189.4	1677.1	68.74	2766	32.1

Table 2 (b). Different Raman parameters obtained from convoluted 2nd order Raman spectra of UNCD thin films synthesized at different H_2 flow rate (sccm) with constant N_2/Ar-flow rate=10 sccm

H₂	Peak I (T-Peak)				Peak II (2D-peak)				Peak III (2G-Peak)				Peak IV			
	Position x1 (cm⁻¹)	Width Δw1 (cm⁻¹)	Area a1 (a.u.) Intensity	Height h1 (a.u.) Intensity	Position x2 (cm⁻¹)	Width Δw2 (cm⁻¹)	Area a2 (a.u.) Intensity	Height h2 (a.u.) Intensity	Position x3 (cm⁻¹)	Width Δw3 (cm⁻¹)	Area a3 (a.u.) Intensity	Height h3 (a.u.) Intensity	Position x4 (cm⁻¹)	Width Δw4 (cm⁻¹)	Area a4 (a.u.) Intensity	Height h4 (a.u.) Intensity
0.0	--	--	--	--	2546.4	347.71	11362	26.073	3170.1	137.78	1903.2	11.021	2909.4	405.53	29811	58.654
3.5	2479.4	441.93	4652.8	8.4	2750.2	368.27	15031	32.565	3013.5	236.60	6653.7	22.438	--	--	--	--
5.0	2521.0	239.05	16923	56.484	2858.7	380.34	73350	153.88	3151.8	193.24	11091	45.793	--	--	--	--
8.0	2416.2	55.625	1336.9	19.176	2779.3	451.66	56779	100.30	3080.5	168.19	4130.5	19.594	--	--	--	--
10.0	2523.7	235.96	26418	89.330	2733.5	370.45	282220	607.85	3093.9	221.43	58391	210.40	--	--	--	--
20.0	2371.7	530.13	3032.4	4.5641	2776.2	439.34	7809.5	14.183	3154.8	243.95	2073.7	6.7823	--	--	--	--

The D band is of A_{1g} symmetry and belongs to breathing mode of a six-fold aromatic ring, which is activated by disorder present in the sp^2 C–C bonding state [35, 37]. The broad spectrum exhibited at 1325 cm^{-1} is denoted as the D* band, which belongs to the T_{2g} symmetry of the nano-diamond phase [36]. However, the intensity, peak position and shape of the peaks as given in table 2 are different from those of the virgin UNCD surface. Most importantly, the intensity of the v2 band weakens in the wear track. Furthermore, all the peaks related to t-PA shift to the lower wavenumber, which is attributed to the bond length disorder [38, 39] arising due to mechanical sliding. Moreover, in the wear track, the D band is shifted to the lower wavenumber as compared with the virgin UNCD film. This shift is associated with the ordering of six-fold aromatic rings in sp^2 C–C bonding [39]. Most importantly, the nano-diamond peak denoted as the D* band is shifted to a lower wavenumber at 1334 cm^{-1} during the tribology test, which explains relaxation of strain due to mechanical sliding. Ordering of six-fold aromatic ring in sp^2C–C bonding and shift of the nano-diamond D* band to a lower wavenumber are relative quantities [38]. However, the G band peak position more/less matches with each other in all the spectra, which confirm similar vibrational bond stretching between a pair of sp^2C–C sites.

4.3.5 Mechanical properties of Ultra-Nano-Crystalline diamond (UNCD) Thin films

Diamond is the hardest of all known single-phase materials, with hardness values around 100 GPa, depending on the crystalline direction. The hardness values reported for polycrystalline diamond (PCD) films are in the range of 80 – 100 GPa, *i.e.* rather close to the single crystalline values. The same is true even for nanocrystalline (NCD) and ultra-nanocrystalline diamond (UNCD) films, for which harnesses up to 95 GPa have been reported. On the other hand, there is a considerable spread of hardness values for this type of films, but systematic studies on the influence of important deposition parameters.

Fig. 4.6 Young's modulus of UNCD thin films synthesized at constant N_2/Ar-flow rate = 5 sccm with different H_2-flow rate (a) H_2 = 0; (b) H_2 = 3.5; (c) H_2 = 5.0; (d) H_2 = 8.0; (e) H_2 = 10.0; (f) H_2 = 20.0.
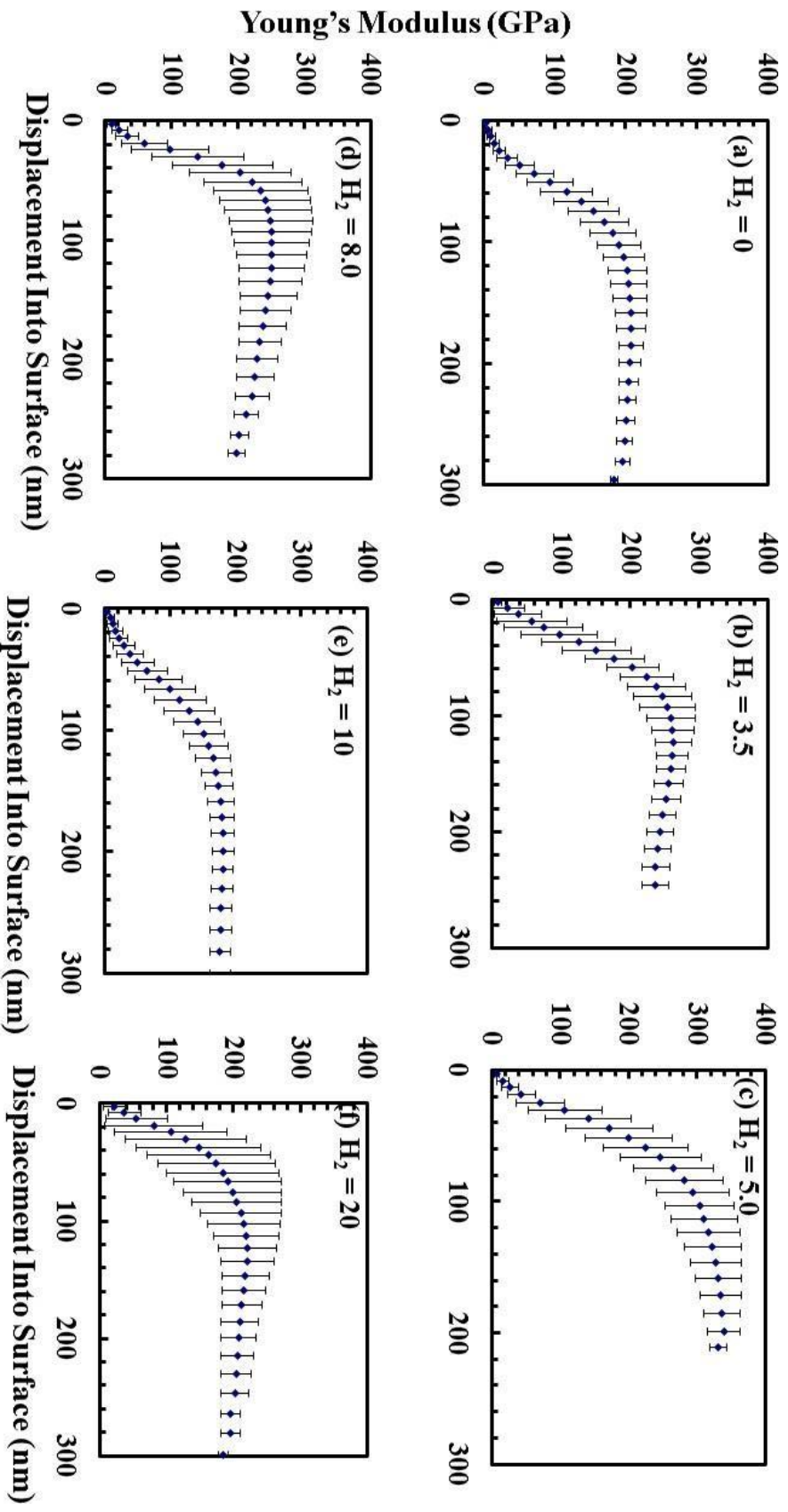
Fig. 4.7 Hardness of UNCD thin films synthesized at constant N_2/Ar-flow rate = 5 sccm with different H_2-flow rate (a) $H_2 = 0$; (b) $H_2 = 3.5$; (c) $H_2 = 5.0$; (d) $H_2 = 8.0$; (e) $H_2 = 10.0$; (f) $H_2 = 20.0$.
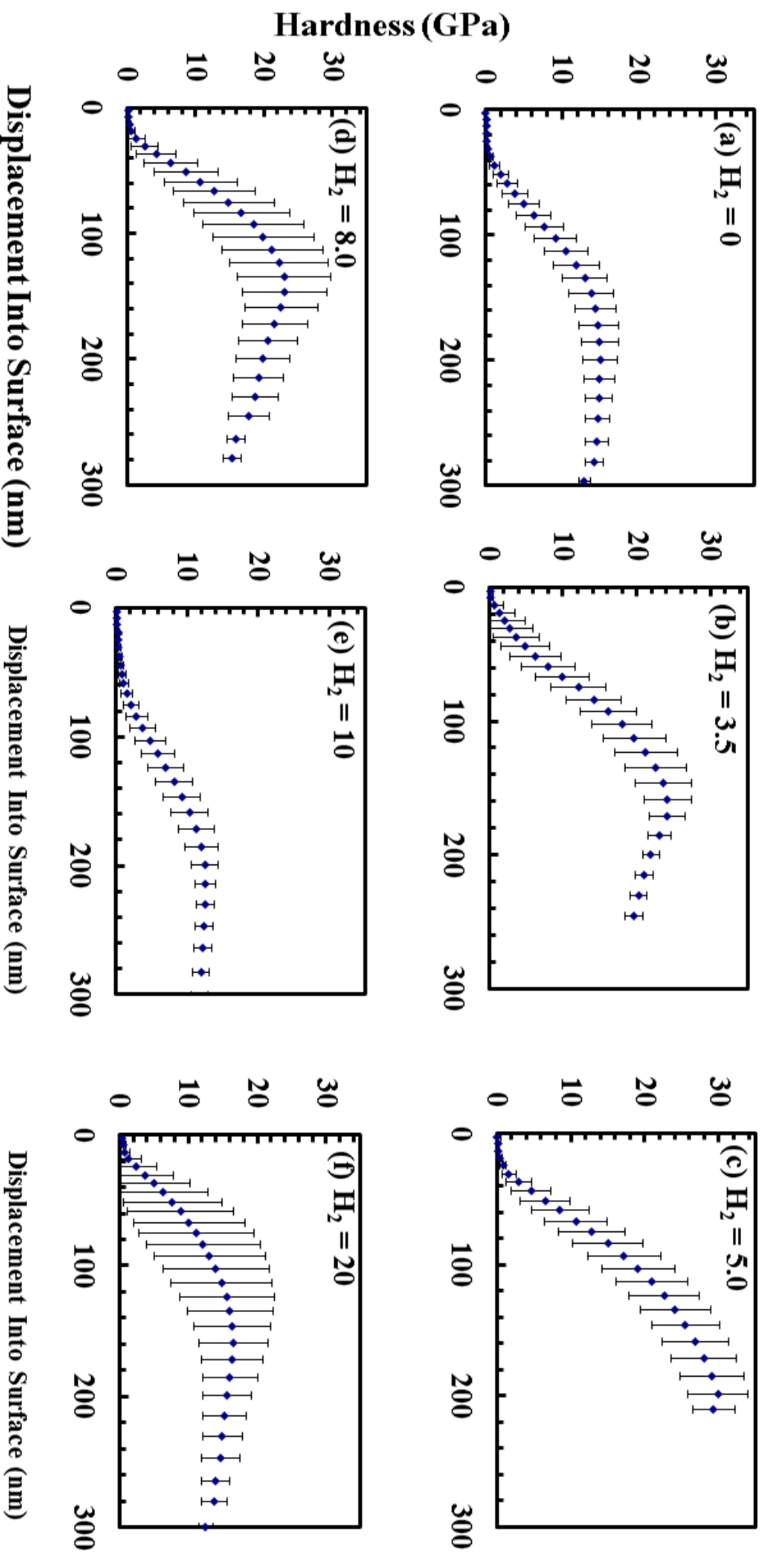
66

As we know that the UNCD films are a candidate for applications in tribology and biomedicine, it is important to know how the hardness, but also other tribological properties are changes. The Mechanical properties, Young's modulus, hardness, and load as a function of displacement are shown in Fig. 4.6 and Fig. 4., respectively. It must be noted that the penetration depth was maintained at 30 mN (approximatively 90 nm of penetration) to minimize the influence of the substrate. Three different points were tested for each UNCD with the same pressed depth. The residual pressed depths for sample with N_2-content ~0.48 at% is lower than those of UNCDs having higher content of N_2. This implies that the elastic recovery ability has improved for the films with higher N_2-content, 1.32 at%, 0.92 at% and have better elastic recovery ability. A change in modulus and hardness with pressed depth for UNCDs is shown in figures 4.6 and 4.7. The Young's modulus is found to be in 160 – 300 GPa range, while the hardness at the range of 14 – 30 GPa. These ranges are comparable with those reported before [40, 41]. On a first view, the Hardness and the Young's modulus found for our UNCD films seem to decrease with a decrease with N_2 (at%) concentrations. These results can be explained in terms of amorphous carbon matrix located in the grain boundary regions of the UNCD films.

4.3.6 X-ray photoemission spectroscopy (XPS)

The elemental analysis, quantification, and chemical bonding of all N-doped UNCD films were performed using X-ray photoelectron spectroscopy (XPS) and was performed using nonmonochromatic Al Kα radiation with a photon energy of 1486.6 eV on a KRATOS spectrometer. The measurement was conducted without ion sputtering etching, to avoid reconfiguration of the bonds. The diameter of the x-ray probe during the measurement was 250 μm. For analysis of UNCD materials, we have measured C 1s, O 1s and N 1s XPS binding energies spectra as shown in figure 4.8 and 4.9. To analyze the XPS spectra precisely, C 1s spectra were decomposed into the following four peaks: sp^2-bonded carbon (C=C), sp^3-

bonded carbon (C–C), carbon-oxygen single bonds (C–O/C–O–C), and carbon-oxygen double bonds (C=O/COOH) [42,43]. The C–O/C–O–C peaks should be ascribed to the adsorption of oxygen on the film surface during and after films deposition [44, 45]. The C=O/COOH peak is observed in the spectra measured by XPS. The C=O/COOH peaks in their spectra, which means the adsorption of oxygen is suppressed, owing to their preservation in the portable vacuum box.

The XPS measurements show sharp spectra with very weak shoulder of the C–O/C–O–C peak due to investigation at deep depth in the films. However, the argon ion bombardment is essential for cleaning the films surface prior to X-ray photoemission spectroscopic measurements, to reduce the contribution of film surface contaminants. The XPS method makes possible the structural examination of the UNCD thin films without applying any surface pre-treatment, such as argon ion bombardment, which destroys nano-sized diamond crystallite in the films [45]. The sp^3 peaks show a relative decrease as the hydrogen gas flow is changes. The XPS technique produces sharp and intense sp^3 peaks with a noticeable difference compared to the sp^2 peaks, unlike those obtained by XPS. The dependence profile of the sp^3 bonding fraction estimated from XPS are in good agreement, not only with each other but also with the hardness dependence profile. This means that the estimation of the sp^3 fraction is precise since the hardness proportionally increases with the sp^3 fraction. On the other hand, the sp^3 fraction estimated from convoluted XPS spectra. Estimation of the sp^3 bonding fraction is also affected by the existence of C–O/C–O–C and C=O/COOH peaks. Therefore, the XPS method and demonstrating a careful methodology for XPS investigation, are recommended when assessing the sp^3 bonding fraction to UNCD thin films and nanomaterials. The UNCD films C 1s peaks was performed by using Gaussian peaks at binding energies of 284.3 eV and 285.3 eV which are attributed to the sp^2 C=C and sp^3 C–C bond

atoms, respectively. The two peaks at 285.9 and 286.7 eV *correspond* to *sp²*-hybridization bonding structures of C atoms bonded to N atoms (sp² C=N) and *sp³* -hybridization bonding structures of C atoms bonded to N atoms (*sp³* C–N), respectively and their relative intensities are tabulated in Table 3. The de-convoluted core level C 1*s* XPS spectra of the samples are shown in Fig. 4.9. The UNCD films, *sp³* C–C bonding is predominant with a peak intensity *sp²* C=C intensity. The appearance of the two peaks sp² C=N and *sp³* C–N indicates the formation of a chemical bond between C and N atoms after the incorporation of nitrogen. The C 1*s* spectra are de-convoluted in different components and are marked as peak –I, peak –II, peak – III and Peak – IV, respectively.

The peak-I at binding energy ~283.4±0.3 eV and peak –II at ~285.3±0.2 eV corresponds to *sp²* C=C and *sp³* C-C hybridization bonding structures respectively [42]. The other two peaks at ~286.5±0.4 eV and 287.2±0.3 eV correspond to *sp²*-hybridization bonding structures of C atoms bonded to N atoms (*sp²* C=N) / C-O-C bonds and *sp³*-hybridization bonding structures of C atoms bonded to N atoms (*sp³* C–N), respectively and their chemical compounds and binding energy position, relative intensities, peak width are tabulated in Table 3 from the results of the figures 4.9. The two peaks indicate above is the formation of a chemical bond between C and N atoms after the incorporation of nitrogen and this agrees with N 1*s* XPS spectra of UNCD films shown in Fig. 4.9. The peak at 399.8 eV within the range 397.0 – 402.5 eV is the contribution of N-*sp³* C and N-*sp²* C [43, 44] further confirming the formation of chemical bonds between C and N atoms in UNCD structures. Incorporation of nitrogen results in two different N–C bonding state, including N–sp³ C bond and N–sp² C bond.

Figure 4.9 shows the de-convoluted O 1*s* XPS of UNCD films, where two peaks at ~529 eV and 532 eV correspond to O-C/N-O and O=O bonds, respectively [45]. De-convoluted C 1*s*, O 1*s*, and N 1*s* XPS parameters *viz.* peak positions, peak width and peak intensities of

synthesized UNCD films are tabulated in Table 3. These results confirm a proper mixing of nitrogen content with UNCD species with low nitrogen concentration (0.48 – 1.32 at%) being well mixed to form nitrogen doped UNCD. As a result, the carbon-nitrogen bonds with nitrogen not on the surface of UNCD
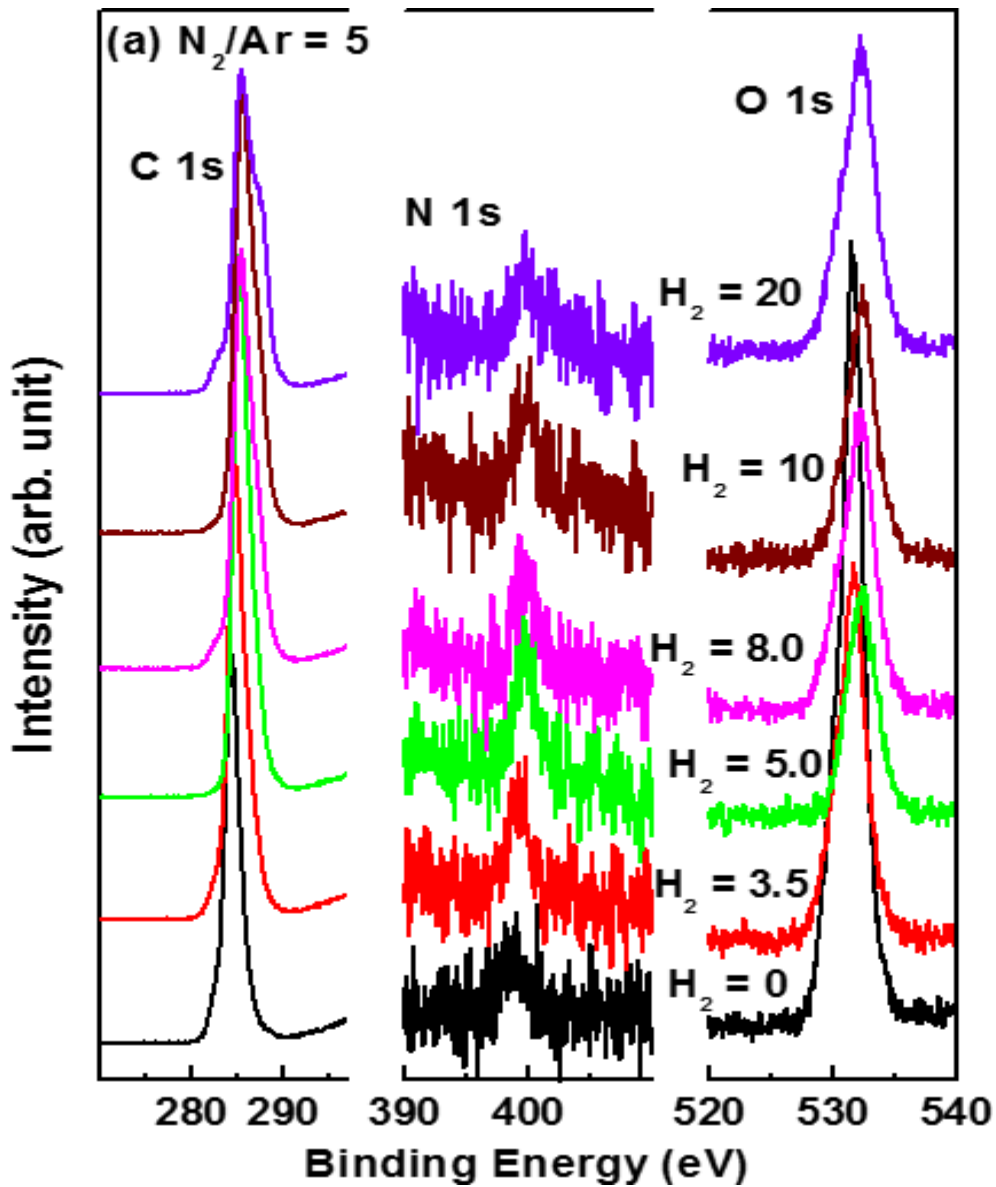

Figure 4.8: X-ray Photoemission Spectroscopy spectra of UNCD thin films synthesized at different hydrogen flow rate (sccm) with constant N_2/Ar flow = 5 sccm.
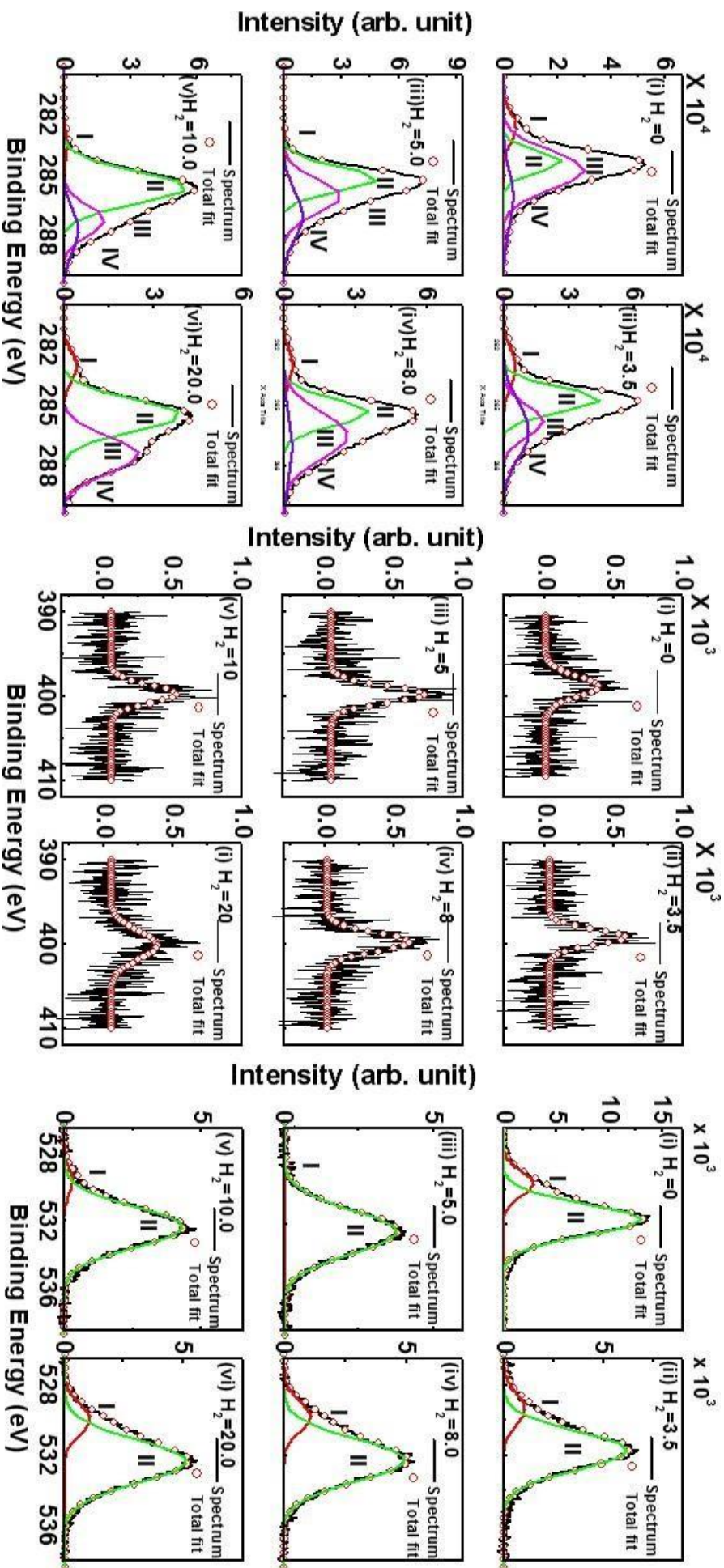
Figure 4.9: *Convoluted C 1s (left panel), N 1s (middle panel) and O 1s (right panel) XPS of UNCD synthesized at different hydrogen flow rate (sccm) with constant N₂/Ar flow = 5 sccm.*

Table 3. Different (a) C 1s, (b) O 1s, (c) N 1s XPS parameters obtained from convoluted C 1s XPS Spectra of UNCD synthesized at different hydrogen flow rate (sccm) with constant N_2/Ar flow = 5 sccm.

C 1s XPS

H_2	Peak I — Position x1 (cm^{-1})	Width $\Delta w1$ (cm^{-1})	Area a1(a.u.)	Intensity Height h1(a.u.)	Peak II — Position x2 (cm^{-1})	Width $\Delta w2$ (cm^{-1})	Area a2(a.u.)	Intensity Height h2(a.u.)	Peak III — Position x3 (cm^{-1})	Width $\Delta w3$ (cm^{-1})	Area a3(a.u.)	Intensity Height h3(a.u.)	Peak IV — Position x4 (cm^{-1})	Width $\Delta w4$ (cm^{-1})	Area a4(a.u.)	Intensity Height h4(a.u.)
0.0	282.6	1.47	9539	5173	284.3	1.02	28417	22134	284.7	1.85	70929	30563	286.2	2.89	14253	3931
3.5	283.1	1.95	14421	5915	284.7	1.22	68367	44881	285.7	1.58	36968	18717	286.2	2.78	42134	12089
5.0	283.4	1.25	2016	1281	285.1	1.19	74053	49737	286.0	1.69	63470	30041	286.9	2.41	31419	10414
8.0	283.1	1.93	9359	3868	285.3	1.33	59812	35952	286.5	2.31	79270	27403	287.0	3.53	16947	3827
10.0	283.7	1.90	4554	1913	285.6	1.57	110350	56102	287.2	1.47	34895	18877	287.7	2.21	18794	6795
20.0	283.02	1.60	9055	4662	285.5	1.58	79670	40092	287.4	1.82	58145	25533	289.9	0.89	1084	967

O 1s XPS

H_2	Peak I — Position x1 (cm^{-1})	Width $\Delta w1$ (cm^{-1})	Area a1(a.u.)	Intensity Height h1(a.u.)	Peak II — Position x2 (cm^{-1})	Width $\Delta w2$ (cm^{-1})	Area a2(a.u.)	Intensity Height h2(a.u.)
0.0	529.6	1.40	5057	2880	531.7	1.78	29408	13154
3.5	529.3	1.85	2546	1096	531.7	2.19	17121	6247
5.0	528.6	1.08	53	39	532.4	2.48	11869	3810
8.0	529.8	1.74	2416	1108	532.3	2.39	14926	4986
10.0	529.7	1.59	635	319	532.4	2.40	12997	4312
20.0	529.9	1.78	2427	1085	532.3	2.45	15785	5147

N 1s XPS

H_2	Peak I — Position x3 (cm^{-1})	Width $\Delta w3$ (cm^{-1})	Area a3(a.u.)	Intensity Height h3(a.u.)	Peak II — Position x4 (cm^{-1})	Width $\Delta w4$ (cm^{-1})	Area a4(a.u.)	Intensity Height h4(a.u.)
0.0	398.8	2.57	1214	377	--	--	--	--
3.5	399.2	1.87	1269	541	--	--	--	--
5.0	399.8	2.02	1696	669	--	--	--	--
8.0	399.8	2.23	1653	590	--	--	--	--
10.0	399.8	2.13	1268	474	--	--	--	--
20.0	400.1	3.83	1422	335	--	--	--	--

4.3.7 Ultra-Violet Photoemission Spectroscopy (UV-PES)

The UV-PES spectra were recorded by operating the spectrometer at a constant retardation ratio. The energy of two photon energies used here are for the He I (hν = 21.22 eV) and He II (hν = 40.81 eV) excitation lines, respectively. We have measured UPS using He-I (hν = 21.22 eV) and He-II (hν = 40.81 eV) excitation energy and the results are shown in Figs. 4.10(a) and Fig. 4.10(b) respectively. Fig 4.10(a) shows the VB-edge (high K.E. slope ≈ converted into binding energy) and secondary electron cut-off (low K.E. slope) of the He-I (~21.22 eV) spectra of N-doped UNCD films. The dominance of these UPS valence band spectra by *p*- electron states is due to abundance of high excitation cross section of these low photon energies [46]. We have also measured UPS as shown in Fig.4.10(a) and the kinetic energy of the electrons at the Fermi edge (E_{Fermi}) and that of the secondary electron cut-off ($E_{cut-off}$) are enlarged at the right shoulder of Fig.4.10(b). To distinguish secondary electron cut-off from the low kinetic energy electron scattering, Negative bias voltages were put on the sample. A shown in Fig. the binding energy E_{Fermi} and the $E_{cut-off}$ are 21.22 and 3.76eV respectively, therefore a work function Φ is estimated by the relation:

$$\Phi = h\nu - (E_{Fermi} - E_{cut-off}) = 21.22 - (21.22 - 3.76) = 3.76 \text{ eV}$$

The surface work function of these UNCD films were derived from secondary electron cut-off low kinetic energy slope as shown in left panel of Fig. 4.10(a). The work function (Φ) of the reference, Ag film, is found to be 4.37 eV, while work functions of UNCD's are listed in table 4. It is found that the values are initially increases from 3.76 eV to 3.94 eV when hydrogen gas flow is 0.0-sccm to 5.0-sccm and after that the values are decreases from 3.83 to 3.62 eV for the UNCD films having hydrogen gas flow changes from 8.0-sccm to 20.0-sccm.
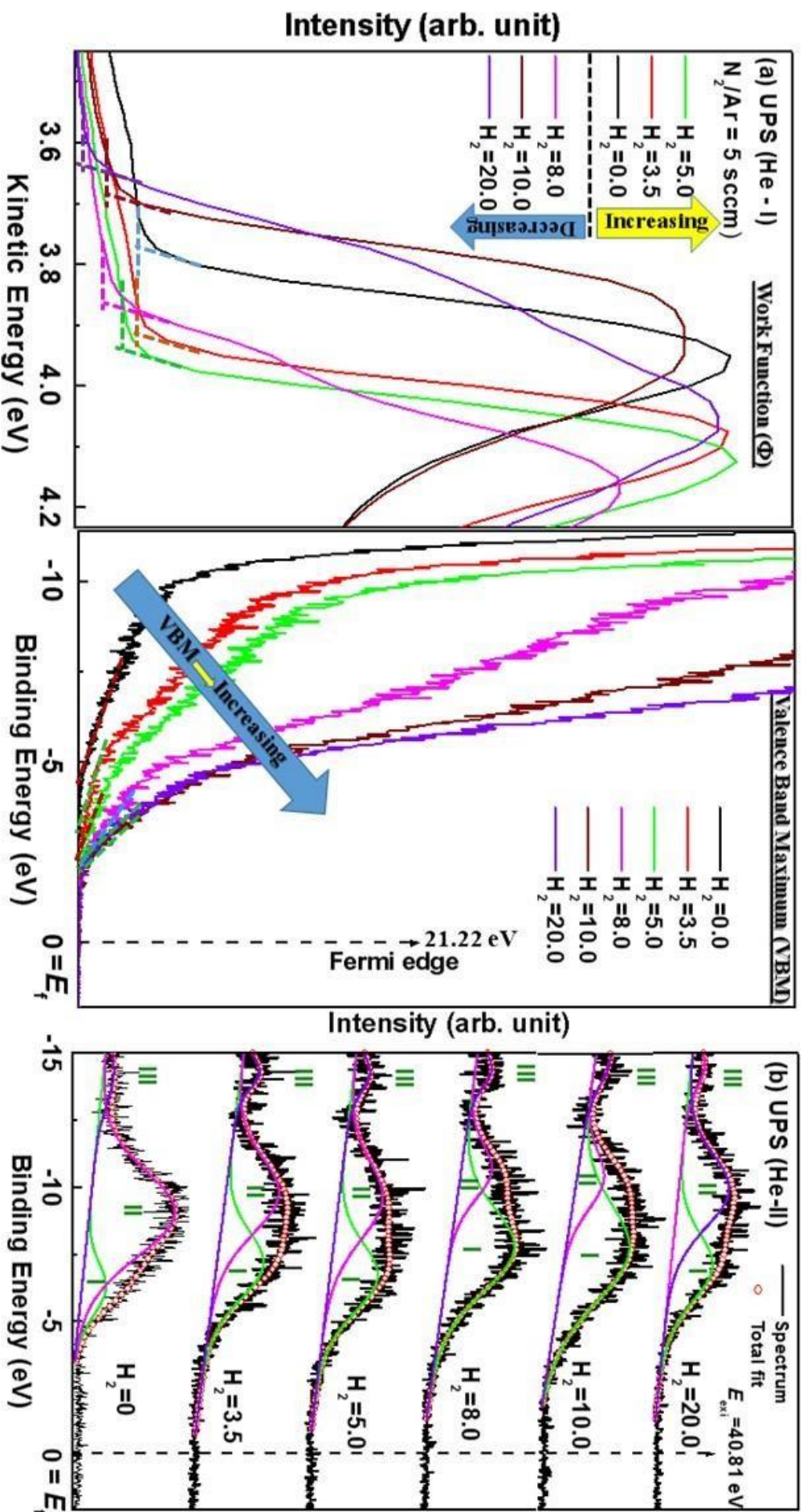
Figure 4.10: *Ultra-violet photoemission spectroscopy; (a) UPS (He-I) and (b) UPS (He-II) Spectra of UNCD synthesized at different hydrogen flow rate (sccm) with constant N₂/Ar flow = 5 sccm.*

Table 4: Different UPS parameters obtained from UPS (He-I) and convoluted UPS (He-II) Spectra of UNCD synthesized at different hydrogen flow rate (sccm) with constant N_2/Ar flow = 5 sccm.

H_2	UPS (He-I), hv = 21.22 eV		UPS (He-II), hv = 40.81 eV								
	Work Function, Φ (eV)	Valence-Band Maximum, (VBM) (eV)	Peak I (p-σ)			Peak II (mixed of s- and p- state)			Peak III (s-state)		
			Position x1 (eV)	Width $\Delta w1$ (eV)	Intensity a1(a.u.)	Position x2 (eV)	Width $\Delta w2$(eV)	Intensity a2(a.u.)	Position x3(eV)	Width $\Delta w3$ (eV)	Intensity a3(a.u.)
0.0	3.76	4.57	6.2	2.40	13.8	9.0	3.9	80.1	14.1	2.4	6.1
3.5	3.91	3.91	7.1	3.08	40.74	9.7	3.44	51.83	14.0	1.40	7.4
5.0	3.94	2.87	6.6	3.15	45.56	9.5	3.55	46.67	14.2	1.60	7.8
8.0	3.83	2.13	7.6	3.73	70.36	10.6	2.49	22.29	14.3	1.52	7.4
10.0	3.66	2.00	7.5	4.38	73.38	10.3	2.62	18.70	14.3	2.01	7.9
20.0	3.62	1.95	7.0	3.12	40.11	9.9	3.34	52.07	14.5	1.89	7.8

The valence band maximum (VBM = E_f - E_{VB}) was estimated using the slope of each VB-edge spectra as shown in right panel of Fig 4.10(a). It is interestingly found that the VBM is gradually decreases from 4.57 eV to 1.95 eV for the UNCD films deposited with 0-sccm to 20- sccm hydrogen gas flow. The work functions and VBM of N-doped UNCD are tabulated in Table 4. The role of N_2/H_2/CH_4 gases in a change in electronic structure was investigated by further analyzing the valence-band spectra obtained by the excitation energy E_{ex} = 40.81 eV. The spectra were decomposed into three Gaussian peaks after the subtraction of Gaussian line, as shown in Fig. 4.10(b). These peaks are described as *p*-σ (6.6 eV – 7.6 eV: peak I), a mixture of *s* and *p* states (9.5 – 10.6 eV: peak II), and *s* (14.3 eV: peak III) bands of carbon, respectively [47]. A similar study was made by Francz *et al.* [31] for CVD-diamonds and they found a peak near ~13 eV and assigned as "diamond" peak. Comparing our spectra, with this peak we may assigned the peak observed at ~14 eV is "diamond peak".

4.3.8 X-ray absorption near edge structure (XANES) spectroscopy

The C *K*-edge XANES spectra were measured using the HSGM beam line at the NSRRC Hsinchu, Taiwan. Figure 4.11 shows the normalized XANES spectra of C *K*-edge UNCD films deposited with different hydrogen (sccm) incorporation. Fig. 4.11 shows the NEXAFS spectra of the films clearly ascertaining that the major part of the carbon is the *sp³* diamond phase with a smaller amount of *sp²* graphitic phase distributed in the films. The small peak at ~285 eV [48-51] is assigned to the C (1*s*) – π* transition corresponding to the sp² graphitic phase. A sharp peak at ~289 eV corresponds to the diamond electron core excitation of C–C (1s)–σ*, i.e., the *sp³* diamond phase. A weak dip observed at ~302 eV [52-54] is assigned to the second absorption band gap of the diamond. The magnified image of the peak at ~285 eV shown inset figure 4.11.
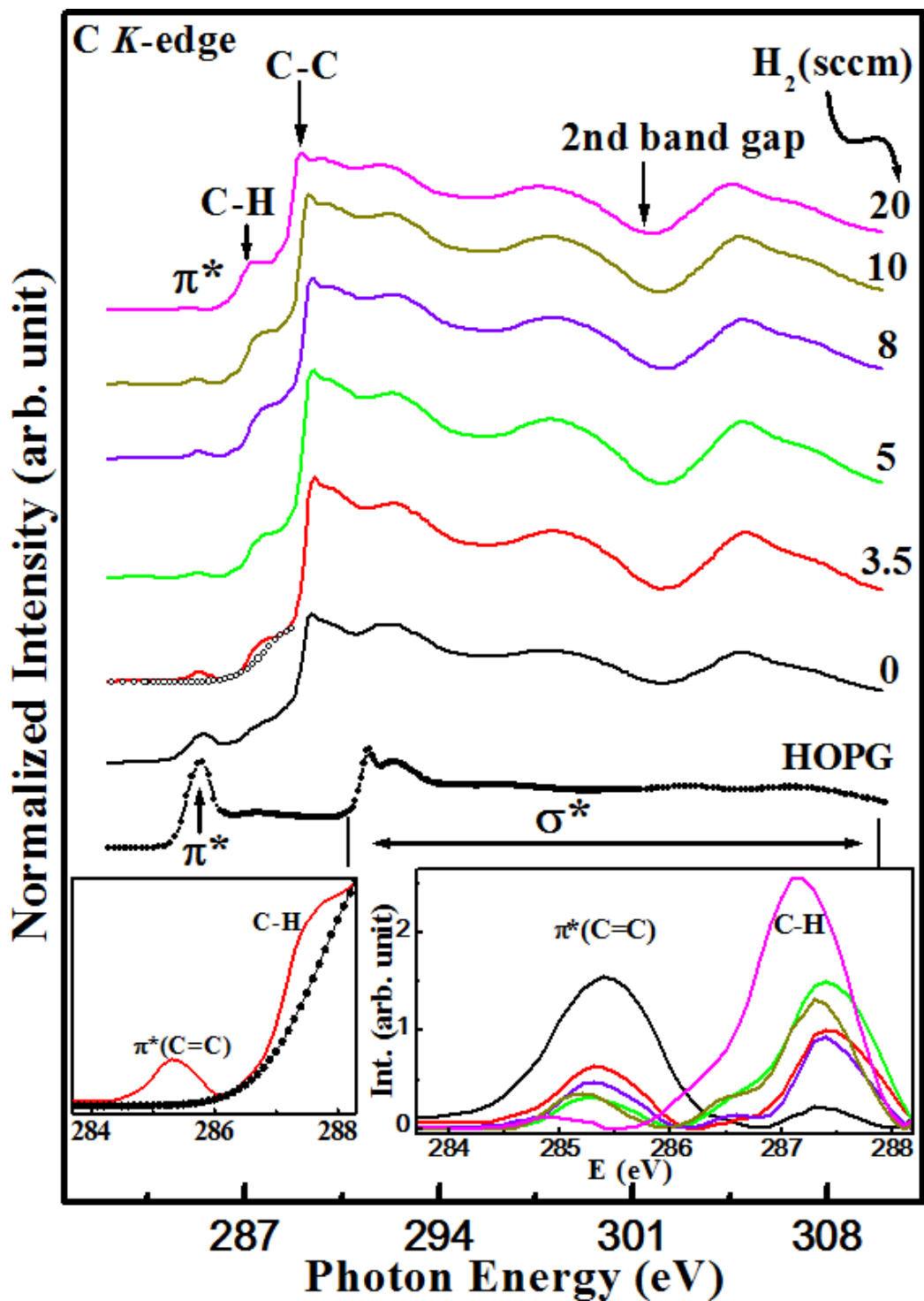
Figure 4.11: *X-ray absorption near edge structure spectroscopy (XANES) of UNCD thin films synthesized at different hydrogen flow rate (sccm) with constant N₂/Ar flow = 5 sccm.*

In these spectrums, the peak π*-band marked in the figure is related with graphitic structure (C=C) and a shoulder described as C–H bonds are observed at~285.5 and ~287.5 eV,

respectively [55]. The intensity of the $\pi*$-band gradually decreases, whereas C–H bonds gradually increase with increase of hydrogen incorporation in the UNCD film structure in all XANES spectra. A sharp peak at ~290eV is C 1s $\sigma*$ (C–C) transitions, which is the characteristic of diamond core-exciton [55, 56] and a dip at 302.1 eV attributed to the second absolute band gap for the diamond materials [55, 56]. This clearly illustrates that most of the films retain ansp3-bonding nature, regardless of hydrogen incorporation. Moreover, the peak present at 285.3 eV associated with the C1s $\pi*$ transition (C=C) indicates that the films contain a small proportion of graphitic phase [57,58] which is presumably located in the grain boundary regions and is gradually diminished with hydrogen incorporation in the UNCD film structure. In the $\sigma*$ region of the C K edge, wider but significant peaks within the range of 291.0–292.8 eV (centred at ~291:9eV) and 293–308 eV (centred at ~295:8eV) are observed and they are assigned as $\sigma*$(C-C) and $\sigma*$ (C–N and C=N) bonds, respectively [59]. it is observed that the $\pi*$ peak position in C K-edge XANES spectra shifts with change of hydrogen incorporation that implies a structural transformation occurs in the UNCD thin films structure.

4.3.9 Current (I) – Voltage (V) relationships of UNCD thin films

The I-V characteristics of these N-doped UNCD thin films are shown in figure 4.12. This UNCD shows that the current gradually decreases when hydrogen flow rate increases gradually during the deposition process. It is also observed that the results do not vary significantly when the measurements are repeated without changing the electrode contact *i.e.* two cycles measurements shows the same results indicating the UNCD are very hard materials and very useful for low current in hard materials devices.
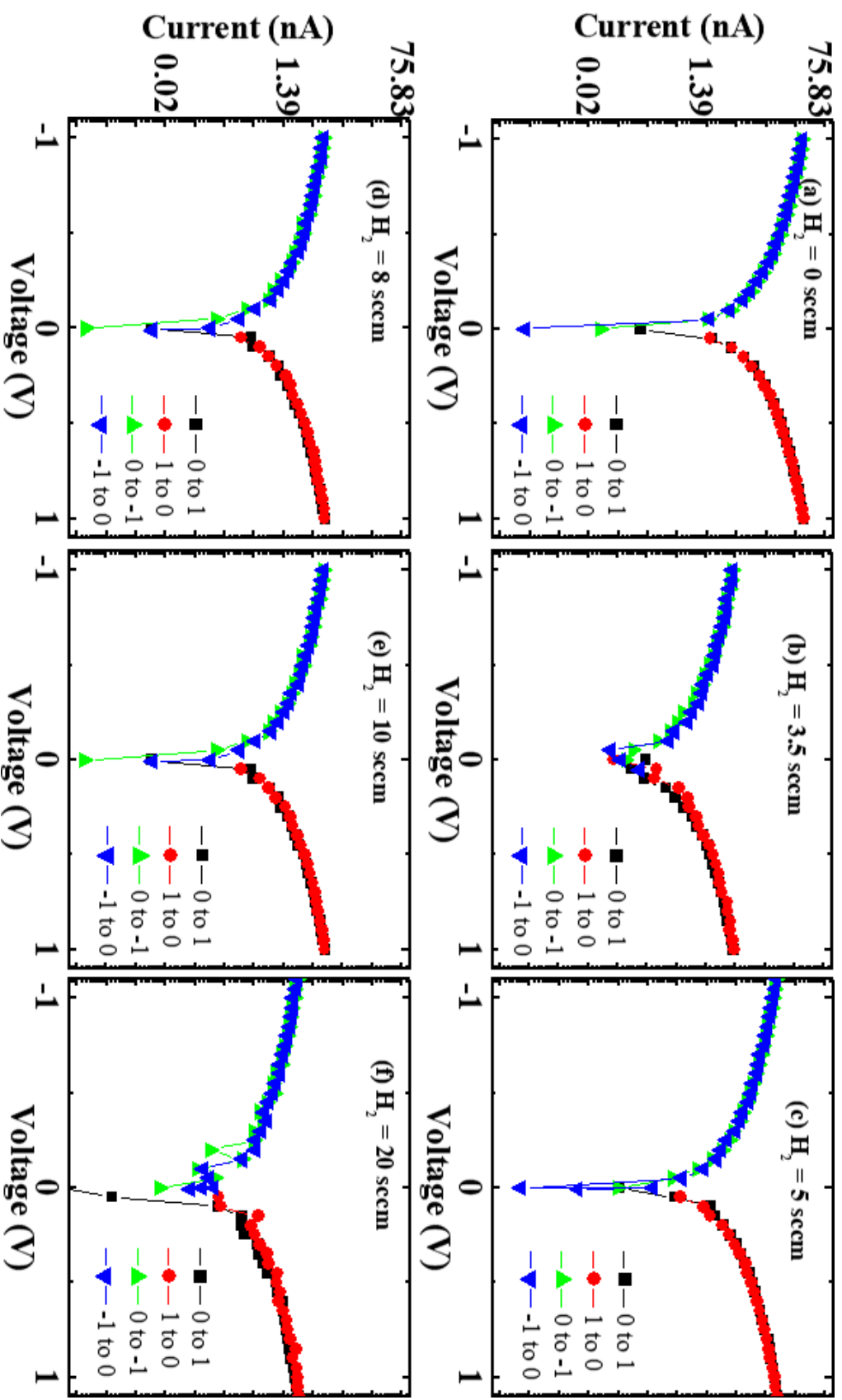
Figure 4.12: *Current (I) – voltage (V) characteristics curve of UNCD thin films synthesized at different hydrogen flow rate (sccm) with constant N₂/Ar flow = 5 sccm.*

The I–V curve of the UNCD shows a hysteresis loop that indicates the bipolar resistive switching effect and shows ferro-electric behaviours. The loop area is not significantly changing for all UNCD. The UNCD layer is considered mainly as sp^3 bonded carbon and the physical properties of UNCD can be modulated by the sp^3 bonded carbon on the surface [60]. When there is a significant amount of carbons and nitrogen bonded groups formed through incorporation of N_2 gas during preparation on the UNCD structure, the conductance of UNCD is assumed to be high due to reducing the sp^3 bonding feature. But with the increase of hydrogen flow rate during UNCD preparation the conductivity as well as the area of hysteresis loop decreases implies an increase of sp^3 content in the UNCD structure. However, these UNCD thin films could be useful for the devices, where low current is necessary and in the same time materials should be very hard as UNCD is sp^3-rich hard materials.

4.3.10 Summary

In conclusion, UNCD thin films were prepared by MW-PECVD system in $CH_4/N_2/Ar/H_2$ plasma atmosphere on silicon substrates. In H_2 incorporation effects on N-doped UNCD films were studied systematically by different spectroscopy and microscopy measurements. XRD and surface morphology study shows the formation of needle-like structure UNCD. The XANES and Raman spectra have demonstrated the presence of diamond, amorphous carbon and other defects in the UNCD films and are consistent with the results of electron field emission data and hardness/Young's modulus values. The highest Hardness (Young's modulus) of these films 30 GPa (300 GPa) is correlated with their microstructure, electronic structure and bonding properties. The differences in the spectral features of Raman scattering are caused by the different scattering cross sections of the amorphous matrix for resonant Raman process when changing the excitation energy. The narrow peaks (1332 cm^{-1}) sitting on the background of wide bands in the whole 830–1950 cm^{-1} region indicate the presence of well-

definable molecular structural units from the grain boundaries in the studied spatial region besides the diamond crystallites and the amorphous carbon matrix. It is also observed that the change of small amount of N_2 content (see table 1), change their C-sp^3 hybridization and hence change their conductivity, work function as well as VBM results in change of Young's modulus and hardness of the films. These films are reproducible with the growth conditions and growth parameters in correlation with plasma features, and their feasibility to be used for the envisaged different electronic and coating technology applications has been established in this work.

References

[1]   Zhou, D., McCauley, T.G., Qin, L.C., Krauss, A.R., Gruen, D.M., 1998. *Synthesis of nanocrystalline diamond thin films from an Ar–CH$_4$ microwave plasma.* J. Appl. Phys, 83(1), pp.540-543.

[2]   Gruen, D. M., 1999. *Nanocrystalline diamond films.* Ann. Rev. Mater Sci., 29(1), pp.211-259.

[3]   Popov, C., Favaro, G., Kulisch, W., Reithmaier, J.P., 2009. *Influence of the nucleation density on the structure and mechanical properties of ultrananocrystalline diamond films.* Diam. Relat. Mater., 2009, 18(2-3): 151-154.

[4]   Shen L, Chen Z., 2009. *A study of mechanical properties of pure and nitrogen-doped ultrananocrystalline diamond films under various loading conditions.* Int. J. Solids Struct., 46(3-4), pp.811-823.

[5]   Kovalchenko, A.M., Elam, J.W., Erdemir, A., Carlisle, J.A., Auciello, O., Libera, J.A., Pellin, M.J., Gruen, D.M. and Hryn, J.N., 2011. *Development of ultrananocrystalline diamond (UNCD) coatings for multipurpose mechanical pump seals.* Wear, 270(3-4), pp.325-331.

[6]   Kumar, N., Sharma, N., Dash, S., Popov, C., Kulisch, W., Reithmaier, J.P., Favaro, G., Tyagi, A.K. and Raj, B., 2011.*Tribological properties of ultrananocrystalline diamond films in various test atmosphere.* Tribol. Int.,44(12), pp.2042-2049.

[7]   Corrigan, T.D., Gruen, D.M., Krauss, A.R., Zapol, P., Chang, R.P., 2002. *The effect of nitrogen addition to Ar/CH$_4$ plasmas on the growth, morphology and field emission of ultrananocrystalline diamond.* Diam. Relat. Mater., 11(1), pp.43–48.

[8]   Erdemir, A.T., Fenske, G.R., Krauss, A.R., Gruen, D.M., McCauley, T., Csencsits, R.T., 1999. *Tribological properties of nanocrystalline diamond films.* Surf. Coat. Tech., 120, pp.565-572.

[9]   Mubarok F., Carrapichano J., Almeida F., Fernandes A.J.S., Silva, R.F., 2008. *Enhanced sealing performance with CVD nanocrystalline diamond films in self-mated mechanical seals.* Diam. Relat. Mater., 17(7-10), pp.1132-1136.

[10]   West, C., Netzel, J., 2008. Diamond—its effect on the seal industry. *World Pumps*, *2008*(504), pp.50-52.

[11]   Birrell, J., Carlisle, J.A., Auciello, O., Gruen, D.M., Gibson, J.M., 2002. *Morphology and electronic structure in nitrogen-doped ultrananocrystalline diamond.* Appl. Phys. Lett., 81, pp.2235–2237.

[12]   Shenderova, O.A., Gruen, D.M., 2006. *Ultrananocrystalline Diamond Synthesis, Properties and Application.* p. 296. William Andrew Publishing, Norwich, U.K.

[13]   Zapol, P., Sternberg, M., Curtiss, L.A., Frauenheim, T., Gruen, D.M., 2001. *Tight-binding molecular-dynamics simulation of impurities in ultrananocrystalline diamond grain boundaries.* Phys. Rev. B, 65(4), p.045403.

[14]   Zapol, P., Sternberg, M., L. Curtis, L.A., Frauenheim, T., Gruen, D.M., 2002. *Tight-binding molecular-dynamics simulation of impurities in ultrananocrystalline diamond grain boundaries.* Phys. Rev. B, 65(4), pp. 1-11.

[15]   Birrell, J., Gerbi, J.E Auciello, O., Gibson, J.M., Gruen, D.M., Carlisle, J.A., 2003. *Bonding structure in nitrogen doped ultrananocrystalline diamond.* J. Appl. Phys., 93(9), pp. 5606–5612.

[16]   Arenal, R., Montagnac, G., Bruno, P., Gruen, D.M., 2007. *Multiwavelength Raman spectroscopy of diamond nanowires present in n-type ultrananocrystalline films.* Phys. Rev. B, 76(24), p.245316.

[17]   Martin, J.A., Vazques, L., Bernard, P., Comin, F., Ferrer, S., 1990. *Epitaxial growth of crystalline, diamondlike films on Si (100) by laser ablation of graphite.* Appl. Phys. Lett., 57, pp.1742–1744.

[18] Rani, R., Panda, K., Kumar, N., Titovich, K.A., Ivanovich, K.V., Vyacheslavovich, S.A. and Lin, I.N., 2018. *Tribological Properties of Ultra-nanocrystalline Diamond Films: Mechanochemical Transformation of Sliding Interfaces.* Sci. Rep., 8 (283).

[19] Shuo, Y.A.N.G., Weidong, M.A.N., Jilei, L.Y.U., Xiong, X.I.A.O., Zhiheng, Y.O.U., Jiang, N., 2017. *Growth of mirror-like ultra-nano-crystalline diamond (UNCD) films by a facile hybrid CVD approach.* Plasma Sci. Technol. 19(5), p.055505.

[20] Jie, L.I.U., Hei, L.F., Chen, G.C., Li, C.M., Tang, W.Z. and Lu, F.X., 2013. *Growth of ultrananocrystalline diamond films in an Ar-rich $CH_4/H_2/Ar$ atmosphere with varying H_2 concentrations.* New Carbon Mater., 28(2), pp.134-138.

[21] Chen, H.C., Wang, C.S., Lin, I.N., Cheng, H.F., 2011. *Defect structure for the ultra-nanocrystalline diamond films synthesized in H_2-containing Ar/CH_4 plasma.* Diam. Relat. Mater., 20(3): 368-373.

[22] Jiao S, Sumant A, Kirk M., Jiao, S., Sumant, A., Kirk, M.A., Gruen, D.M., Krauss, A.R. and Auciello, O., 2001. *Microstructure of ultra-nanocrystalline diamond films grown by microwave Ar–CH plasma chemical vapor deposition with or without added H_2.* J. Appl. Phys., 90(1): 118-122.

[23] Huang, B.R., Wu, C.H., Ke, W.Z., 1999. *Surface analysis of boron-doped polycrystalline diamond films deposited by a microwave plasma chemical vapor deposition system.* Mater. Chem. Phys.,59(2). 143–148.

[24] Dischler, B., Bubenzer, A., Koidl, P., 1983. *Bonding in hydrogenated hard carbon studied by optical spectroscopy.* Solid State Commun., 48(2), pp.105-108.

[25] Tang, C.J., Neves, A.J., Carmo, M.C., 2005. *Infrared absorption study of hydrogen incorporation in thick nanocrystalline diamond films.* Appl. Phys. Lett., 86(22), p.223107.

[26] Popov, C., Kulisch, W., Gibson, P.N., Ceccone, G., Jelinek, M., 2004. *Growth and characterization of nanocrystalline diamond/amorphous carbon composite films prepared* by *MWCVD*. Diam. Relat. Mater., 13(4-8), pp.1371-1376.

[27] Aggadi, N., Arnas, C., Bénédic, F., Dominique, C., Duten, X., Silva, F., Hassouni, K. and Gruen, D.M., 2006. *Structural and chemical characterization of soot particles formed in Ar/H$_2$/CH$_4$ microwave discharges during nanocrystalline diamond film synthesis. Diam. Relat. Mater.*, 15(4–8), pp. 908–912.

[28] John, P., Milne, D.K., 1992.Attenuated total reflection infrared absorption in CVD diamond films, in *Diamond Optics V*, vol. 1759 of *Proceedings of SPIE*, July; San Diego, Calif, USA, pp. 209–217.

[29] McNamara, K.M., Williams, B.E., Gleason, K.K., Scruggs, B.E., 1994. *Identification of defects and impurities in chemical-vapordeposited diamond through infrared spectroscopy*. J. of Appl. Phys., 76(4), pp.2466-2472.

[30] Correa, E.J., Wu, Y., Wen, J.G., Chandrasekharan, R., Shannon, M.A., 2007. *Electrical conduction in undoped ultrananocrystalline diamond thin films and its dependence on chemical composition and crystalline structure.* J. Appl. Phys., 102(11), p.113706.

[31] Sails, S.R., Gardiner, D.J., Bowden, M., Savage, J., Rodway, D., 1996. *Monitoring the quality of diamond films using Raman spectra excited at 514.5nm and 633 nm.* Diam. Relat. Mater., 5(6–8) (1996) 589–591.

[32] Klauser, D. Steinmüller-Nethl, R., Kaindl, E., Bertel, N. Memmel, N., 2010. *Raman studies of nano-and ultra-nanocrystalline diamond films grown by hot-filament CVD.* Chem. Vap. Depos., 16(4–6), pp.127–135.

[33] Ferrari, A.C., Robertson, J., 2004. *Raman spectroscopy of amorphous, nanostructured, diamond–like carbon, and nanodiamond*. Philos. T. R. Soc. A, 362(1824), pp.2477–2512.

[34] Ferrari, A.C., Robertson, J., 2001. *Origin of the 1150 cm^{-1} Raman mode in nanocrystalline diamond.* Phys. Rev. B: Condens. Matter. Mater. Phys., 63(12), p.121405.

[35] Ferrari, A.C., Robertson, J., 2001. *Resonant Raman spectroscopy of disordered, amorphous, and diamondlike carbon.* Phys. Rev. B, 64(7), p.075414.

[36] Pfeiffer, R., Kuzmany, H., Knoll, P., Bokova, S., Salk, N., Günther, B., 2003. *Evidence for trans-polyacetylene in nano-crystalline diamond films.* Diam. Relat. Mater., 12(3-7), pp.268-271.

[37] Birrell, J. Gerbi, J.E., Gibson, J.M., Gruen, D.M., LA Carlisle., 2003. *Bonding structure in nitrogen doped ultra-nanocrystalline diamond.* J. Appl. Phys., 93(9) (2003), pp.5606–5612.

[38] Ferrari, A. C., Robertson, J., 2000. *Interpretation of Raman spectra of disordered and amorphous carbon*. Phys. Rev. B, 61(20), p.14095.

[39] Ferrari, A. C., Robertson, J., 2004. *Raman spectroscopy of amorphous, nanostructured, diamond–like carbon, and nanodiamond*. Phil. Trans. R. Soc. Lond. A, 362(1824), pp.2477-2512.

[40] Feng, J., Xie, Y.N., Li, Z., Wu, X.Z., Li, J.G., Me, J., Yu, Z.M., We, Q.P., 2015. *Microscopic mechanical characteristics analysis of ultranano-crystalline diamond films.* Trans. Nonferrous Met. Soc. China, 25, p.3291.

[41] Lodes, M.A., Kachold, F.S., Rosiwal, S.M., 2015. *Mechanical properties of micro- and nanocrystalline diamond foils.* Philos. Trans. A Math. Phys. Eng. Sci. 373(2038) p.20140136.

[42] Shalini, J., Sankaran, K.J., Dong, C.L., Lee, C.Y., Tai, N.H., Lin, I.N., 2013. *In situ detection of dopamine using nitrogen incorporated diamond nanowire electrode.* Nanoscale 5(3), pp.1159-1167.

[43] Zheng, W.T., Sjöström, H., Ivanov, I., Xing, K.Z., Broitman, E., Salaneck, W.R., J. E. Greene, J.E., Sundgren, J.E., 1996. *Reactive magnetron sputter deposited CNx: Effects of N_2 pressure and growth temperature on film composition, bonding, and microstructure.* J. Vac. Sci. Technol. A, 14, p.2696.

[44] Zheng, W.T. K. Z., Xing, K.Z., Hellgren, N., Lögdlund, Johansson, M.A., Gelivs, U., Salaneck, W.R., Sundgren, J.E.,1997. *Nitrogen 1s electron binding energy assignment in carbon nitride thin films with different structures.* J. Electron. Spectrosc. Relat. Phenom. 87, p.45.

[45] Rani, R., Panda, K., Kumar, N., Titovich, K.A., Ivanovich, K.V., Vyacheslavovich, S.A., Lin, I.N., 2018. *Tribological Properties of Ultra nanocrystalline Diamond Films: Mechanochemical Transformation of Sliding Interfaces.* Sci. Rep. 8, p.283.

[46] McFeely, F.R., Kowalczyk, S.P., Ley, L., Cavell, R.G., Pollak, R.A., Shirley, D.A., 1974. *X-ray photoemission studies of diamond, graphite, and glassy carbon valence bands.* Phys. Rev. B, 9(12), p.5268.

[47] Mansour, A., Ugolini, D., 1993. *Photoelectron-spectroscopy study of amorphous a-CNx:H,* Phys. Rev. B 47(16), p.10201.

[48] Birrell, J., Gerbi, J.E., Auciello, O., Gibson, J.M., Gruen, D.M. and Carlisle, J.A., 2003. *Bonding structure in nitrogen doped ultrananocrystalline diamond.* J. Appl. Phys, 93(9), pp.5606-5612.

[49] Xiao, X., Birrell, J., Gerbi, J.E., Auciello, O., Carlisle, J.A., 2004. *Low temperature growth of ultrananocrystalline diamond.* J. of Appl. Phys., 96(4), pp.2232-2239.

[50] Joseph, P.T., Tai, N.H., Chen, C.H., Niu, H., Cheng, H.F., Pong, W.F. and Lin, I.N., 2009. *On the mechanism of enhancement on electron field emission properties for ultrananocrystalline diamond films due to ion implantation.* J. Phys. D: Appl. Phys., 42(10), p.105403.

[51] Coffman, F.L., Cao, R., Pianetta, P.A., Kapoor, S., Kelly, M., Terminello, L.J., 1996. *Nearedge xray absorption of carbon materials for determining bond hybridization in mixed sp^2/sp^3 bonded materials.* Appl. Phys. Lett., 69(4), pp.568-570.

[52] Lin, C.R., Liao, W.H., Wei, D.H., Chang, C.K., Fang, W.C., Chen, C.L., Dong, C.L., Chen, J.L., Guo, J.H., 2011. *Improvement on the synthesis technique of ultrananocrystalline diamond films by using microwave plasma jet chemical vapor deposition.* J. Cryst. Growth, 326(1), pp.212-217.

[53] Chang, Y.K., Hsieh, H.H., Pong, W.F., Tsai, M.H., Chien, F.Z., Tseng, P.K., L. Chen, L. C., Wang, T.Y., Chen, K.H., D. M. Bhusari, D.M., Yang J.R., and Lin, S.T., 1999. *Quantum confinement effect in diamond nanocrystals studied by X-ray-absorption spectroscopy.* Phys. Rev. Lett., 1999, 82, 5377.

[54] Shang, N., Papakonstantinou, P., Wang, P., Zakharov, A., Palnitkar, U., Lin, I.N., Chu, M., Stamboulis, A., 2009. *Self-assembled growth, microstructure, and field-emission high-performance of ultrathin diamond nanorods.* Acs Nano, 3(4), pp.1032-1038.

[55] Madaleno, J.C., Singh, M.K., Titus, E., Cabral, G., Grácio, J. and Pereira, L., 2008. *Electron field emission from patterned nanocrystalline diamond coated a-SiO$_2$ micrometer-tip arrays.* Appl. Phys. Lett., 92(2), p.023113.

[56] Ohmagari, S., Yoshitake, T., Nagano, A., Ohtani, R., Setoyama, H., Kobayashi, E., Hara, T., Nagayama, K., 2010. *Formation of p-type semiconducting ultrananocrystalline diamond/hydrogenated amorphous carbon composite films by boron doping.* Jpn. J. Appl. Phy., 49(3R), p.031302.

[57]   Yoshitake, T., Nagano, A., Ohmagari, S., Itakura, M., Kuwano, N., Ohtani, R., Setoyama, H., Kobayashi, E. and Nagayama, K., 2009. *Near-edge x-ray absorption fine-structure, x-ray photoemission, and Fourier transform infrared spectroscopies of ultrananocrystalline diamond/hydrogenated amorphous carbon composite films.* Jpn. J. Appl. Phys., 48(2R), p.020222.

[58]   Laikhtman, A., Gouzman, I., Hoffman, A., Comtet, G., Hellner, L., Dujardin, G., 1999. *Sensitivity of near-edge x-ray absorption fine structure spectroscopy to ion beam damage in diamond films.* J. Appl. Phys., 86(8), pp.4192-4198.

[59]   Barradas, N.P., Khan, R.U.A., Anguita, J.V., Silva, S.R.P., Kreissig, U., Gro tzschel, R., Moller W., 2000. *Growth and characterisation of amorphous carbon films doped with nitrogen.* Nucl. Instrum. Methods Phys. Res., Sec.B (161–163), p.969.

[60]   Ray, S.C., Lin, I.N., 2015. *Ferroelectric behaviours of ultra-nano-crystalline diamond thin films.* Surf. Coat. Technol., 271, pp.247–250

Chapter 5

Conclusion and recommendations for future work

5.1 Conclusions

UNCD thin films were prepared by MW-PECVD system in $CH_4/N_2/Ar/H_2$ plasma atmosphere on silicon substrates. In H_2 incorporation effects on N-doped UNCD films were studied systematically by different measurements results. XRD and surface morphology study shows the formation of needle-like structure UNCD. The highest Hardness (Young's modulus) of these films 30 GPa (300 GPa) is correlated with their microstructure, electronic structure, and bonding properties. C K-edge XANES and Raman spectra have demonstrated the presence of diamond, amorphous carbon and other defects in the UNCD films and are consistent with the results of electron field emission data and hardness/Young's modulus values. The differences in the spectral features of Raman scattering are caused by the different scattering cross sections of the amorphous matrix for resonant Raman process when changing the excitation energy. The narrow peaks (1332 cm^{-1}) sitting on the background of wide bands in the whole 830–1950 cm^{-1} region indicate the presence of well-definable molecular structural units from the grain boundaries in the studied spatial region besides the diamond crystallites and the amorphous carbon matrix. Again, the incorporation of small content of N_2 species into Ar plasma modifies the microstructure of UNCD films as investigated using electrical measurements. As generally defined, the positive voltage applied to the p-type Si side is a forward bias. The hetero-junction exhibited a typical rectifying action of p–n junction diodes. UNCD is slightly p-type as grown. As nitrogen is added, this material becomes n-type with very shallow activation energy. The origin of this conductivity is related to disorder and π bonding at the grain boundaries, which introduce states within the gap and band tails, resulting in high carrier concentrations and low mobilities. The grown UNCD films are composed of nano-crystalline diamond grains and a structurally disordered mixture of sp^3/sp^2-bonded carbons in the grain boundaries.

Upon introducing nitrogen into UNCD films, the most energetically favourable sites should be at the grain boundaries, where the lone pair electrons in nitrogen can facilitate the transformation of tetrahedral coordinated sites of sp^3-like carbon configuration into a three-fold-coordinated site of sp^2-like carbon arrangement with a perturbed N-doped characteristic at the grain boundaries. Thus, the incorporation of nitrogen into UNCD films could lead to an increase in amorphous sp^2-bonded (π-) carbon phase by the formation of conjugated networking of the chain-like sp^2 and sp^1 hybridized with N-doped structures together with aromatic carbon clusters in the grain boundaries as evidenced by the results of Raman and XPS spectral investigations.

5.2 Recommendations for future work

In this present work, the UNCD are synthesized using different gas flow as listed in table 1; where N_2/Ar gas flow ratio kept constant for all UNCD *i.e*. 5 sccm and hydrogen gas flow was varied 0 sccm to 20 sccm.

In our future work, it is proposed to prepare the UNCD films by changing the N_2/Ar gas flow ratio by 10 sccm, 15 sccm and 20 sccm respectively and the hydrogen gas flow will be the same as our preset work *i.e.* varied from 0 sccm to 20 sccm. Our motivation will be the change of structural properties with their electrical behaviour.

Appendix

Microstructure and electronic properties of ultra-nano-crystalline-diamond thin films

R.W. Thoka[a], S.J. Moloi[a], Sekhar C. Ray[a],*, W.F. Pong[b],*, I.-N. Lin[b]

[a] DEPARTMENT of Physics, CSET, University of South AFRICA, PRIVATE BAG X6, FLORIDA, 1710, Science CAMPUS, CHRISTIAAN de Wet AND Pioneer Avenue, FloridA PARK, JOHANNESBURG, South AFRICA
[b] DEPARTMENT of Physics, TAMKANG University, TAMSUI 251, TAIPEI, TAIWAN

ABSTRACT

Ultra-nano-crystalline diamond (UNCD) thin films with average thickness ~200 nm, were grown on n-type mirror polished silicon (100) substrates using microwave plasma enhanced chemical vapour deposition system in different gas (H_2-N_2-Ar-CH_4) composition plasma atmospheres at 1200 W (2.45 GHz) and in a pressure of 120 Torr with plasma-temperature ~475 °C. Raman spectroscopy was used for microstructural study and nano-indentation was used for Hardness/Young's modulus study; whereas X-ray absorption near edge structure, X-ray photoelectron and ultraviolet photoemission spectroscopies were used for electronic structure of UNCD thin films. The hardness of the films is found to be ~30 GPa, Young's modulus ~300 GPa and induced electron field emission, the turn on electric field, E_{TOE} = 11 V/µm. All results show that the UNCD could be useful for different industrial semiconductor/optoelectronic devices and as flexible materials for thin film coating technology.

1. Introduction

Ultra-nano-crystalline diamond (UNCD) thin films has ultra-small diamond grains ranging between 5–10 nm and smooth surface characteristics with a special form of diamond films. UNCD is now a material of research interest because of its exclusive granular structure [1] and it has been the subject of a large interest since the establishment of its deposition more than 30 years ago. UNCD films are more than 90% sp^3 character with grain boundaries having a mixture of sp^2, sp^3, hydrocarbon, and amorphous carbon (a-C). In this mixture sp^2 character is predominant [2]. Because of an outstanding crystal structure compared to other forms of diamond films (microcrystalline or nano-crystalline), UNCD has an excellent mechanical and optical properties, high surface area and tuneable surface structure [3], high surface acoustic wave velocity, high electron mobility, high thermal conductivity, and good chemical and thermal stability. UNCD is also a material of interest for fabrication of high performance electronic devices applied in high temperature and heavy radiation environments [4] and application such as cold cathode field emitters and other vacuum microelectronic devices [5]. In addition these UNCD could be useful for drug discovery, drug delivery, biomedical implants and cell purifiers, microfluidics, inertial navigation, printing, various sensors, night vision, IR emitters, telephone/DSL switching, RF devices, power management, and several others [4,5].

Different processes have been used to synthesis UNCD films [6–8]. Gruen et al. have deposited nano-crystalline diamond films on scratched Si(100) from hydrogen-poor argon plasma using fullerenes as growth precursors [9]. Chakrabarti et al. obtained nano-diamond crystallites by introducing camphor into the CVD chamber [10]. Adding N_2 and/or N_2/Ar to a plasma with a high methane concentration can also produce nano-crystalline diamond [11,12]. With all processes/techniques followed/adopted to synthesise the films, a reproduction of UNCD films with properties suitable for specific applications requires the optimized and controllable growth process. In this case, different stable process parameters ensuring the reproducibility of growth conditions and their influences on the film characteristics can be investigated in correlation with plasma features.

In this work, the UNCD thin films were synthesized by controlling the composition of H_2-N_2-Ar-CH_4 gases, such that the estimated C-content is ≥95 at% and (O_2+N_2)-content is < 5 at% for the modification of microstructural, electronic and transport properties of UNCD films for different electronic devices and coating technology applications. In this work, we have used low concentration nitrogen to make defect induced UNCD films; where nitrogen- carbon bonding is formed and nitrogen is not adhere on the surface of UNCD. We have used X-ray absorption near edge structure (XANES) spectroscopy, X-ray photoelectron spectroscopy (XPS), ultra-violet photoemission spectroscopy (UV-PES), X-ray diffraction pattern (XRD), Fourier transform

* Corresponding authors.
  E-MAIL ADDRESSES: Raysc@unisa.ac.za (S.C. Ray), wfpong@mail.tku.edu.tw (W.F. Pong).

infra-red spectroscopy (FTIR), Raman spectroscopy, field-emission scanning electron microscopy (FE-SEM) images, nano-indentation (Hardness, Young's modulus) for study different properties of synthesized UNCD thin films. A correlation of micro- and electronic structure with mechanical properties of the films have been explained and the feasibility of using the material for envisaged electronic and coating technology applications was established.

2. Experimental details

The UNCD thin films were grown on n-type mirror polished silicon (100) substrates using microwave plasma enhanced chemical vapour deposition (MW-PECVD) system. The silicon (100) substrates were first ultrasonically cleaned by acetone to remove native-oxides and any other surface contamination and then dipped in 40% HF solution for 1 min to etch the surface oxide layer, followed by ultra-sonication in diamond powder (30 nm) slurry of methanol solution. The substrates with diamond powder (30 nm) slurry of methanol solution, were again ultrasonically cleaned and dried by blowing pure N_2 gas. The UNCD films were grown at different composition gas plasma atmospheres at 1200 W (2.45 GHz) in a 120 Torr chamber pressure. The total gas flow rate was 100 sccm; which contains 85–90 sccm CH_4+Ar, 5–10 sccm H_2 with 5 sccm of N_2 gas. No external heater was used and the substrate temperature was estimated to be ~475 °C during the growth of the UNCD films, which was presumably heated due to the bombardment of the plasma species. The thickness of the UNCD films was ~200 nm, which was estimated from a cross-sectional field emission scanning electron microscopic image as described in details elsewhere [13,14]. A very few amount of nitrogen content (0.48–1.32 at%) was found in the UNCD film structure that was estimated from the elemental and compositional analysis XPS measurements. The microstructural, electronic and bonding properties were studied using XRD, FE-SEM, FTIR, Raman, XANES, XPS and UV-PES techniques. Raman measurements were carried out using LASER excitation wavelengths ~532 nm with the LASER beam spot size ~1 μm and the incident power was ~1 mW. The XPS and UV-PES measurements were carried out with spatial resolution of < 3 μm using KRATOS AXIS X-ray photoelectron spectrometer at UNISA (Florida Science Campus), South Africa. The nanomechanical characterizations of UNCD films were measured using a nanoindenter. The C K-edge XANES spectra were measured using the HSGM beam line at the Taiwan light source, Hsinchu, Taiwan. The Electric Field Emission (EFE) measurements were also performed using Keithley power supply.

3. Results and discussion

Fig. 1(a) shows XRD patterns for the UNCD films grown with 1.32%, 0.92% and 0.48% N_2 concentration. Different nitrogen content (i.e. N_2 at%) present in UNCD films were estimated from XPS spectra and are discussed later with the elemental/quantificational analysis tabulated in Table 1. Each spectrum of UNCD has relatively sharp and narrow diffraction peaks with 2θ values of ~44.4° and ~75.4° that can be ascribed to the diffraction of the (111) and (220) crystallographic planes of the cubic diamond respectively [15,16]. Apart from these two diamond peaks, two shoulders observed at ~24.4° (For N_2 ~ 0.48 at% and ~0.92 at%) and ~37.7° (For N_2 ~ 1.32 at%) respectively are assigned to (002) and (004) sp^2-diamond peaks. XRD analysis is usually used to characterize the nano-crystalline nature and the full width that half maximum (FWHM) of the films. The (111) and (220) peaks at ~44.4° and ~75.4° are diamond peaks. The (111) diamond peak in the diffraction patterns of the films is slightly broadened because of the non-crystalline structure of these films. The average crystallite size of the UNCD can be estimated from the line widths using the Scherrer formula, $d = 0.9\lambda / (B \times \cos\theta)$; where λ =0.1541 nm is the x-ray wavelength, B is the FWHM of the diffraction peak, and θ is the Bragg angle. The estimated crystal size is approximately ~5–7 nm.

Fig. 1(b–d) shows the surface morphology of UNCD films deposited on the silicon substrates with different N_2 concentrations from 1.32 at.% →0.92 at.% →0.48 at.%. A Surface morphology of the films shows densely packed homogeneously needle-like clusters distributed UNCD grains looking like diamond nanowires [17]. It can be seen that the grain size varies slightly with N_2 concentration and the average grain size is ~6 nm when N_2 concentration is 1.32%. It is also observed that the UNCD needle-like clusters are similar for the films having higher nitrogen concentration (1.32 at% & 0.92 at%) but become more ag- glomerated at low N_2-concentration (0.48 at%). It could be clearly seen that when the N_2-content was 1.32 at% the surface of diamond films was the smoothest and the grains size was the finest among these films. The FT-IR absorption spectra of UNCD thin films shows different vibration modes in the range 400–3800 cm^{-1} [18] as shown in Fig. 1(e). The diamond crystallites contain all of sp^3-hybridized carbon atoms and both of the sp^3-hybridized and sp^2-hybridized carbon atoms are present in the grain boundaries of the diamond films. In this case, oxygen phenomena will occur more easily in the grain boundaries since more dangling bond exist. Other several absorption bands are observed in the spectral range 2800–3100 cm^{-1}, which arise from C–H stretch vibrations, suggesting an hydrogenation process on UNCD film surfaces, which was achieved during synthesis process. The C–H vibrational fre- quencies could be assigned according to the type of carbon hybridiza- tion (sp^3, sp^2 or sp^1) and to the type of group (C-H$_3$, C-H$_2$, or C-H). The C-H stretch frequency depends weakly only on the arrangement of the more distant neighbours, suggesting the incorporation of hydrogen on non-crystalline or defective region of the films. A several bands in the region 1020–1370 cm^{-1}, usually assigned to the C-O-C stretching vibration, suggest that the UNCD films are oxidized during growth process [18]. The peak observed at ~2375 cm^{-1} is due to environmental CO_2 and/or C-N bonds [19].

Fig. 1(f) shows the Raman spectra of UNCD films deposited with different nitrogen concentration viz. ~1.32 at%, ~0.92 at% and ~0.48 at% in CH_4-rich atmosphere (≥85 sccm). The typical different spectral features are (i) a broad band at ~1332 cm^{-1} from nano-diamond, (ii) the broad band of the range ~1380—1630 cm^{-1} (centred at ~1554 cm^{-1}) which is sp^2-bonded carbon features for graphite D & G-bands, and (iii) the C–H vibration characteristics of short-chain conjugated trans-polyacetylene (t-PA) phases originating from the grain boundaries of UNCD films at ~1193 cm^{-1} together with a weak peak at ~1460 cm^{-1} [20]. This t-PA-phase peaks are considered as the fingerprint for UNCD films [21] that are more prominent in these UNCD films. This further indicates the presence of extensive hydrogenated network in the grain boundaries. The graphite D & G-bands, possibly in the grain boundaries indicates the presence of amorphous and graphite phases occupying the grain boundaries. The (I_D/I_G) ratio related with (sp^2/sp^3) ratio increases with N_2-content and could be correlated with the crys- tallite size. The observed results obtained from Raman spectra confirms that all films prepare/synthesized are indeed UNCD films. This increase in the ratio could be due indicating that either the material becomes lees of sp^3 or more of sp^2 hybrids as N_2 content increases. In any case, this increase of the ratio is associated with increase of electrical conductivity of the UNCD material.

The Mechanical properties, Young's modulus (a–c), hardness (d–f) and load (g–i) as a function of displacement are shown in Fig. 2 (a–c), 2(d–f) and (g–i) respectively. In all measurements the penetration depth was limited at 4 mN (approximatively 90 nm of penetration) to minimize the influence of the substrate. Three points were tested in each UNCD with the same pressed depth. The residual pressed depths of UNCD, which is synthesized with N_2-content ~0.48 at% is lower than those of the UNCD's which were made with higher N_2-content (1.32 at % and 0.92 at%), which implies that the films of N_2-content 1.32 at%, 0.92 at% and have better elastic recovery ability. The curves of three UNCD whose modulus and hardness change with pressed depth are shown in Fig. 2(a–c) & 2(d–f). The Young's modulus and the Hardness
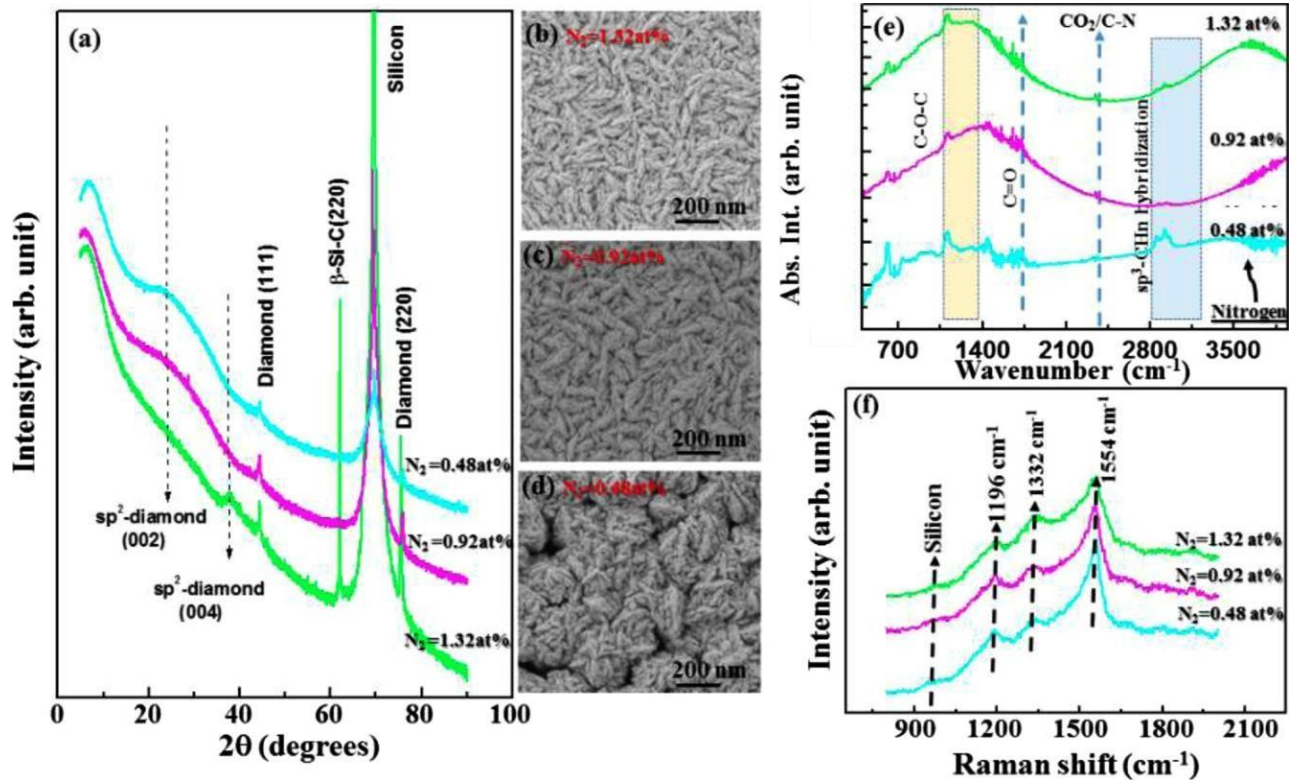
Fig. 1. Figure 1. (a) XRD, (b-d) Scanning Electron Microscopy mages, (e) FTIR and (f) Raman spectra.

14–30 GPa [Fig. 2(d–f)] respectively that are comparable with the reported values [22,23]. On a first view, the values of Hardness and the Young's modulus found for our UNCD films seem to be decrease with decreases of N_2 (at%) concentrations. These results can be explained by the presence of the amorphous carbon matrix located in the grain boundary regions of the UNCD films. It is well known that the Hardness/Young's modulus is depends on the sp^3 and/or sp^2-content presence in the UNCD structure. With increase of sp^3-content in UNCD, the Hardness/Young's modulus is increases; whereas with increase of sp^2-contents, opposite trend is observed. In our N-UNCD films, with increase of N-at%, the sp^3-content decreases and hence the Hardness/Young's modulus decreases. The Hardness/Young's modulus of these UNCD is four times lesser than single crystal natural diamond and is most suitable for different electronic devices and coating technology applications.

To understand the change in electronic structure of the UNCD films, a details investigation on the electronic and their bonding structure were carried out using XANES, XPS and UPS techniques. Fig. 3 shows the normalized C K-edge XANES spectra of UNCD films deposited with different nitrogen (at%) concentration. In these spectra, the UNCD films clearly ascertain that the major part of the carbon is the sp^3 diamond phase with a smaller amount of sp^2 graphite phase distributed the films. The small peak π*-band marked in the figure is related with graphitic

structure (C=C) and a shoulder described as C–H bonds are observed at ∼285.5 eV and ∼287:5 eV, respectively [24]. It is clear that the in- tensity of the π*-band decreases, whereas C–H bonds gradually increase with decrease (increase) of nitrogen (hydrogen) incorporation in the UNCD film structure in all XANES spectra (see Fig. 3, inset below right after background subtraction, using a best Gaussian line fit). A sharp peak at ~290 eV corresponds to the diamond electron core excitation of C 1s σ* (C–C) transitions *i.e.*, the sp^3 diamond phase [24,25]. A dip observed at ~302.1 eV attributed to the second absolute band gap for the diamond materials [24,25]. This clearly illustrates that most of the films retain an sp^3-bonding nature, regardless of nitrogen (hydrogen) incorporation. Moreover, the peak present at 285.3 eV associated with the C 1s π* transition (C=C) indicates that the films contain a small proportion of graphitic phase [26,27], which is presumably located in the grain boundary regions. The σ* region of the C K edge is wider but significant peaks within the range of 291.0–292.8 eV (centered at ∼291:9 eV) and 293–308 eV (centered at ∼295.8 eV) are observed and they are assigned as σ* (C=C) and σ* (C–N and C=N) bonds, respectively [27]. These films possess low sp^2 graphite phase implying a low electrical conductivity of the UNCD materials. We have estimated the C=C content from the integrated π* region that tabulated in Table 1. It is found that the C=C content is higher (for N_2 ∼0.9 at%) and its E_{TOE} = 11.2 V/mm, the lowest value among these UNCD films.

Table 1

Elemental composition/quantification analysis results, Raman (I_D/I_G) ratio, Young's Modulus/Hardness, turn on electric field (E_{TOE}) of synthesized UNCD thin film.

Gasses flow (sccm)			XPS elemental and quantification (at %)			Nitrogen (%)		I_D/I_G ratio	Young's modulus (Hardness) GPa	From XANES (arb. unit)		Turn on electric field, E_{TOE} (V/μm)
CH_4+Ar	N_2	H_2	C	O	N	$\frac{N}{(C+N)}$	$\frac{N}{(O+N)}$			(π*)	C-H	
90.0	5.0	5.0	96.35	2.32	1.32	1.4%	36.3%	0.95	300 (30)	0.24	1.52	13.6

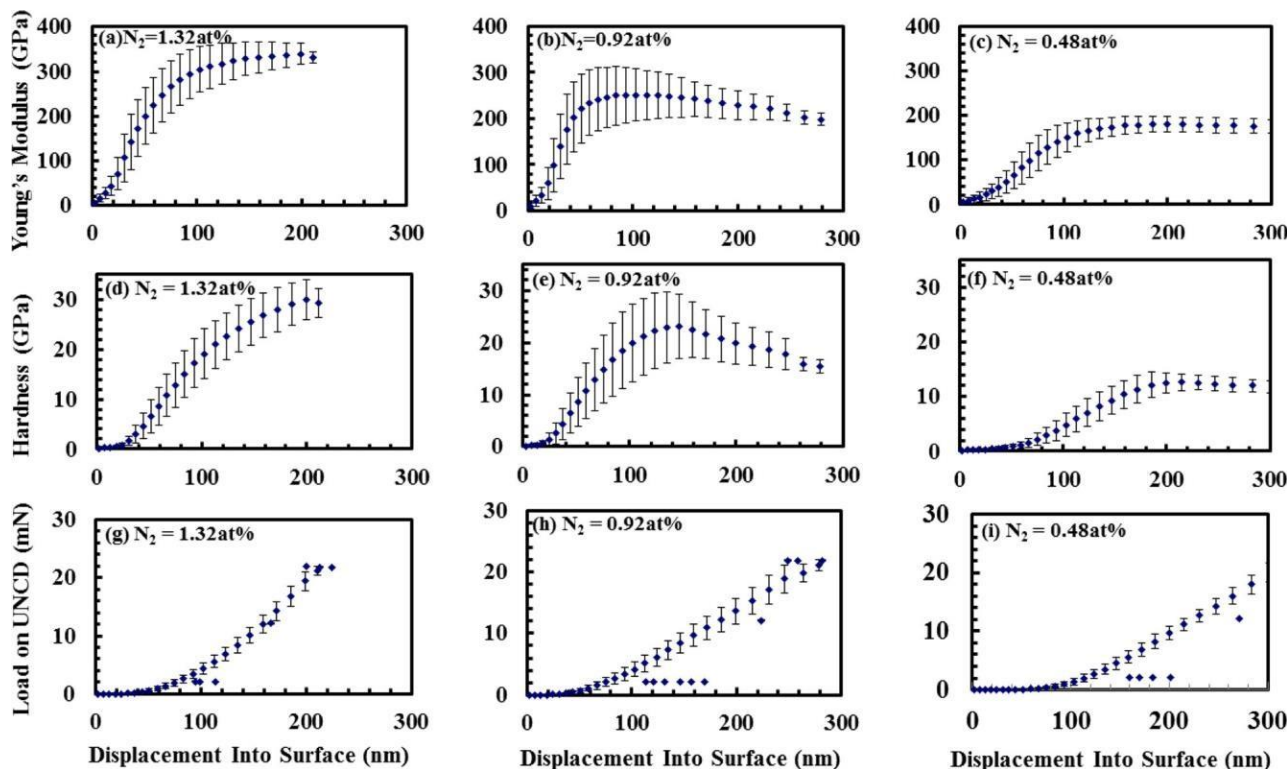| 87.0 | 5.0 | 8.0 | 95.34 | 3.73 | 0.92 | 0.9% | 19.8% | 0.57 | 250 (24) | 0.39 | 0.73 | 11.2 |
| 85.0 | 5.0 | 10.0 | 96.40 | 3.12 | 0.48 | 0.5% | 13.3% | 0.53 | 160 (14) | 0.25 | 1.17 | 15.0 |

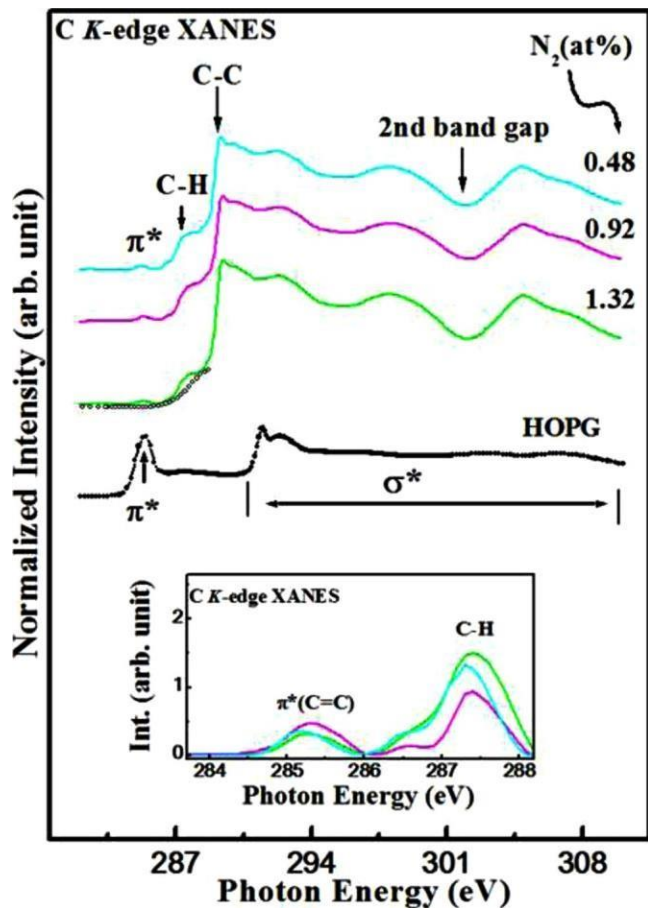Fig. 2. Figure 2. Young's modulus (a-c), Hardness (d-f) and load (g-i) as a function of displacement.

Fig. 3. -Figure 3. C_k edge XANES spectra of pai* region shows in the inset.

The elemental and quantificational analysis of all UNCD films were performed using XPS spectra that are tabulated in Table 1. The deconvoluted core level C 1s XPS spectra of UNCD films synthesized with different N$_2$-content are given in Fig. 4 (a–c). The C 1s spectra are deconvoluted in different components and are marked as peak –I, peak –II, peak–III and Peak–IV, respectively. The peak-I at binding energy ∼283.4 ± 0.3 eV and peak –II at ∼285.3 ± 0.2 eV corresponds to sp^2 C=C and sp^3 C-C hybridization bonding structures respectively [17]. The other two peaks at ∼286.5 ± 0.4 eV and 287.2 ± 0.3 eV correspond to sp^2-hybridization bonding structures of C atoms bonded to N atoms (sp^2 C▉N)/C-O-C bonds and sp^3-hybridization bonding structures of C atoms bonded to N atoms (sp^3 C–N), respectively and their relative intensities, peak width are tabulated in Table 2a. These two peaks indicate the formation of a chemical bond between C and N atoms after the incorporation of nitrogen and this is in agreement with N 1s XPS spectra of UNCD films shown in Fig. 4 (d–f). The peak at 399.8 eV within the range 397.0–402.5 eV is the contribution of N-sp^3 C and N-sp^2 C [28,29] further confirming the formation of chemical bonds between C and N atoms in UNCD structures. Fig. 4 (g–i) show the deconvoluted O 1s XPS of UNCD films, where two peaks at ∼529 eV and 532 eV correspond to O-C/ N-O and O=O bonds, respectively [21]. Deconvoluted C 1s, O 1s, and N 1s XPS parameters *viz.* peak positions, peak width and peak intensities of synthesized UNCD films are tabulated in Table 2a. As mentioned above, the N–peak is observed in the N 1s XPS within the range 397.0–402.5 eV and this peak is ascribed as the chemical bonding between C and N atoms that further confirms the formation of nitrogen doped UNCD films and this low concentration (0.48–1.32 at%) nitrogen is properly doped that formed carbon nitrogen bonds and the nitrogen is not on the surface of UNCD. It is found that with increase of N$_2$-at% concentration, C 1s (I) first decrease and then increase as indicated table-II; which is very unlikely. Again, the [N/(N+C)] and [N/(N+O)] ratios are different as shown in table-I. This change implies that carbon is not only bonded with nitrogen but also with oxygen in the matrix of N-UNCD film structure. As the N 1s XPS peak is within the range 397.0–402.5 eV; which is the combination
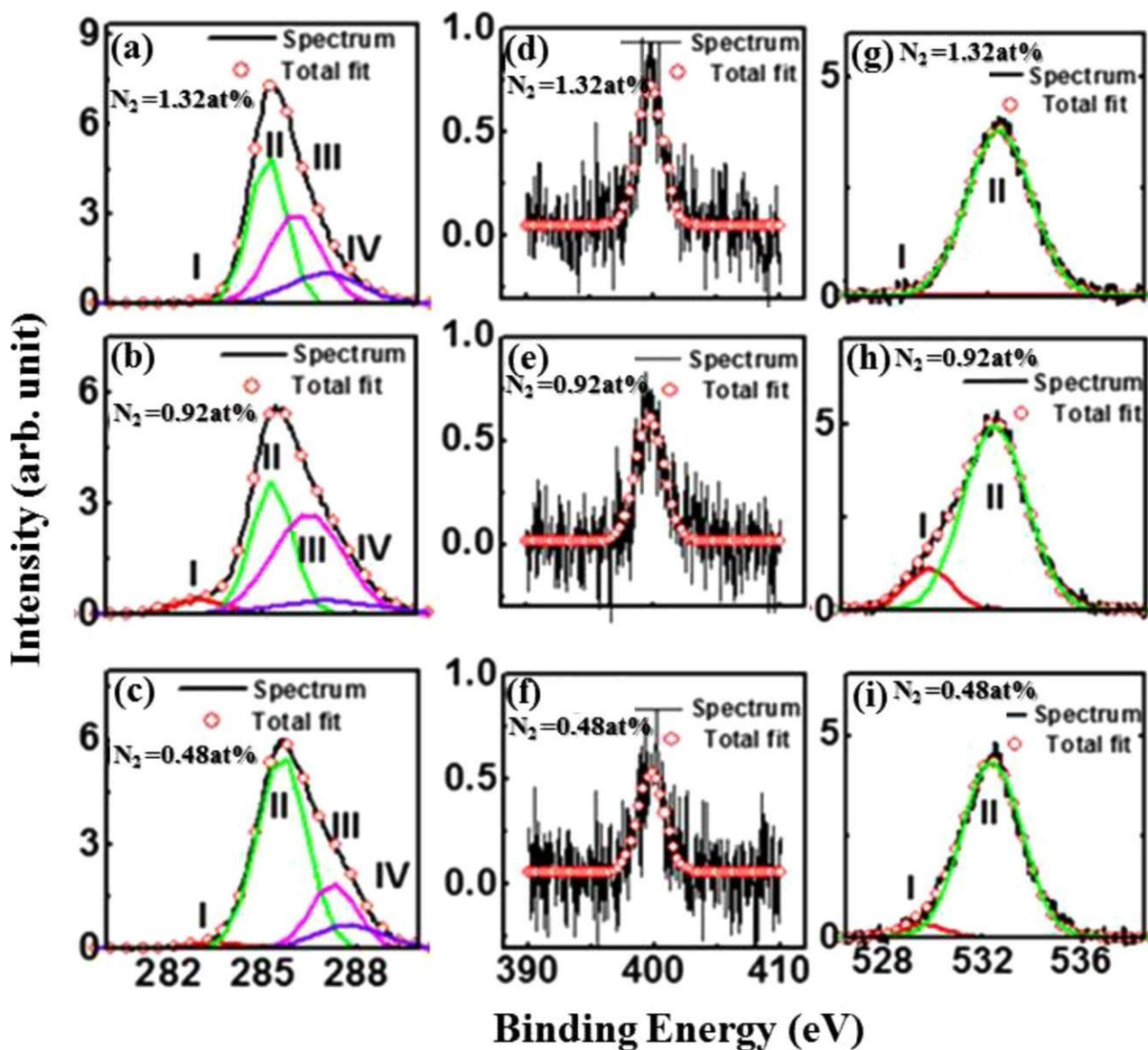
5

Fig. 4. -Figure 4. C 1s (a-c), N 1s(d-f) and O 1s (g-i) XPS spectra.

Table 2a

Different (a) C 1s, (b) O 1s, (c) N 1s XPS parameters obtained from convoluted C 1s XPS Spectra of UNCD synthesized at different hydrogen flow rate (sccm) with constant N2/Ar flow =5 sccm.

N₂ (at%)	C 1 s XPS → Peak I (sp²-C)				Peak II (sp³-C)				Peak III (sp³-C)				Peak IV (sp³-C)			
	Position x1 (eV)	Width Δw1	Intensity		Position x2 (eV)	Width Δw2	Intensity		Position x3 (eV)	Width Δw3	Intensity		Position x4 (eV)	Width Δw4	Intensity	
		(eV)	Area a1(a.u.)	Height h1(a.u.)		(eV)	Area a2(a.u.)	Height h2(a.u.)		(eV)	Area a3(a.u.)	Height h3(a.u.)		(eV)	Area a4(a.u.)	Height h4(a.u.)
1.32	283.4	1.25	2016	1281	285.1	1.19	74,053	49,737	286.1	1.69	63,470	30,041	286.9	2.41	31,419	10,414
0.92	283.1	1.93	9359	3868	285.3	1.33	59,812	35,952	286.5	2.31	79,270	27,403	287.0	3.53	16,947	3827
0.48	283.7	1.90	4554	1913	285.5	1.57	110,350	56,102	286.9	1.47	34,895	18,877	287.5	2.21	18,794	6795
	O 1s XPS →Peak I				Peak II				N 1s XPS →Peak I				Peak II			
1.32	528.6	1.08	53	39	532.4	2.48	11,869	3810	399.8	2.02	1696	669	–	–	–	–

| 0.92 | 529.8 | 1.74 | 2416 | 1108 | 532.3 | 2.39 | 14,926 | 4986 | 399.8 | 2.23 | 1653 | 590 | – | – | – | – |
| 0.48 | 529.7 | 1.59 | 635 | 319 | 532.4 | 2.40 | 12,997 | 4312 | 399.8 | 2.13 | 1268 | 474 | – | – | – | – |

of different atom (Carbon and oxygen) bonded nitrogen *viz.* (i) the peak below 400 eV to nitrogen bonded to sp^3 carbon (N–sp^3 C), and the peaks above 400 eV, to nitrogen linked to sp^2 carbon (N–sp^2 C), on the basis of the values of binding energy for urotropine (N–sp^3 C) at 399.4 eV and pyridine (N– sp2 C) at 399.8 eV, respectively [28,29]. The N-O

bonds also possibly formed within this UNCD matrix because N-O peak is generally observed at 402 eV in N 1s XPS spectra.

We have measured UPS using He-I (hv = 21.22 eV) and He−II (hv = 40.81 eV) excitation energy and the results are shown in Figs. 5(a) and (b) respectively. Fig. 5(a) shows the VB-edge (high K.E. slope ≈
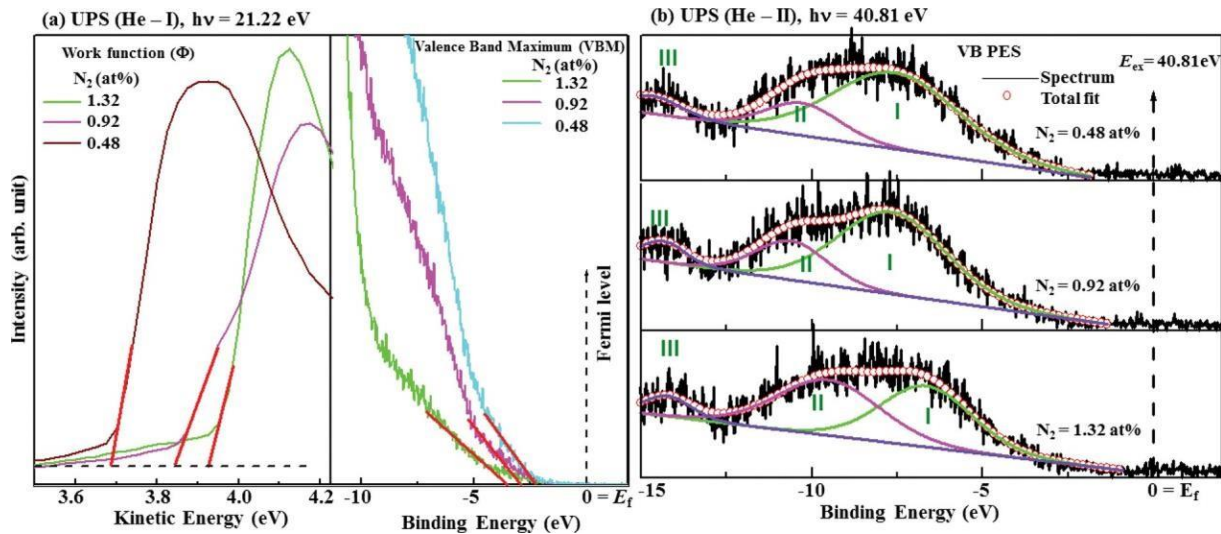
8

Fig. 5. -Figure 5. UPS spectra (a) He-I for evalute work function and VBM; (b) He-II for valence band states.

Table 2b
Different UPS parameters obtained from convoluted UPS (He-II) Spectra of UNCD synthesized at different hydrogen flow rate (sccm) with constant N2/Ar flow = 5 sccm.

N$_2$ (at%)	UPS (He-I), hν = 21.22 eV		UPS (He-II), hν = 40.81 eV								
			Peak I (p-σ)			Peak II (mixed of s- and p- state)			Peak III (s- state)		
	Work Function, Φ (eV)	Valence-Band Maximum, (VBM) (eV)	Position x1	Width	Intensity	Position x2	Width	Intensity	Position	Width	Intensity
	(eV)	(eV)	(eV)	Δw1 (eV)	a1(a.u.)	(eV)	Δw2(eV)	a2(a.u.)	x3(eV)	Δw3 (eV)	a3(a.u.)
1.32	3.93	3.60	6.6	3.15	45.56	9.5	3.55	46.67	14.2	1.60	7.77
0.92	3.84	2.97	7.6	3.73	70.36	10.6	2.49	22.29	14.3	1.52	7.35
0.48	3.68	2.26	7.5	4.38	73.38	10.3	2.62	18.70	14.3	2.01	7.92

converted into binding energy) and secondary electron cut-off (low K.E. slope) of the He-I (∼21.22 eV) spectra of UNCD films. These UPS valence band spectra are dominated by p-electron states due to the much higher excitation cross-section at these low photon energies [30]. The Surface work function of these UNCD films were derived from secondary electron cut-off low kinetic energy slope as shown in left panel of Fig. 5(a). A work function (Φ) of 4.37 eV is obtained for the reference Ag film. The Φ values of 1.32 at%, 0.92 at% and 0.48 at% N-doped UNCDs are 3.93 eV, 3.84 eV, and 3.68 eV respectively. The valence band maximum (VBM = E_f – E_{VB}) were estimated from the slope of each VB-edge spectra that are 3.60 eV, 2.97 eV, and 2.26 eV respectively, and shown in right panel of Fig. 5(a). From the obtained Φ and VBM values, we can roughly estimate the band gaps of these UNCD that are related with density of states (DOS) and/or work-functions in these UNCD films. It is found that the work-functions as well as VBM are decreases with decrease of N at%-content in these UNCD films. The work functions and VBM of N-doped UNCD are tabulated in Table 2b. The decrease of VBM also implies the increase of DOS that implies the decrease of band gaps. In order to understand the role of N$_2$/H$_2$/CH$_4$ gases in controlling the electronic structure, the valence-band spectra obtained by the excitation energy E_{ex} = 40.81 eV are decomposed into three Gaussian peaks after subtracting a Gaussian line, as shown in Fig. 5(b). These peaks are described as p-σ (6.6 eV – 7.6 eV: peak I), a mixture of s and p states (9.5–10.6 eV: peak II), and s (14.3 eV: peak III) bands of carbon, respectively [31]. A similar study were made by Francz et al. [32] for CVD-diamonds and they found a peak near ∼13 eV and assigned as "diamond" peak. Comparing our spectra, with this peak we may assigned the peak observed at ∼14 eV is "diamond peak".

4. Conclusion

UNCD thin films were prepared by MW-PECVD system in $CH_4/N_2/$ Ar/H_2 plasma atmosphere on silicon substrates. XRD and surface morphology study shows the formation of needle-like structure UNCD. The highest Hardness (Young's modulus) of these films 30 GPa (300 GPa) is correlated with their microstructure, electronic structure and bonding properties. We have shown that the change of small amount of N_2 content ($0.48 \rightarrow 0.98 \rightarrow 1.32$ at%), change their C-sp^3 hybridization and hence change their conductivity, work function as well as VBM results in change of hardness and Young's modulus of the UNCD films. These films are reproducible with the growth conditions and growth parameters in correlation with plasma features, and the feasibility of them to be used for the envisaged different electronic and coating technology applications has been established in this work.

References

[1] T.D. Corrigan, D.M. Gruen, A.R. Krauss, P. Zapol, R.P.H. Chang, The effect of ni- trogen additionto Ar/CH4 plasmas on thegrowth, morphology andfieldemission of ultrananocrystalline diamond, Diam. Relat. Mater. 11 (2002) 43.

[2] J. Birrell, J.A. Carlisle, O. Auciello, D.M. Gruen, J.M. Gibson, Morphology and electronic structure in nitrogen-doped ultrananocrystalline diamond, Appl. Phys. Lett. 81 (2002) 2235.

[3] V.N. Mochalin, O. Shenderova, D. Ho, Y. Gogotsi, The properties and applications of nanodiamonds, Nat. Nanotechnol. 7 (2012) 11.

[4] T. Tsubota, T. Fukui, T. Saito, K. Kusakabe, S. Morooka, H. Maeda, Surface morphology and electrical properties of boron-doped diamond films synthesized by microwave-assisted chemical vapor deposition using trimethylboron on diamond (100) substrate, Diam. Relat. Mater. 9 (2000) 1362.

[5] K.J. Sankaran, P.T. Joseph, H.C. Chen, N.H. Tai, I.N. Lin, Investigation in the role of hydrogen on the properties of diamond films grown using Ar/H_2/CH_4 microwave plasma, Diam. Relat. Mater. 20 (2011) 232.

[6] Y.S. Zou, Z.X. Li, Y.F. Wu, Deposition and characterization of smooth ultra-nanocrystalline diamond film in CH_4/H_2/Ar by microwave plasma chemical vapor deposition, Vacuum 84 (2010) 1347.

[7] V.P. Varnin, V.A. Laptev, V.G. Ralchenko, The state of the art in the growth of diamond crystals and films, Inorg. Mater. 42 (2006) S1–S18.

[8] M.Y. Liao, X.M. Meng, X.T. Zhou, J.Q. Hu, Z.G. Wang, Nanodiamond formation by hot-filament chemical vapor deposition on carbon ions bombarded Si, J. Cryst. Growth 236 (2002) 85.

[9] C. Zuiker, A.R. Krauss, D.M. Gruen, X. Pan, J.C. Li, R. Csencsits, A. Erdemir, C. Bindal, G. Fenske, Physical and tribological properties of diamond films grown in argon carbon plasmas, Thin Solid Films 270 (1995) 154.

[10] K. Chakrabarti, R. Chakrabarti, K.K. Chattopadhyay, S. Chaudhuri, A.K. Pal, Nanodiamond films produced from CVD of camphor, Diam. Relat. Mater. 7 (1998) 845.

[11] D. Zhou, A.R. Krauss, L.C. Qin, T.G. McCauley, D.M. Gruen, T.D. Corrigan, R.P. Chang, H. Gnaser, Synthesis and electron field emission of nanocrystalline diamond thin films grown from N_2/CH_4 microwave plasmas, J. Appl. Phys. 82 (1997) 4546.

[12] Y.F. Zhang, F. Zhang, Q.J. Qiao, X.F. Peng, Z.D. Lin, The roles of argon addition in the hot filament chemical vapor deposition system, Diam. Rela. Mater. 10 (2001) 1523.

[13] C.S. Wang, G.H. Tong, H.C. Chen, W.C. Shih, Effect of N_2 addition in Ar plasma on the development of microstructure of ultra-nanocrystalline diamond films, Diam. Relat. Mater. 19 (2010) 147.

[14] Sekhar C. Ray, Rudolph M. Erasmus, H.M. Tsai, C.W. Pao, I.-N. Lin, W.F. Pong, Hydrogenation effects of ultrananocrystalline diamond detected by X-ray absorption near edge structure and raman spectroscopy, J. Appl. Phys. 51 (2012) 095201.

[15] S. Yang, W. Man, J. Lyu, X. Xiao, Z. You, N. Jiang, Growth of mirror-like ultra-nanocrystalline diamond (UNCD) films by a facile hybrid CVD approach, Plasma Sci. Technol. 19 (2017) 055505.

[16] J. Liu, Li-Fu Hei, G.-C. Chen, C.-M. Li, W.-Z. Tang, F.-X. Lu, Growth of ultra-nanocrystalline diamond films in an Ar-rich CH_4/H_2/Ar atmosphere with varying H_2 concentrations, New Carbon Mater. 28 (2) (2013) 134.

[17] J. Shalini, K.J. Sankaran, C.-L. Dong, C.-Y. Lee, N.-H. Tai, I.-N. Lin, In situ detection of dopamine using nitrogen incorporated diamond nanowire electrode, Nanoscale 5 (2013) 1159.

[18] L.M. Apátiga, R. Velázquez, V.M. Castaño, Photochemical effect on diamond film surfaces induced by extended exposure to UV light, Surf. Sci. 529 (2003) 158.

[19] S.C. Ray, T.I.T. Okpalugo, C.W. Pao, H.M. Tsai, J.W. Chiou, J.C. Jan, W.F. Pong, P. Papakonstantinou, J.A. McLaughlin, W.J. Wang, Electronic structure and photoluminescence study of silicon doped diamond like carbon (Si:DLC) thin films, Mater. Res. Bull. 40 (2005) 1757.

[20] C.-C. Teng, S.-M. Song, C.-M. Sung, C.-T. Lin, Structural transformation upon nitrogen doping of ultrananocrystalline diamond films by microwave plasma CVD, J. Nanomater. 2009 (2009) 621208.

[21] R. Rani, K. Panda, N. Kumar, K.A. Titovich, K.V. Ivanovich, S.A. Vyacheslavovich, I-Nan Lin, Tribological properties of ultrananocrystalline diamond films: mechanochemical transformation of sliding interfaces, Sci. Rep. 8 (2018) 283.

[22] J. Feng, Y.-N. Xie, Z. Li, X.-Z. Wu, J.-G. Li, J. Me, Z.-M. Yu, Q.-P. We, Microscopic mechanical characteristics analysis of ultranano-crystalline diamond films, Trans. Nonferrous Met. Soc. China 25 (2015) 3291.

[23] M.A. Lodes, F.S. Kachold, S.M. Rosiwal, Mechanical properties of micro- and nanocrystalline diamond foils, Philos. Trans. A Math. Phys. Eng. Sci. 373/2038 (2015) 20140136.

[24] J.C. Madaleno, M.K. Singh, E. Titus, G. Cabral, J. Gra´cio, L. Pereira, Electron field emission from patterned nanocrystalline diamond coated α-SiO_2 micrometer-tip arrays, Appl. Phys. Lett. 92 (2008) 023113.

[25] S. Ohmagari, T. Yoshitake, A. Nagano, R. Ohtani, H. Setoyama, E. Kobayashi, T. Hara, K. Nagayama, Formation of p-Type semiconducting ultrananocrystalline diamond/hydrogenated amorphous carbon composite films by boron doping, J. Appl. Phys. 49 (2010) 031302.

[26] T. Yoshitake, A. Nagano, S. Ohmagari, M. Itakura, N. Kuwano, R. Ohtani, H. Setoyama, E. Kobayashi, K. Nagayama, Near-edge X-ray absorption fine-structure, X-ray photoemission, and fourier transform infrared spectroscopies of ultrananocrystalline diamond/hydrogenated amorphous carbon composite films, J. Appl. Phys. 48 (2009) 020222.

[27] A. Laikhtman, I. Gouzman, A. Hoffman, G. Comtet, L. Hellner, G. Dujardin, Sensitivity of near-edge x-ray absorption fine structure spectroscopy to ion beam damage in diamond films, J. Appl. Phys. 86 (1999) 4192.

[28] W.T. Zheng, H. Sjöström, I. Ivanov, K.Z. Xing, E. Broitman, W.R. Salaneck, J.E. Greene, J.-E. Sundgren, Reactive magnetron sputter deposited CNx : effects of N_2 pressure and growth temperature on film composition, bonding, and microstructure, J. Vac. Sci. Technol. A 14 (1996) 2696.

[29] W.T. Zheng, K.Z. Xing, N. Hellgren, M. Lögdlund, A. Johansson, U. Gelivs, W.R. Salaneck, J.-E. Sundgren, Nitrogen 1s electron binding energy assignment in carbon nitride thin films with different structures, J. Electron. Spectrosc. Relat. Phenom 87 (1997) 45.

[30] F.R. McFeely, S.P. Kowalczyk, L. Ley, R.G. Cavell, R.A. Pollak, D.A. Shirley, X-ray photoemission studies of diamond, graphite, and glassy carbon valence bands, Phys. Rev. B 9 (1974) 5268.

[31] A. Mansour, D. Ugolini, Photoelectron-spectroscopy study of amorphous *a*-CNx:H, Phys. Rev. B 47 (1993) 10201.

[32] G. Francz, P. Kania, P. Oelhafen, Photoelectron spectroscopy of CVD diamond, Diam. Relat. Mater 3 (11–12) (1994) 1289–1292.